Laser-beam welding as a method to characterise in-situ local thermo-mechanical conditions leading to liquid zinc embrittlement of Dual-Phase steel

Thesis report for Materials Science & Engineering, Metals Science & Technology Master Programme

by
Huub Rombouts
4301234

Thesis performed at:
Joining and Additive Manufacturing research group
at faculty 3me TUDelft

Supervisors:
Dr.Ir. M.J.M. Hermans
G. Agarwal PhD.

Thesis Committee:
Dr.Ir. M.J.M. Hermans
Dr. V. Popovich
G. Agarwal PhD.
Dr. H. Gao
Arjun Sood MSc.

Materials Science and Engineering

TUDelft Delft University of Technology

Abstract

Liquid metal embrittlement (LME) is a problem encountered in the resistance spot welding joining process of advanced high-strength steels in the automotive industry. Its occurrence reduces the mechanical performance of welds. The nature of resistance spot welding prevents in-situ characterisation of thermo-mechanical conditions causing LME. Laser-beam welding (LBW) under tension is proposed as an alternative method to analyse LME cracks growing during the welding process of a DP1000 dual-phase steel grade. The influence of global thermo-mechanical parameters on the degree of embrittlement is investigated through Gleeble hot tensile tests. LBW schedules are explored, and material characterisation used to find and prove LME crack occurrence. Finite element analysis with COMSOL is used to connect results from Gleeble hot tensile tests with results from LBW and relevance to RSW is outlined. Results show that a temperature dependent ductility trough is present between 750 and 900°C. The Fe-Zn system is further found to require specific mechanical conditions (stress and strain rate) to become susceptible to LME. The proposed LBW setup is found to be susceptible to LME, but not in a high enough severity to be detectable through SEM and EDS. Changes should be made to the loading setup of the LBW setup to induce LME crack growth to a sufficient degree to allow for in-situ monitoring of local thermo-mechanical conditions surrounding the crack.

Contents

1. Introduction

Advanced High-Strength Steels (AHSS) are carefully manufactured steels through precise chemical compositions and specific heat treatments leading to steels with microstructures using different strengthening mechanisms to improve their mechanical properties over conventional steels. Superior strengths, maximum elongations, fracture toughness etc. can be achieved, uniquely combining high ranges of these properties [1]. As shown in figure 1.1, AHSS grade steels surpass the conventional steels in many aspects.
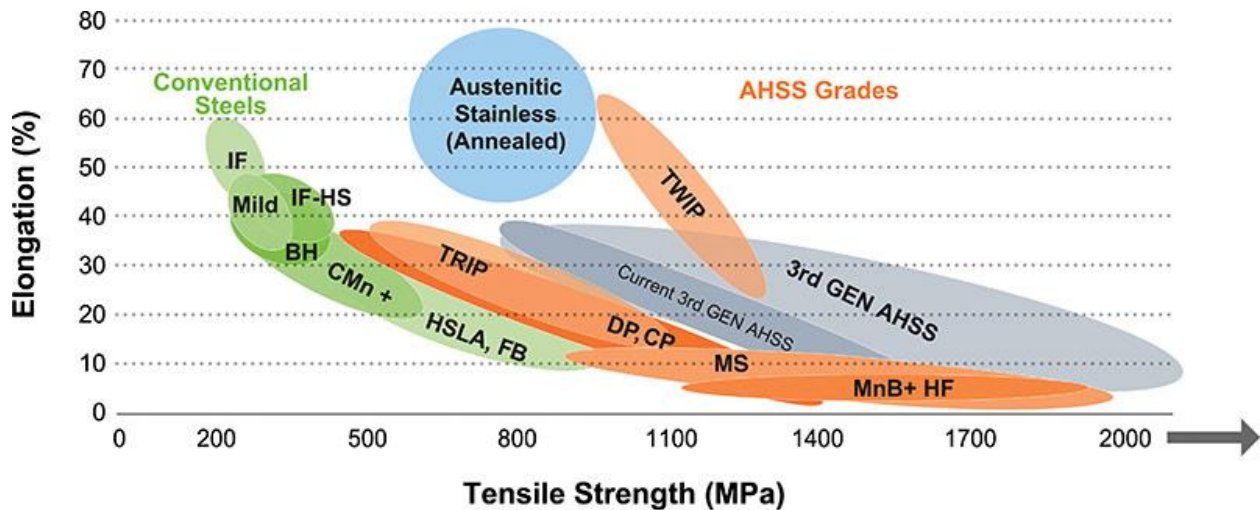
Figure 1.1: Strength-ductility diagrams showing different grades of conventional steels and AHSS [1]

In addition to the exceptional mechanical properties achievable in AHSS, they are tailored to be lightweight. Because of the combination of the mechanical and lightweight properties AHSS are widely utilised in the automotive industry. For example, the high energy absorption of Dual-Phase (DP) and Transformation-Induced Plasticity (TRIP) steels make them useful for crash absorbing structural elements, while the extreme strengths of Martensitic and boron-based Press Hardened steels make them ideal for impact absorbing structures such as the passenger cage [2].

However, the unique microstructures of AHSS often come paired with unique challenges. DP steel is a steel recently discovered to encounter such an issue. Liquid-metal-embrittlement (LME) is a phenomenon that can occur in a solid metal when it is brought into contact with a specific liquid metal. Several such pairs have already been known for a longer time, such as solid aluminium and liquid gallium [3] and solid lead and liquid bismuth [4] [5] [6]. More recently, another discovered pair is solid iron and liquid zinc [7]. In conventional steels, the issue was not present, but the specific microstructures of AHSS make them more susceptible to grain boundary related weakening mechanisms, such as solidification cracking [8] and LME [9]. Nevertheless, specific conditions are needed for the metal becoming susceptible to LME, including a combination of high temperature and an externally applied stress. The application of DP steels in the automotive industry, body panels [2], have been found to encounter such conditions. Resistance Spot Welding (RSW) is a joining technique employed in joining car body panels using Joule heating to melt the material. To achieve the weld, high compressive and shear stresses are introduced to the weld area,

along with high temperatures in the weld and surrounding the weld. LME cracks have been observed to occasionally occur during the welding process for several AHSS including DP steel [10] [11] [12]. The nature of a RSW (electrodes covering the weld and a small area) creates difficulty in characterizing the specific thermo-mechanical conditions during joining that lead to LME. Without knowing the specific thermo-mechanical conditions, no measures can be taken to prevent them. Therefore, an alternative method for analysing LME in AHSS, specifically DP steel is proposed to analyse thermo-mechanical conditions. Through laser-beam welding (LBW), the welded area can remain visible. By using LBW together with an externally applied load, local conditions leading to LME can be extracted during welding and translated back to RSW. This thesis explores the potential of LBW under tension as a method to characterise LME during joining. To this end, the global thermo-mechanical conditions are investigated through Gleeble hot-tensile testing and translated to LBW to find welding schedules causing LME. Both quantitative embrittlement and microstructural signs of embrittlement are explored. The different setups (Gleeble, LBW) are compared with the aid of Finite Element Analysis (FEA) software using COMSOL.

The following research questions connected to LME will be explored:

1. Is LBW under tension a viable alternative to RSW to investigate the microscopic thermo-mechanical conditions leading to LME during the welding process, including a high detectability and reproducibility of LME cracks?
2. What are the macroscopical thermo-mechanical conditions and mechanism leading to LME in Gleeble hot tensile testing?
3. To what extent are Gleeble testing results applicable to LME occurrence in LBW and to what extent are Gleeble and LBW LME results applicable to RSW.

2. Theory

In this chapter, the background theory of the different aspects of this study will be explained. The current knowledge on the phenomenon of Liquid Metal Embrittlement (LME) and its atomic-scale mechanism will be explained. The material investigated for the study will be introduced in chapter 2.2, followed by characteristics of the processing techniques, resistance spot welding (RSW) and laser beam welding (LBW), employed.

2.1 Liquid Metal Embrittlement

LME is a phenomenon occurring in specific solid-liquid metal pairs, that leads to weakening of the solid metal upon exposure to the liquid metal. The LME phenomenon poses a serious problem in several applications, including in welding and in liquid metal nuclear reactor materials. This section will describe the effects of LME on the macro- and microscale, will give an insight in the current knowledge on the atomistic mechanism involved in LME and will show its effects on the most investigated metal pair: aluminium and liquid gallium. Finally, this chapter provides a description of the theoretical aspects concerning the metal pair considered in this investigation: iron and liquid zinc.

2.1.1 Atomistic Mechanism

The atomic scale mechanisms governing LME have been studied on a well-known LME pair: Al-Ga. Because of the low temperature needed for the embrittling of this system, being around 30 °C, since Gallium has a melting point of 29.76 °C [13], in-situ observations are more readily available. Although the system will be slightly different from the iron-zinc system of interest to this study, it will provide an insight into the mechanisms that leads to LME.

The foundation of the LME phenomenon is defined by interfacial energies. As will be explained in more detail in this chapter, LME leads to brittle crack propagation by penetration by the liquid metal into grain boundaries. This step is fundamental for LME to occur. The most important requirement a system must fulfil to be susceptible to LME is equation 2.1. The two interfaces created by wetting of the grain boundary with the liquid metal must have a lower interfacial energy than the grain boundary interface.

$$\gamma_{GB} - 2\gamma_{SL} \geq 0 \qquad\qquad \text{(eq 2.1)}$$

The factors influencing susceptibility and severity of a material to LME are therefore all related to these energies. Some of the most important factors [4] [14] are listed below and will be discussed further throughout chapter 2.

1. The solid-liquid metal combination: Not all combinations of solid and liquid metals are susceptible to LME. If the interfacial energy of two solid metal-liquid metal interfaces is significantly higher than the average grain boundary energy of the solid metal, no other factors can change these energies enough to make grain boundary wetting thermodynamically favourable. Therefore, LME will never occur in such systems.

2. Solid metal microstructure: This factor is related to the solid-liquid metal combination. The same metal could have different microstructures, leading to different properties, including a higher or lower grain boundary energy. Additionally, alloying elements in a metal can drastically alter the energetic properties of the material.
3. Temperature: Temperature will affect both the liquid-solid interfacial energy, as well as the grain boundary energy. For each energy, the dependence on temperature is different, leading to temperature ranges where LME is possible.
4. Stress: Applying a stress to the solid metal will introduce more energy into the system. Part of the introduced energy will increase the grain boundary energies of the system, especially if the grain boundary is perpendicular to the loading direction. Therefore, higher stresses could make a normally non-susceptible system susceptible to LME.
5. Strain rate: Like stress, the strain rate will increase the grain boundary energy of the solid metal. However, when only applying a constant stress, the metal, especially at higher temperatures, will equilibrate with the applied stress, lowering the increased grain boundary energy caused by the stress over time. When applying a strain rate, the system will become more dynamic, maintaining the increased grain boundary energy.

Figure 2.1 provides a schematic overview of three atomistic steps that can be distinguished in LME, which will be discussed sequentially.
The first step (figure 2.1a) of LME is wetting of solid metal surface or a crack tip. Because the system is not in an equilibrium state when loaded, perfect wetting of the liquid metal near the crack tip does not occur. The wetting angle is therefore not 0, leading to a capillary force on the liquid metal that pulls the liquid metal in the direction of the crack tip [15], causing penetration of the liquid metal into the crack.
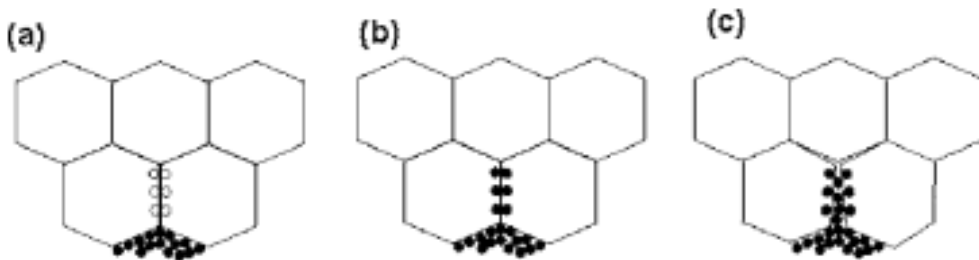
Figure 2.1: schematic representation of the three steps leading to LME. The liquid metal penetrates the crack until it wets the surface in front of the grain boundary (a), the liquid metal penetrates the grain boundary and forms a solid interface with the adjacent grains (b), more metal penetrates the interface, leading to loss of cohesion of the grains (c).

The second step is penetration of liquid metal from the material surface into the grain boundary and consequential grain boundary wetting (figure 2.1b). The capillary force leading to penetration of liquid metal into a crack as mentioned before assists in pulling the liquid metal into the grain boundary. [15] [3]. Thermodynamically, penetration into the GB is only possible when the system fulfils the fundamental Equation 2.1.

So, the interface energies of the two new solid-liquid interfaces should be smaller than the interface tension of the grain boundary. If the condition is fulfilled, it would be energetically favourable for the liquid metal to penetrate the grain boundary. This condition explains why LME is encountered only in specific solid-liquid pairs or in specific solid metal microstructures, as the energies of the original grain boundary energy and the liquid-solid interfacial energies should be close enough together for changes in macroscopic conditions causing the system to fulfil Equation 2.1.

In a study by Sigle [16] it was found that the actual system involved in the GB penetration step is slightly different. By letting liquid gallium penetrate the solid system and taking HRTEM images of the GB at the liquid metal penetration front, figure 2.2 was obtained.
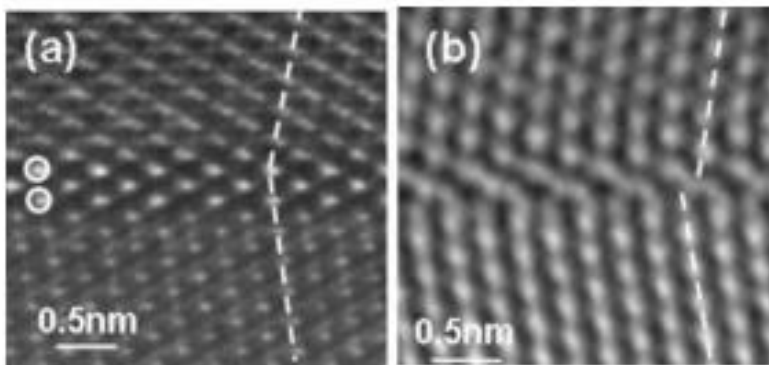
Figure 2.2: HRTEM images of liquid gallium penetration into aluminium grain boundaries, showing the liquid penetration front indicated by the circles (a) and showing progressed penetration of liquid Gallium separating the inclined aluminium crystal planes (b) [16]

Their results showed that the liquid metal penetrating the grain boundary was forced into a solid state despite the temperature still being above the melting point of gallium. Additionally, the HRTEM images showed that the gallium in the GB was the same solid f.c.c. crystal structure as the aluminium lattice but the lattice planes are inclined to match both adjacent grains as closely as possible. However, solid gallium normally crystallizes into an orthorhombic structure, deviating strongly from the f.c.c. structure found here. This indicates that the interfacial energy of the aluminium and f.c.c. gallium interface is low enough that the aluminium forces the liquid gallium into a solid state fitting the aluminium crystal structure.

The final step leading to LME is the loss of grain boundary cohesion following grain boundary penetration (figure 2.1c). Ab initio calculations determined that the metal penetrating the GB, in this case gallium, has a strong bonding to the solid metal, leading to a strong interface between a grain and the first layer of the penetrating metal. However, the atomic bond strength of the penetrating metal is relatively weak. This means that the two adjacent grains are strongly bound to the penetrating metal, but as enough metal penetrates into the grain boundary to form atomic layers between the interfaces, the grains will easily lose cohesion when a stress is introduced, due to the gallium layers between the interface layers causing separation of the grains [17] [18].

2.1.2 LME induced crack propagation

LME weakens the solid metals in wetting contact with a liquid metal, leading to sudden brittle crack propagation and eventual brittle failure of a normally highly ductile metal. It results in crack formation and failure at significantly shorter elongations and reduced fracture energy [4] [19] [14] when the material is exposed to an embrittling liquid metal. The phenomenon has been known for over a century and was characterized as LME after the first study on liquid mercury embrittling β-brass [20].

On the crack size scale, as mentioned in section 2.1.1. the liquid metal enters the crack and travels to the crack tip, where the liquid metal penetrates the grain boundary and forms a strong interface with the solid metal. In the grain boundary, the liquid metal is then forced into a solid state. Because the strength of the embrittling metal is often significantly lower than the solid metal, the stress that does not lead to crack growth in the solid metal, instead causes the crack to propagate through the weaker metal now present in the grain boundaries. No significant amount of time is necessary for the liquid metal to weaken the crack tip, so crack propagation velocity is limited by the penetration speed of the liquid metal towards the crack tip. Since the penetration of the liquid metal is often fast, crack propagation velocities during LME are reported to be around 100 mm/s [21]. These crack propagation velocities are found in cases where the metal is normally not prone to brittle cracking, such as f.c.c. metals. In the case of metals being sensitive to cracking, the weakening of the crack tip by a liquid metal may lead to a longer crack length at speeds in the m/s range [22].

In most cases, LME can only occur while the solid metal is in contact with the embrittling liquid metal. If the solid metal is exposed to the liquid metal while not stressed and only stressed after removing the liquid metal, no embrittling is found. The reason for this is that often, the temperature where the couple leads to embrittlement is at a low enough temperature that penetration of the liquid metal into the solid metal is not fast enough to leave enough embrittling metal to cause LME [21]. So, if a crack nucleates at a later point, chances are low that liquid metal is present near the crack tip which would lead to weakening. However, since there could be cases where penetration of the liquid metal is fast enough or exposure times are long enough, embrittlement caused by the embrittling metal in solid solution, after removal of the liquid metal has still been found [23]. Figure 2.3 shows the ratio of the maximum load after exposure to the maximum load before exposure to liquid metal (F_m/F_{m0}) and the ratio of fracture surface cross section after exposure and before exposure ($S_{brittle}/S_0$) for different solid-liquid pairs after removal of the liquid metal from the surface. This figure shows that for short term exposure to liquid metals, which may also occur during welding, the embrittlement effects will only be present while the solid is in contact with the liquid metal. However, longer exposure times, as would be present in liquid metal nuclear reactors would pose a risk of embrittlement after the liquid metal has been removed from the surface [24].
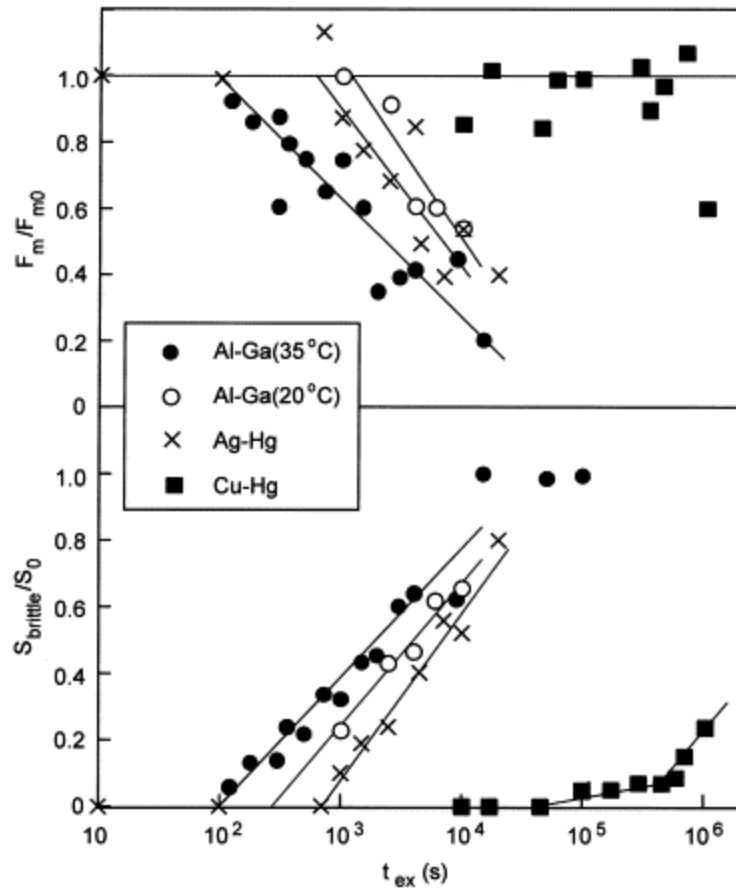
Figure 2.3: Normalized maximum load reduction and fracture surface cross section reduction as a function of exposure time to liquid metal followed by removal of liquid metal from the surface for different solid-liquid pairs [24].

2.2 Galvanized DP steels

The steel investigated in this thesis is a galvanized DP1000 steel. This section will outline properties of dual-phase (DP) steels, their production routes, and microstructural characteristics before explaining the process of hot-dip galvanization coating the final product with a zinc layer.

2.2.1   DP steel [25]

Dual Phase (DP) steels are a family of advanced high-strength steels (AHSS) having a high combination of strength and ductility. Presently, ultimate tensile strengths of DP steels can be achieved in the range of 400 to 1200 MPa, with most grades having strengths between 600 and 800 MPa. Maximum elongations of around 8% are easily achievable. These excellent properties of DP steels are obtained by the combination a ferritic steel matrix and martensitic zones, often in the form of so-called martensite 'islands'. The final steel structure partitions the applied stresses and strains between the two different steel phases and can achieve a combination of high ductility by the ferritic phase with the high strength and hardness of the martensite. The martensite, with its exceptional strength and hardness, bears the largest amount of the load, whereas the ferrite will deform plastically sooner, leading to a high strain-hardening rate. By carefully tailoring the martensitic volume fraction and morphology, the optimal combination of strength and ductility can be obtained for a specific application. Figures 2.4 and 2.5 show the effect of the martensite volume fraction of a DP steel with the same chemical composition on the tensile strength and ductility, respectively. These graphs clearly show the range of combinations of tensile strengths and ductility achievable with DP steels.
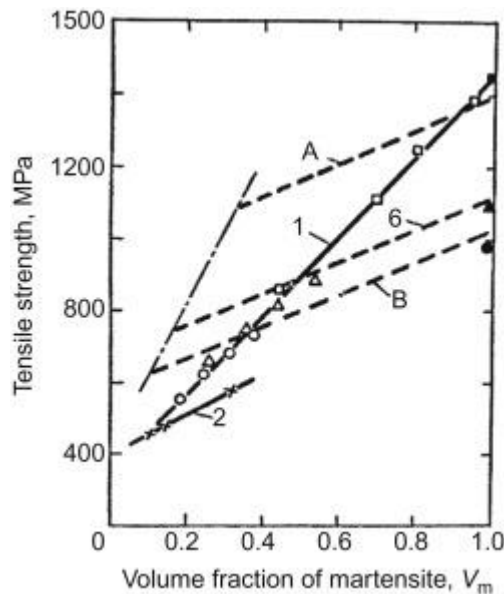
Figure 2.4: Tensile strength as a function of martensite volume fraction of a CR-Mn-Si-B DP steel with various content of carbon: ○- steel with 0.07% C; Δ-0.10% C; □—0.18% C. The solid symbols indicate fully martensitic microstructure. Dashed lines show calculated tensile strength using the rule of mixtures when mixing the three different carbon content steels [25]
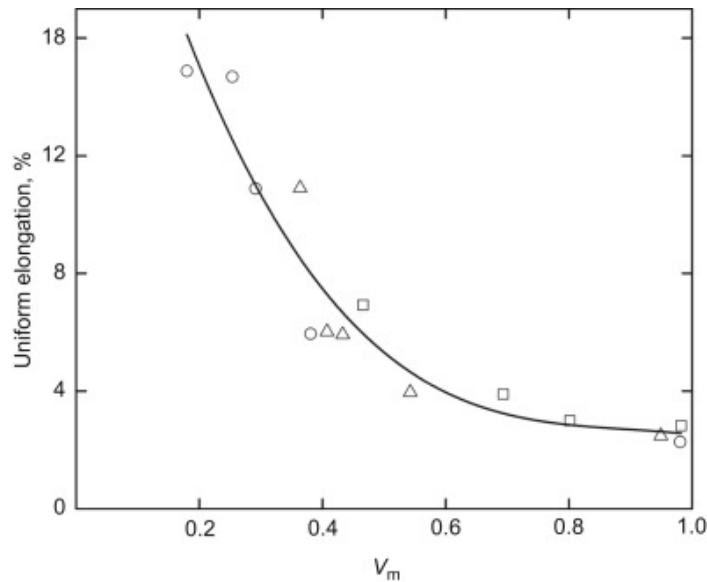
Figure 2.5: Maximum uniform elongation as a function of martensite volume fraction (V_m) of a Cr-Mn-Si-B DP steel [25]

Production of the unique combination of ferrite and martensite is mostly controlled by applying a specific heat treatment cycle to a steel. First the steel is heated above the A_E temperature, forming a fully austenitic microstructure. Starting from the austenitic microstructure, slow cooling first leads to the formation of ferrite. Holding the steel at a constant temperature, in the case of the steel composition discussed here at 920°C, while ferrite is growing controls the amount of ferrite present in the final microstructure limited by the equilibrium austenite/ferrite composition at the chosen temperature. By quenching with a high cooling rate, the remaining austenite is then transformed to martensite, thereby avoiding the formation of cementite and pearlite. By choosing different holding times for the isothermal period, the final martensite volume fraction can be controlled. This production route, called step quenched (SQ) is shown schematically in a continuous cooling transformation (CCT) diagram in figure 2.6.
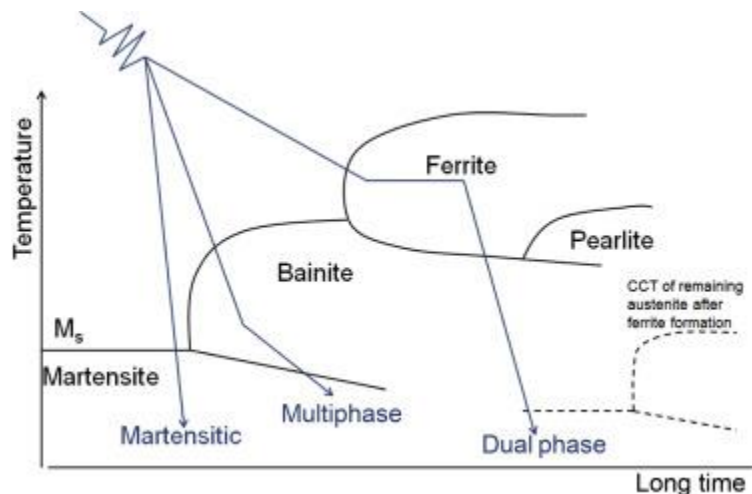
Figure 2.6: Schematic CCT diagram of a steel composition with a processing route leading to the formation of DP steel. [25]

Another approach to create DP steels is to immediately quench the fully austenitic microstructure to a fully martensitic microstructure, called intermediate quench (IQ). The second step in this treatment involves annealing at an intercritical temperature, in this case at 850°C to form ferrite and austenite, growing from the martensite microstructure [7] until the desired ferrite content is achieved, then quenching again to transform the formed austenite back to martensite.

Microstructural results of the two different processing routes are shown in figure 2.7 and 2.8. and properties in figure 2.9 A finer martensitic microstructure leads to superior combinations of strength and ductility. So, choosing a more complex production route can lead to superior final materials.
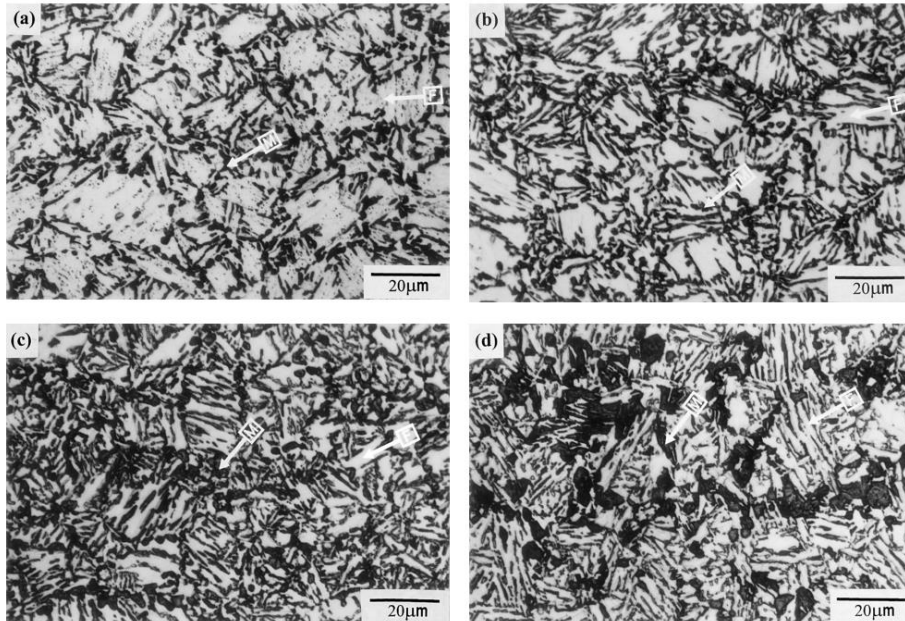
Figure 2.7: Fine martensite microstructure obtained by annealing a martensitic steel at increasing temperatures using an IQ treatment from (a) to (d) [7]
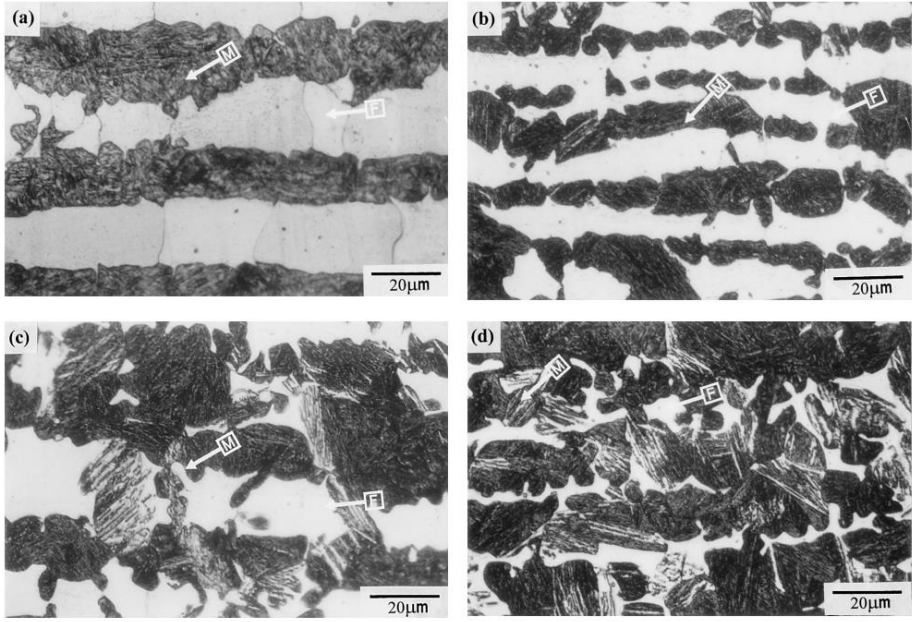
Figure 2.8: Coarse martensite microstructure obtained by cooling to an intercritical temperature increasing from (a) to (d) through a SQ treatment [7]
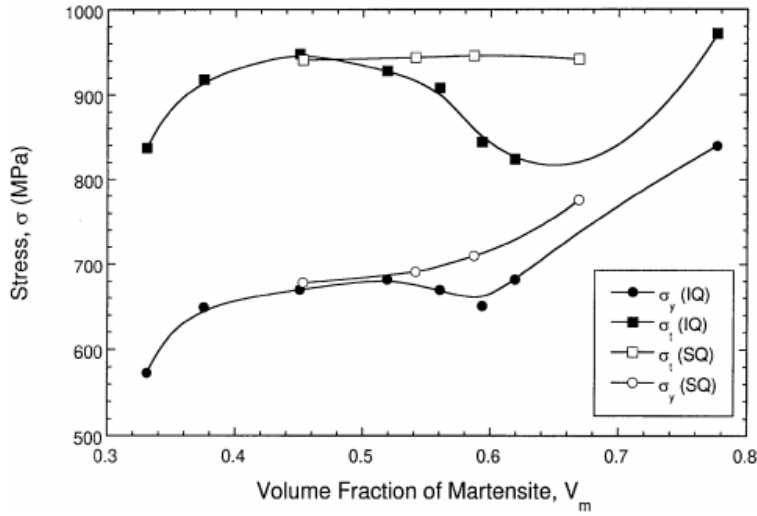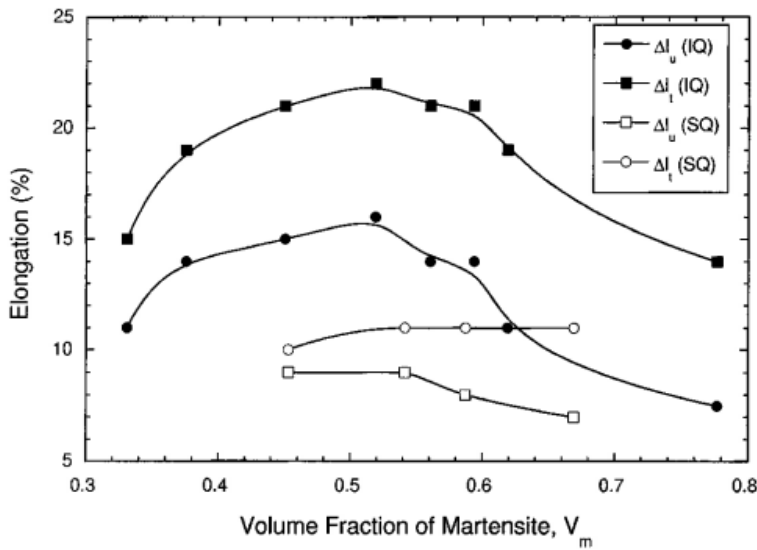
Figure 2.9: Tensile strength (a) and maximum elongation (b) for the two different production routes at increasing martensite volume fraction

2.2.2 Hot-dip galvanization

Galvanization is the process of applying a zinc-coating to an iron or steel with the purpose of protecting the underlying material against corrosion [26]. The corrosion protection is two-fold. Firstly, the zinc layer is the only material exposed to a corrosive medium, be it air or an aqueous environment. A typical galvanized coating is shown in figure 2.10.
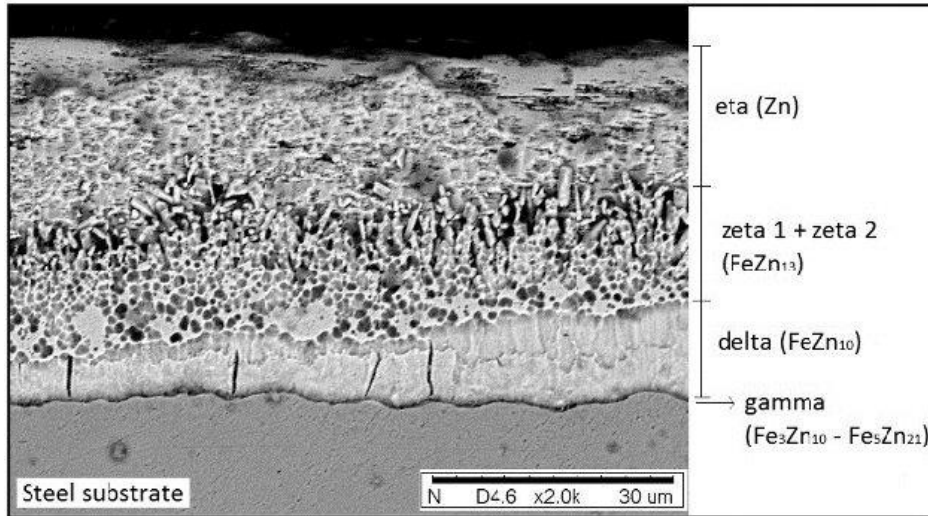
Figure 2.10: Typical microstructure of the zinc coating of a galvanized steel substrate [27]

The zinc coating blocks contact between the steel and the atmosphere. Because zinc oxidizes very slowly it takes a long time before the atmosphere can interact with the iron substrate, thereby retarding the corrosion of the steel part. Secondly, zinc provides a galvanic protection to the iron in the case that the coating is locally damaged. Zinc is less noble than steel or iron as shown in figure 2.11. The galvanic protection means that if two different metals, in this case steel and zinc, are in contact, the less noble metal will be preferentially corroded. So, even when the coating is damaged, the underlying steel substrate will not corrode.

The most common way of applying the zinc-coating is by hot-dip galvanizing. In hot-dip galvanizing, the steel part to be coated is submerged in a bath of liquid zinc, which coats the steel in a thin layer of liquid zinc. Upon cooling, either by air or a cooling liquid, the zinc layer solidifies, resulting in a uniform zinc coating with a thickness of 10-100 micron [28].

Although the zinc coating is highly beneficial for corrosion protection, it can pose problems during welding of galvanized parts. The welding process locally achieves high temperatures and stresses, resulting in areas where Zn will evaporate, whereas in some regions of the heat affected zone the zinc will be present as a liquid phase. Due to a nonhomogeneous temperature in the welded part stresses will be introduced. As mentioned in section 2.1, both are important factors leading to LME.
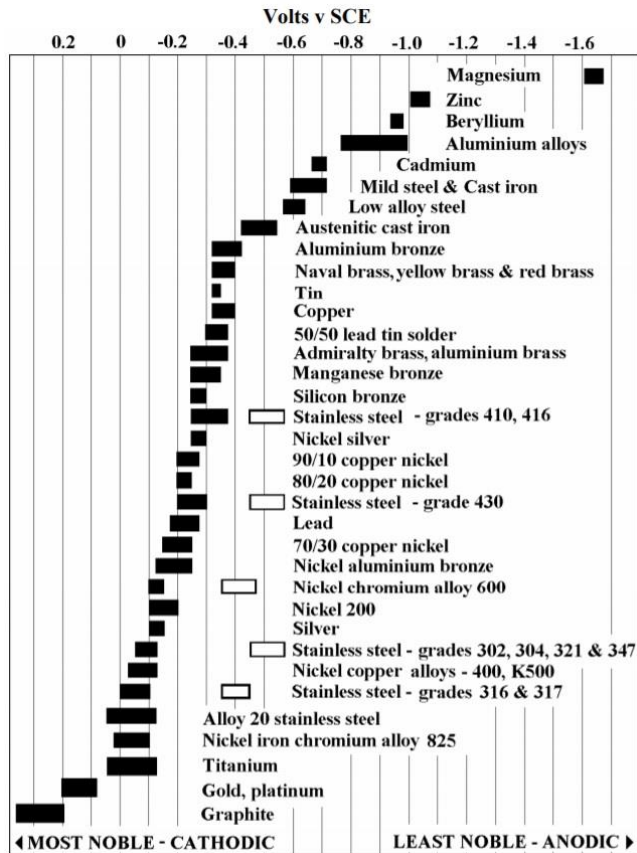
Figure 2.11: Galvanic series of commonly used metals showing the highly anodic nature of zinc [29]

2.3 Resistance spot welding

Resistance Spot Welding (RSW) is a welding method most used for the joining of sheet metals. In the automotive industry it is utilised to join the body panels. A typical automotive construction contains several thousand resistance spot welds [30]. This section will outline the general process characteristics used to achieve RSW and some underlying mechanisms. Afterwards, the occurrence of LME in RSW will be addressed and current research on the topic will be outlined.

2.3.1 The process

In RSW two electrodes are used that clamp the sheets to be welded together using compressive forces in the kN ranges. An electrical pulse is then applied through the electrodes that melts the material in the interface of the two metal sheets through a Joule heating process, leading to a welding nugget. Because of the high temperatures that are achieved during the welding process, the electrodes need to be cooled using water flowing through the inside of the electrode. Figure 2.12 shows a schematic view of a typical RSW setup.
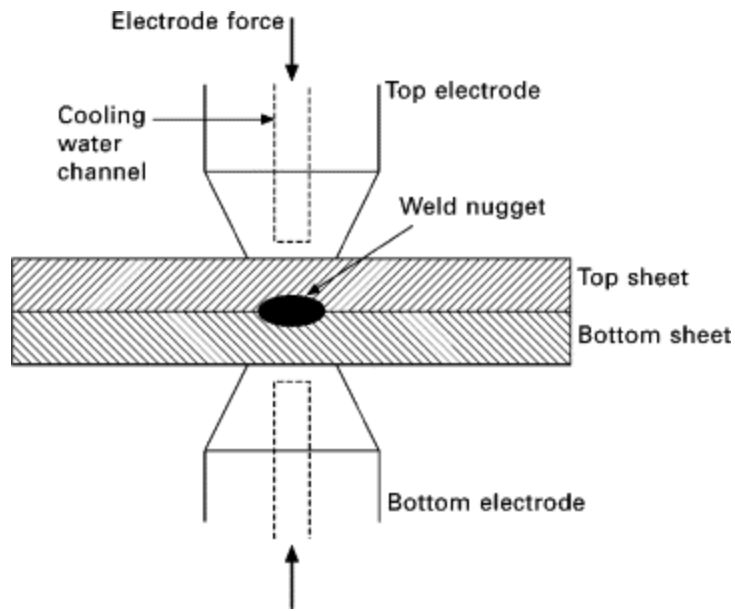
Figure 2.12: Schematic representation of a RSW setup [31]

The processing parameters for a RSW depend highly on the materials to be joined. The electrode forces must be tailored to ensure proper contact in the interface between the two sheets and between the sheet surface and the electrode, while avoiding significant deformation of the material. More important however, are the welding current and the welding time. Both parameters are linked to the final weld nugget diameter. A too low current or too short welding time can lead to small nuggets that easily fail. Using too high a current or time can lead to the welding nugget growing beyond the diameter of the electrode. At this point, cooling from the cooling water in the electrode becomes significantly less efficient in the areas beyond the electrode tip. High temperatures can then cause expulsion of the liquid metal from the weld interface. Combinations of welding current and welding times form an envelope or weldability lobe with desirable welds [31]. A schematic weldability lobe is shown in figure 2.13.
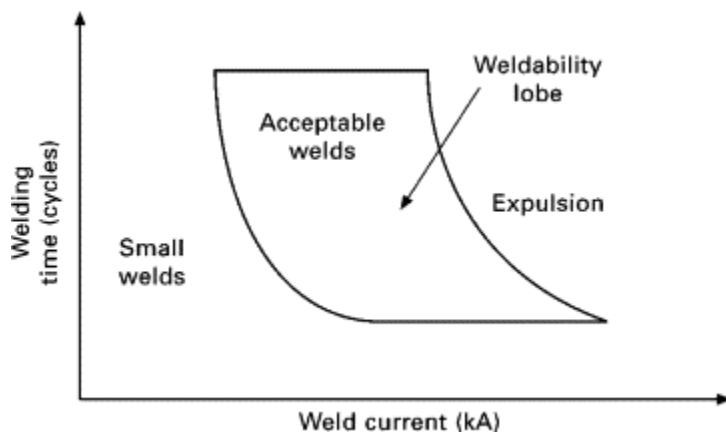
Figure 2.13: schematic weldability lobe for a RSW process [31]

The specific material to be joined determines the location of the weldability lobe on the graph. When comparing an uncoated steel with a hot-dip galvanized steel, the Zn-coated sheets require more electrode

force, higher welding currents and longer welding times as shown in table 2.1. The more extreme conditions are required for Zn-coated steels for two reasons: the additional Zn-layer increases the total amount of material heating up, so more energy is needed. Additionally, both the melting and boiling point of zinc are lower than the melting point of steel. To weld the steel sheets, therefore requires the zinc to melt and boil, requiring both more energy input, as well as changes in the contact surface between the electrodes and the sample surface [32].

Table 2.1: Comparison of RSW processing parameters necessary for the joining of two sheets of 0.9 mm thickness [33]

Parameter	Steel (uncoated)	Zn-coated steel (hot-dipped)
Welding time (cycles) at 50 Hz cycles	7-10	9-12
Current (kA)	7-10	9-11
Force (kN)	1.9-2.6	2.2-2.9

The Zn-coated steel is therefore exposed to more extreme conditions for longer times than the uncoated steel. The Zn-coating will therefore locally melt and be in contact with the high temperature substrate that is under significant external stresses due to the applied electrode force, as will be shown in the next section. All conditions prevailing during welding fulfil the LME requirements detailed in section 2.1.1, thus making the system susceptible to LME in certain areas around the spot weld.

2.3.2   LME in RSW

The extreme local temperatures and stress states that arise during spot welding of galvanised steels create zones in or around the weld that can be highly susceptible to LME. Cracks could form during welding, reducing the performance of the weld. Additionally, predicting the exact location, nature and extent of cracking caused by liquid zinc is, currently, not accurately possible. Therefore, the mechanical behaviour of the steel surrounding the weld is unpredictable and can lead to issues.

Multiple studies have been carried out on LME in RSW of galvanised steels [9] [10] [11] [12] [30]. The steels that are susceptible to LME are, in most cases, the same steels that are susceptible to hydrogen embrittlement, due to both mechanisms acting on decohesion characteristics [34]. Therefore, the steels studied regarding LME are exclusively in the AHSS family, specifically TWIP and TRIP steels. The LME cracks that are formed during RSW are typically found at two locations: The first, predominantly occurring crack, forms at the surface in contact with the electrode. The second, less likely crack, occurs in the interface between the two welded sheets. In both cases, the cracks are so-called circumferential cracks. The cracks nucleate at one point and then grow circumferentially around the electrode [9]. Depending on the specific conditions, cracks can be large and easily visible, in which case there are often few cracks, as shown in figure 2.14 [9] or the cracks are smaller and only revealed upon high magnifications, in which case there are more cracks as shown in figure 2.15 [11].
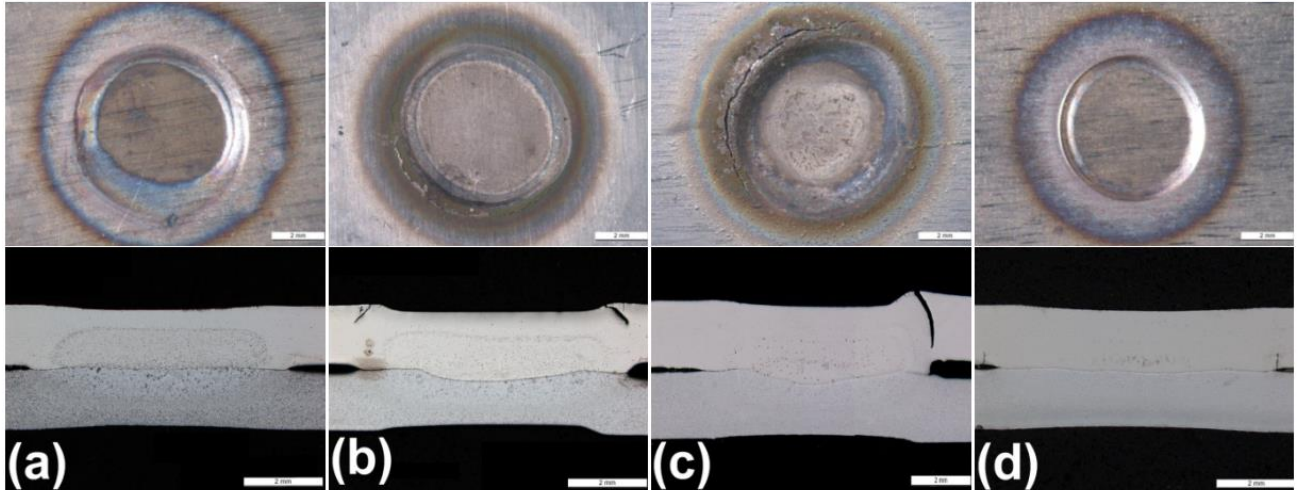
Figure 2.14: Micrographs of RSW welds of TWIP steel (lighter steel) welded to ferritic steel (darker steel). (a) both steels not galvanised, (b) only TWIP steel galvanised, (c) both galvanised and (d) only ferritic galvanised. Showing mm sized cracks in the TWIP steel [9].

As mentioned before, the specific temperature range that creates susceptibility is determined by the specific material. However, in RSW accurately measuring the temperatures during welding is not possible, due to the electrodes needing to be in full contact with the metal, which both prevents the use of thermocouples and the use of thermal imaging to measure temperatures. The images shown in figure 2.14 and 2.15 do show the location where LME occurs during RSW. The cracks form just outside the area of the actual weld zone in the coarse-grained heat-affected zone (HAZ). Two reasons can be identified for the location of LME cracks. Firstly, stresses are high in these zones, both due to temperature effects and due to high shear stresses introduced by the applied compressive electrode force, calculated through SORPAS to be around 130 MPa [10].

Secondly, the shape of the electrode leads to the highest temperatures (around 850°C) on the surface occurring just next to the electrode during the final part of the welding cycle. These temperatures have been calculated using welding simulation software SORPAS as shown in figure 2.16 [10].
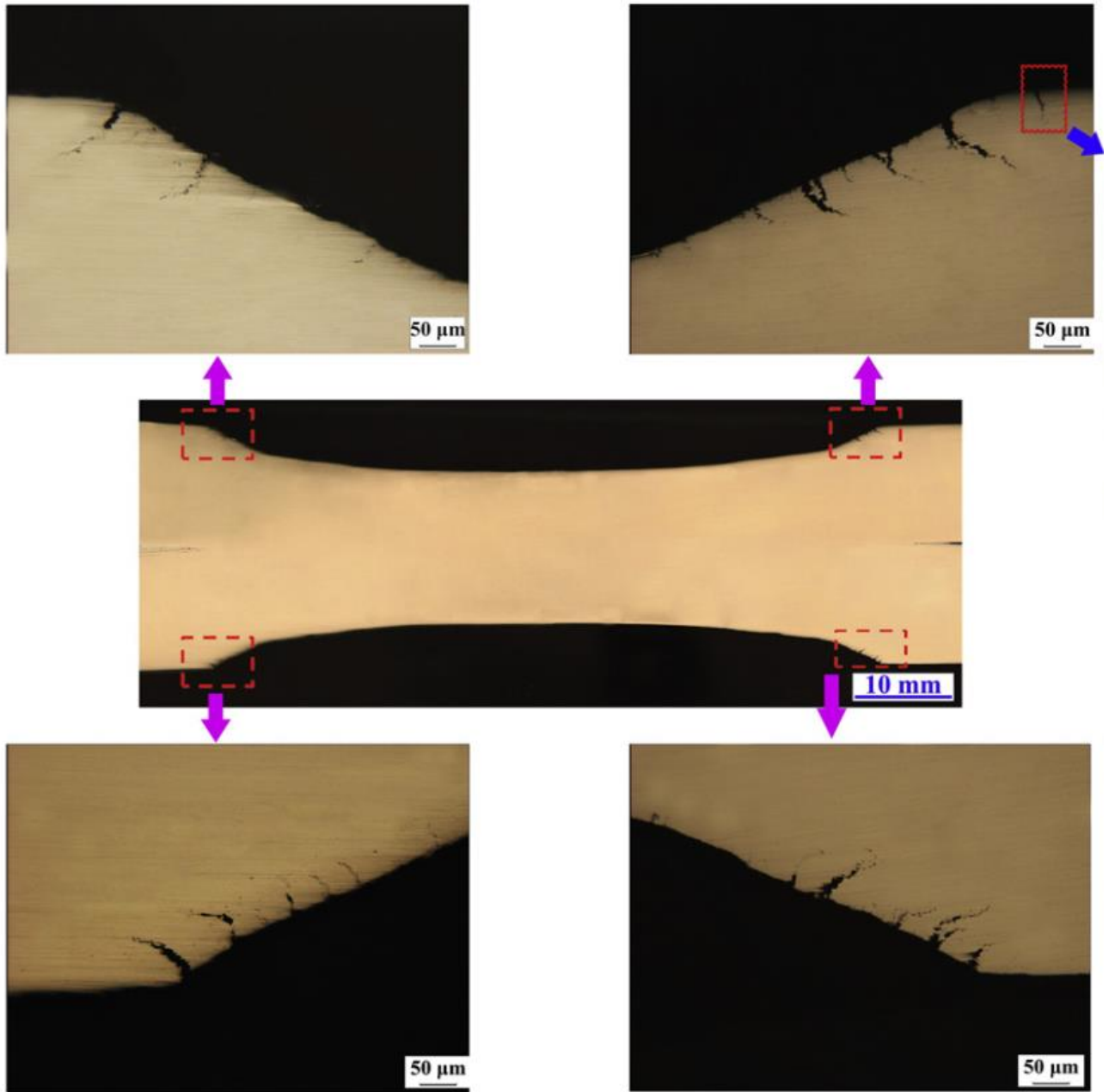
Figure 2.15: Micrometre sized LME cracks [11]
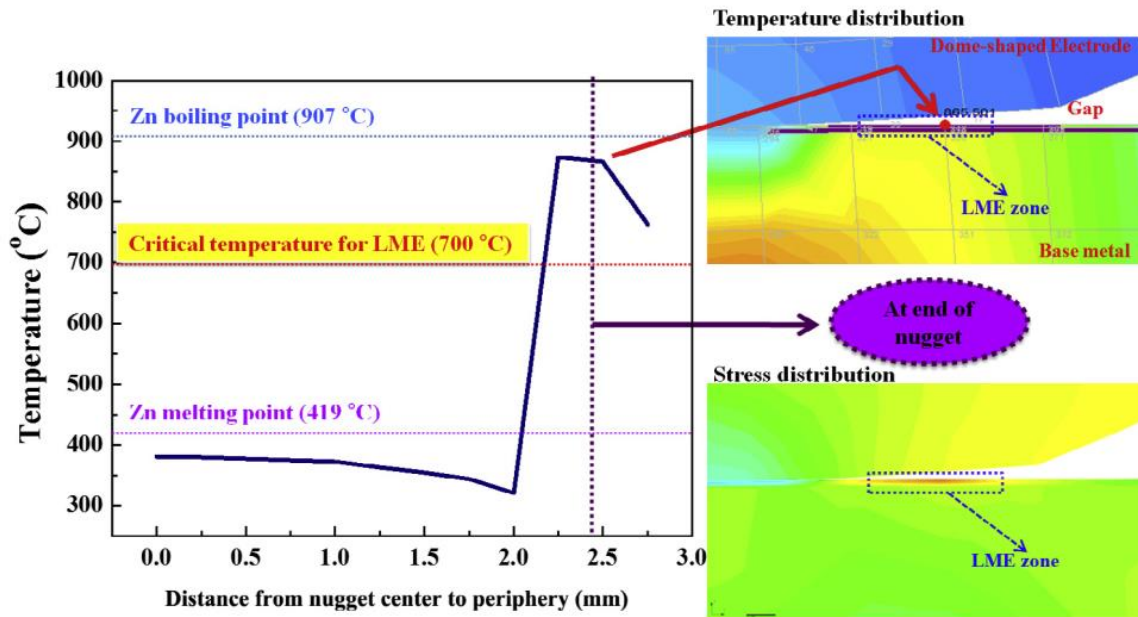
Figure 2.16: Simulation of temperature field around the electrode tip during the last cycle of welding of galvanized TWIP steel with an estimated critical LME temperature [10].

During the earlier stages of welding, LME will not occur, because the temperatures are high enough in the LME zone as indicated in figure 2.16 to melt the base steel. As the steel solidifies, the weld nugget is cooled rapidly due to the cooling water flowing through the electrode. The electrode tip, however, is dome shaped. Just beside the direct contact between the electrode and the metal surface a gap is present where the metal is neither cooled efficiently by the cooling water nor by cooling to the air. In this small area, the temperature will remain in the small intercritical zone for LME for longer times, leading to LME cracks forming in this zone.

Following these findings, studies were performed with the goal of controlling the welding processing parameters to prevent LME. Firstly, a welding pulse schedule was devised that could control the temperature around the weld [11]. As mentioned in section 2.3.1, RSW can only be performed in a narrow weldability lobe for welding current and welding time. When the prevention of LME in this weldability lobe is considered, the weldability lobe was found to be more restricted, as shown in figure 2.17.
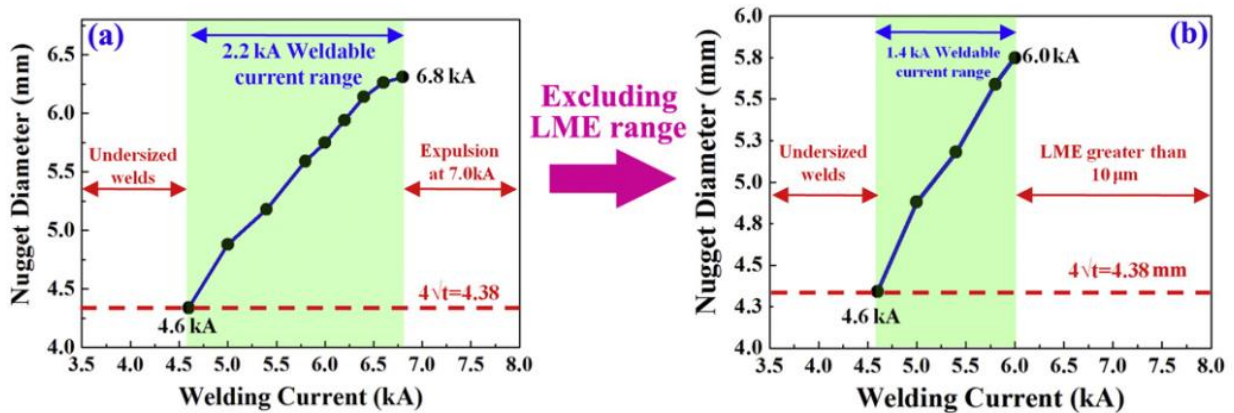
Figure 2.17: Weldability lobes of electrogalvanized TWIP steels with (a) only considering too small welds and expulsion and (b) also considering LME [10].

However, by carefully devising a current pulse schedule, with two welding pulses, a schedule was created where the temperature around the weld was controlled to only reach the minimum welding diameter and a strong corona bond during the first pulse. The second pulse then grows the welding nugget to reach the desired nugget size and form the desired final weld. By using this schedule, the heating rate in the LME susceptible area was controlled and thermal stresses minimised. It was found that LME would only occur during the second pulse [11]. By making the second pulse as short as possible, the welding current leading to LME was pushed to higher currents, thereby preventing LME until the welding schedule would also cause expulsion as shown in figure 2.18.
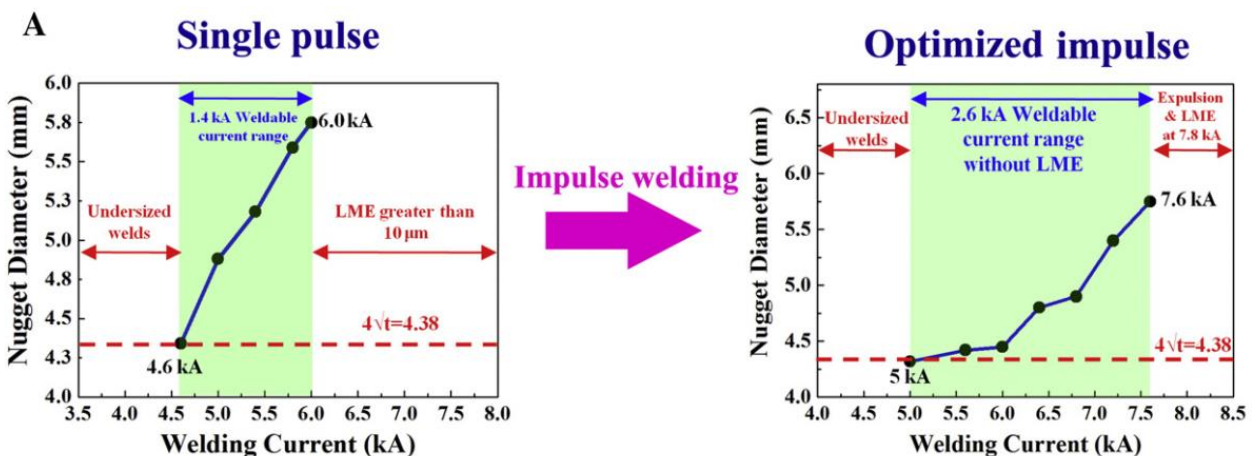
Figure 2.18: Comparison of the weldability lobes of electrogalvanized TWIP steels when using a single pulse and using an optimized multiple impulse schedule [11].

Finally, LME can be suppressed by using larger and flatter electrode caps. By increasing the welding cap diameter, the shear stresses at the edge of the weld will be lower, which reduces the LME susceptible zone. Additionally, the transition where the welded metal is cooled by water to where it is cooled by air will be more gradual around the electrode tip, suppressing the high temperature peaks in the HAZ, again

decreasing the LME susceptible area. Figure 2.19 shows the effect schematically [9].
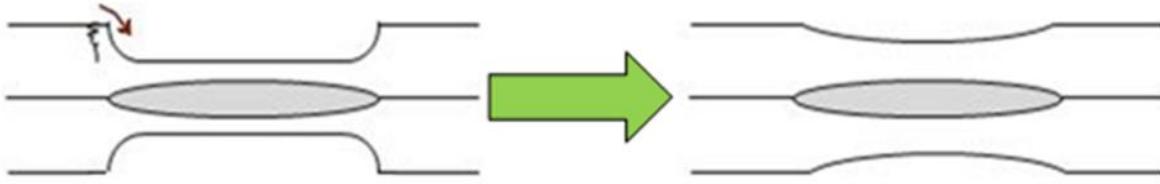
Figure 2.19: Schematic representation of the effect of a larger and flatter electrode cap [9].

2.4 Laser-beam welding

The electrodes used in RSW cover the welded zone preventing the use of most techniques for accurately measuring temperatures during the welding process. Thermocouples cannot be used, since they would touch the electrodes, interfering with the welding. Neither can thermal imaging be utilised because the electrodes cover the surface of interest. A process that could be used to monitor LME crack formation and conditions during welding is laser-beam welding (LBW). By carefully selecting laser welding conditions, especially laser power and travel velocity, and by applying external loads, the conditions in RSW can be approximated while leaving the welded surface visually accessible during welding. This section will introduce the process of LBW and show research that has been conducted regarding LME in LBW.

2.4.1　The process

Laser-beam welding is a process where a concentrated beam of photons of a single wavelength is used to heat up the material to be welded in a localised area. Gases can be used to control side-reactions, such as oxidation, from occurring during interaction of the laser with the material. For example: shielding with argon ensures that no oxides are formed during the time at elevated temperatures. The beam power can be calculated from the selected beam peak intensity and the focused spot size using equation 2.2 [35].

$$P = (\frac{\pi w^2}{2})H_0 \qquad\qquad \text{(eq 2.2)}$$

where P is the delivered laser power, w is the spot size radius on the material and H_0 is the peak intensity of the laser. The total energy delivered into the material depends on the laser absorption coefficient of the material under investigation and can be divided in several energy terms using equation 2.3 [36].

$$C_{absorption}E_{laser} = E_{\Delta T} + E_{rad} + E_{melt} + E_{vapor} \qquad \text{(eq 2.3)}$$

where $E_{\Delta T}$ is the energy translating to an increase in temperature, related to the specific heat capacity, E_{rad} the energy lost by radiation, E_{melt} the latent heat of melting and E_{vapor} the latent heat of vaporization.

Schematically, the process is shown in figure 2.20.
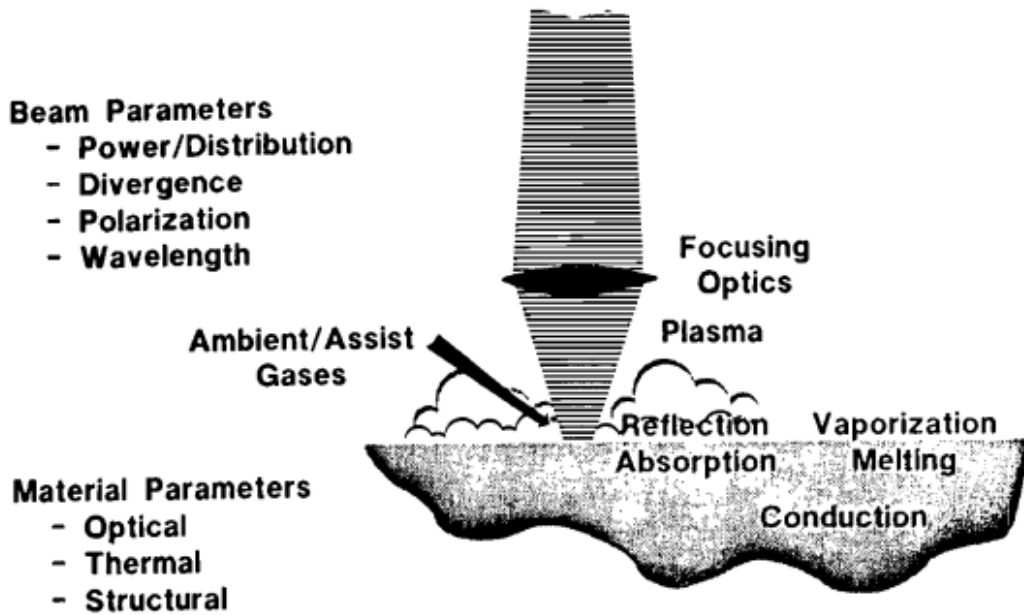
Figure 2.20: Schematic representation of an LBW process [35].

Two main types of laser are used in industry for LBW: CO_2 lasers and Neodymium doped yttrium aluminium garnet crystal (Nd: YAG) lasers. The main difference between the two is the radiation wavelength produced: 10600 nm for CO_2 lasers and 1060 nm for Nd: YAG lasers. Because of the different energies of the two wavelengths, it also translates to the laser powers achievable by the two types: 60 kW and 4 kW for the two types respectively [37]. The absorption efficiency of the process also depends on the wavelength and is approximately 50% for a Nd:YAG laser, compared to 12% for a CO_2 laser [38]. Figure 2.21 shows a laser in use.
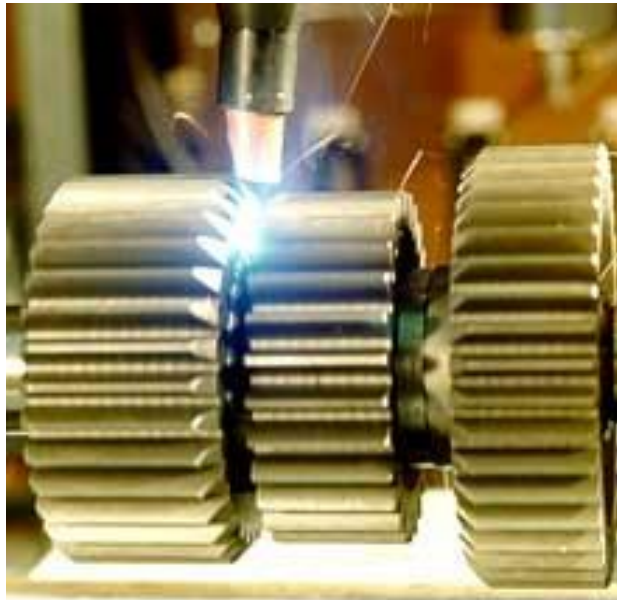
Figure 2.21: CO_2 laser in use for welding of a gear component in the automotive industry [37]

2.4.2   LME in LBW

Laser-beam welding, due to its contactless nature, should enable in-situ imaging of temperature distributions during welding using thermal imaging, as well as local strain field measurements using digital image correlation. By comparing the *in-situ* conditions to LME crack locations after welding, knowledge could be gained on the local thermo-mechanical conditions leading to LME cracking, which could be translatable to RSW applications. Provided LME cracks in LBW grow to a significant size, *in-situ* measurement of crack growth could also be applied.

Figure 2.22 shows an experimental setup allowing for careful control of the laser power, *i.e.,* temperature input, and external applied load.
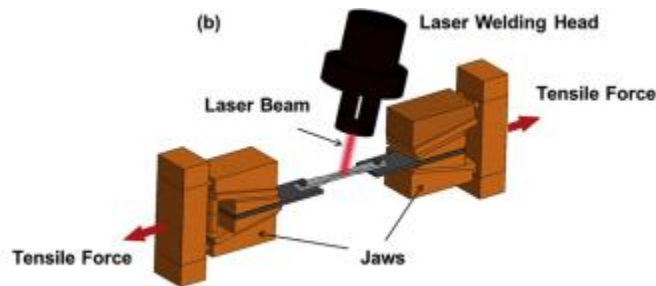
Figure 2.22: Schematic representation of a typical LBW under tensile load experimental setup [39].

Using such a setup, the formation of LME cracks in LBW was confirmed [39]. However, unless using highly extreme conditions, close to fracture load, formed LME cracks were extremely small, only a few microns in length. An example is shown in figure 2.23. Cracks were identified as being LME cracks when a significant amount of Zinc was found on the crack surface, as this implied liquid zinc penetration into the crack without significant diffusion of zinc into the bulk steel [39]. By increasing the applied tensile stress to well above the yield strength at room temperature, LME cracks were observed to have grown longer, allowing for more detailed examination. The LME crack length dependence on applied stress during welding is shown in figure 2.24.
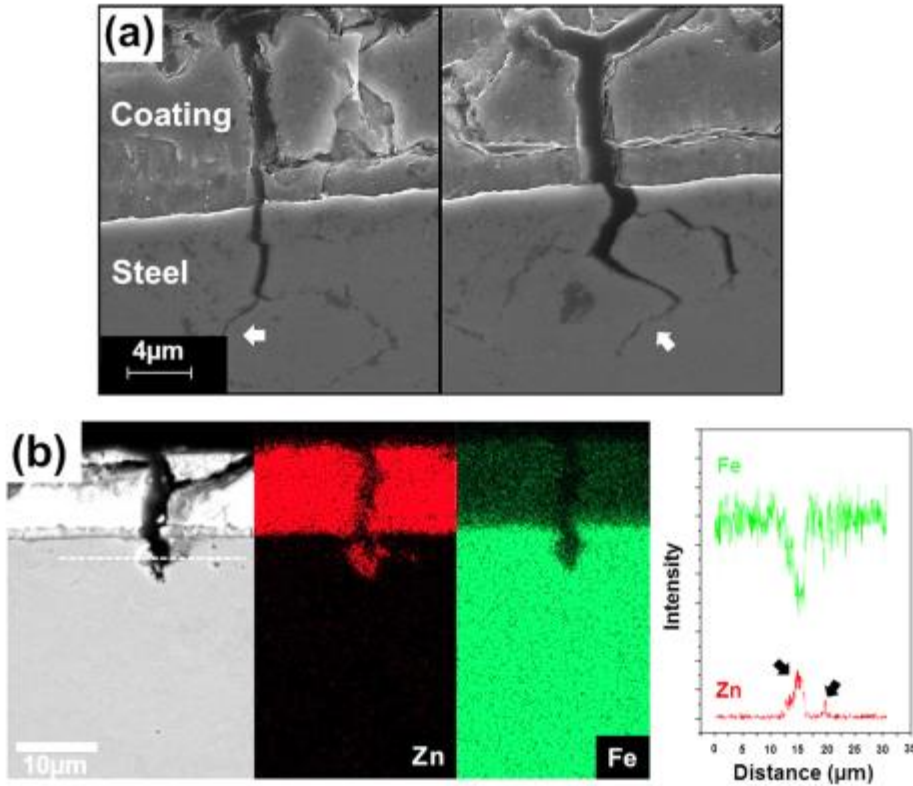
Figure 2.23: SEM micrographs of the Zn-coating/Steel interface of a Boron steel LBW under tension sample, combined with EPMA map, showing LME cracks filled with Zinc. [39]
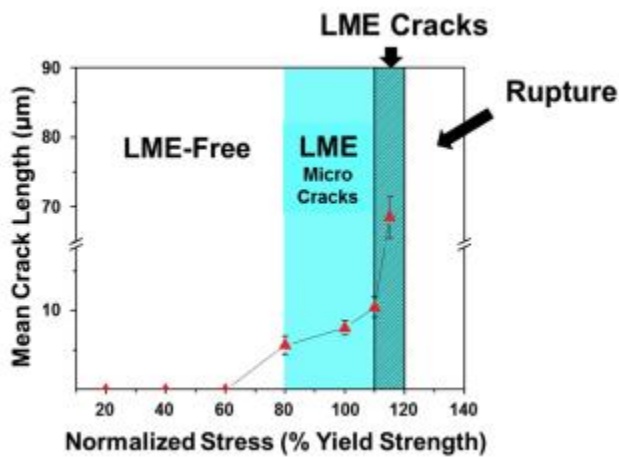
Figure 2.24: Mean LME crack length as a function of applied tensile stress during LBW under tension, showing the narrow zone where characterizable LME cracks are formed [39].

Like LME cracking in RSW, cracks were only observed in a very narrow region, namely the upper-critical heat affected zone (UCHAZ) directly adjacent to the weld line, where the temperature reaches between 850 and 900°C. This UCHAZ was only a few tens of microns wide [39]. The occurrence of LME in such small regions of a weld implies that extremely specific conditions are necessary for LME to occur.

Finally, using EBSD measurements, by identifying prior austenite grain boundaries (PAGBs) in the cooled specimen, it was confirmed that LME crack growth occurred intergranular in the austenite grains as shown in figure 2.25. The combination of zinc present in cracks and the growth of cracks along prior austenite grain boundaries confirms that the cracks are a result of LME, as explained by the atomic scale mechanism of LME in section 2.1.2.
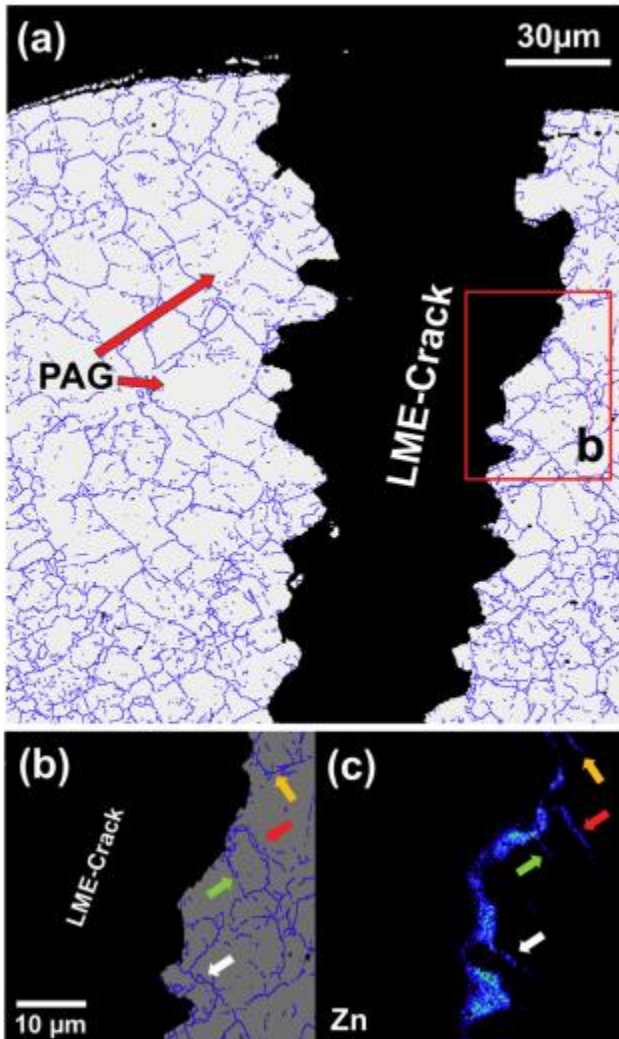
Figure 2.25: Modified EBSD map showing PAGs surrounding a larger LME crack in an LBW sample along with EPMA maps showing zinc penetration into the PAGBs [39].

2.5   Macroscopic thermo-mechanical conditions

All previously mentioned welding methods only showed LME crack formation at specific stress states and temperatures. These results show that specific conditions are needed for LME cracking. Using highly controlled hot tensile testing, the required conditions can be determined on a more macroscopic scale. Although little information is gained about the microscopic thermo-mechanical conditions, the macroscopic studies do provide a general idea of the requirements. By comparing non-zinc coated specimens and galvanised specimens under the same hot tensile testing conditions, the degree of liquid metal embrittlement can be determined by comparing the fracture energies. Figure 2.26 shows a typical ductility trough for LME at different strain rates. The ductility trough shows the relative reduction of fracture energy of the coated specimen as compared to the bare specimen. Such a ductility trough is one of the ways embrittlement can be shown.
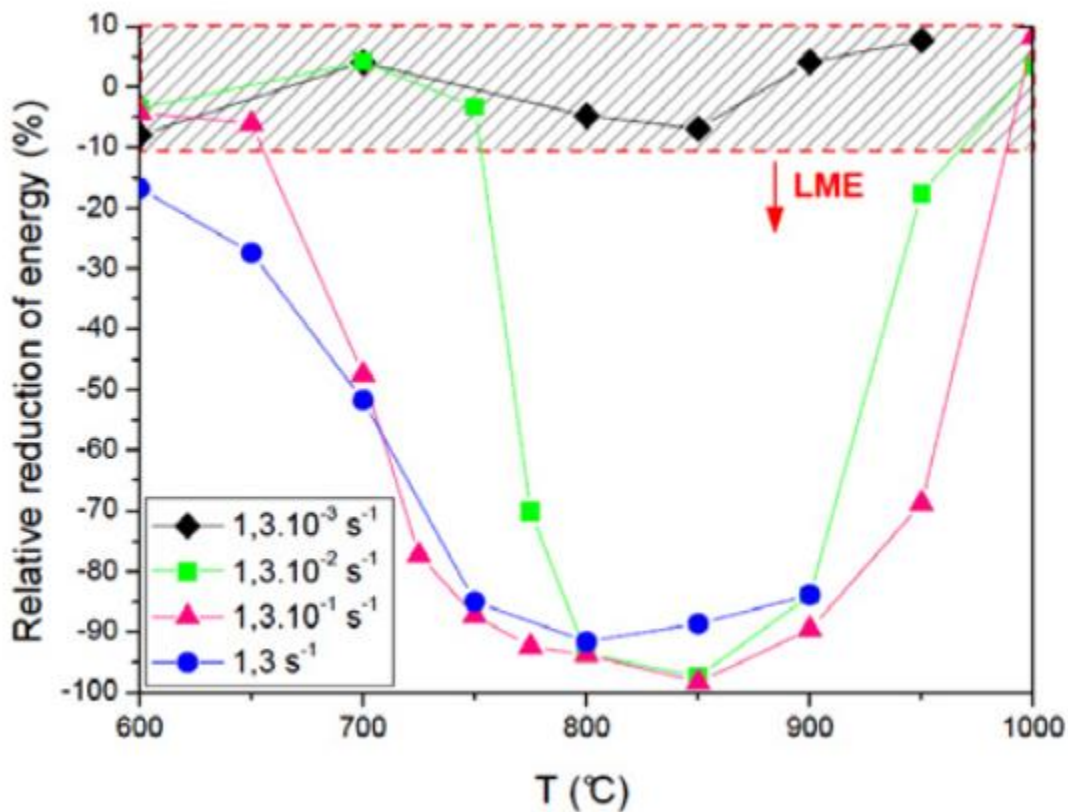
Figure 2.26: Ductility trough of galvanised TWIP steel for different strain rates in hot tensile testing [40]

The ductility troughs show three aspects of the occurrence of LME [40].

Firstly, a lower temperature limit exists. In the case of the TWIP steel, this lower limit is between 600 and 700 °C. The lower temperature limit is related to the increase in grain boundary energy of the austenite grains as the temperature increases. At a certain temperature the cohesion of the grains becomes low enough for the liquid zinc to penetrate the grain boundary and start the LME process.

Secondly, an upper temperature limit around 900 °C can be identified. This upper limit is not related to the solid metal, but rather to the presence of liquid metal. The evaporation point of Zinc is around 907 °C [41]. Above this point, the zinc will evaporate. Since the zinc layer is only a few microns thick, the zinc will evaporate quickly, leaving no zinc for embrittlement. The embrittling effect starts to decrease slightly before the actual boiling point of zinc, because necking causes the local temperature to increase above the overall temperature.

Lastly, the strain rate applied to the sample has an important effect on the embrittling capacity of the zinc. At low strain rates ($1.3*10^{-3}$ s^{-1}) no embrittling can be observed at all. As the strain rate increases, more embrittling is seen. This implies that the dynamic or static nature of a certain set of conditions determines whether embrittling occurs.

2.6   Summary

Many studies on the topic of LME have been performed [3] [4] [5] [6] [14] [15] [16] [17] [18] [21] [22] [23] [24] [40] [42]. Historically, as mentioned before, the underlying mechanisms of LME were studied on an Al-Ga pair.

Multiple more engineering-oriented studies have been performed on the thermo-mechanical LME behaviour in a slightly different system. Namely, steel in contact with a liquid Lead-Bismuth eutectic that occurs in the reactor cores of generation IV liquid metal nuclear reactors [5] [6] [43]. Although, the liquid environment is different in these studies and the contact between solid and liquid metal occurs for longer times, an important aspect can be found. The embrittlement does not occur immediately at a temperature where the embrittling metal becomes liquid. A higher temperature is often needed in steels before the liquid metal penetrates the grain boundaries and causes embrittlement [43]. This effect is shown in figure 2.27 where fracture energy (the area under the stress-strain curve) only drops significantly at a higher temperature.
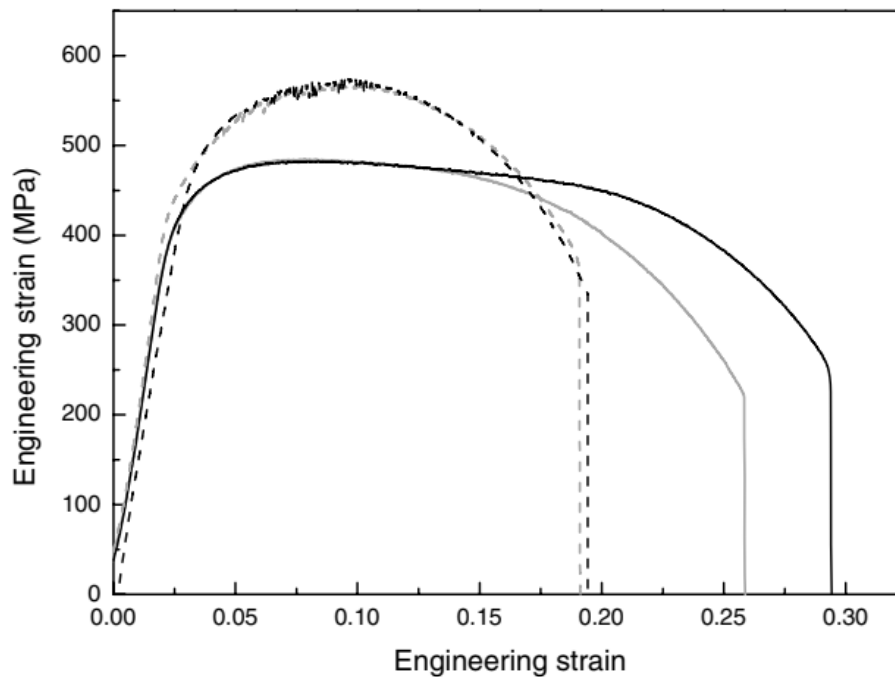
Figure 2.27: Engineering stress-strain curves of T91 martensitic steel pre-exposed to liquid lead-bismuth (grey lines) and not exposed to liquid lead-bismuth (black lines) at 300 °C (dashed lines) and 450 °C (solid lines) [43].

Studies have also been shown investigating LME occurrence during RSW [9] [10] [11] [12] [30]. Mechanisms, LME susceptible areas around a RSW and welding parameters leading to LME susceptible conditions in the susceptible area have been studied and shown. Specific RSW processing parameters avoiding LME have also been shown. A difficulty has been identified in achieving further investigation and characterisation of LME in RSW: the electrodes used in RSW cover the welded area, making *in-situ* characterisation of LME during welding impossible.

LBW has been proposed as an alternative method to characterise LME in hot-dip galvanised steel. The occurrence of LME in LBW under tension samples has been shown and the effect of several macroscopic thermo-mechanical conditions (temperature, strain rate, stress) has been explored. However, several questions are still unanswered relating to the applicability of LBW to study *in-situ* LME:

LME in LBW has only been shown in prepared LBW sample cross-sections, studied using time-consuming analysis techniques such as SEM, EBSD and EPMA. Even if LME occurs during an LBW under tension test, it is unknown if the LME crack growth can be identified at a surface level during welding.

The severity of LME, especially in LBW, has only been stated in terms of LME crack lengths. Little is stated about amount or density of LME cracks. If cracks penetrate deep into the material, but only a few cracks grow, again it is unknown if they can be identified *in-situ*.

Finally, the conditions leading to LME in RSW, LBW and using hot-tensile testing, have only been analysed regarding the respective technique used. Comparisons of the conditions are not made. Therefore, the applicability of one technique to analyse a different technique (*i.e.,* LME in LBW under tension to study LME in RSW) is still unknown.

3. Methods and Materials

This section deals with the methods and materials used in this study. Firstly, the properties of the investigated steel will be presented. Secondly, the experimental setup used for Gleeble testing and laser-beam welding under tension will be discussed. This is followed by the approach of analysis of tested samples. Finally, a thermo-mechanical model is outlined, which allows approximations of temperature and stresses for both the experimental setups applied in this study to be made.

3.1 DP steel

The material under investigation is a hot-dip galvanized dual-phase steel with a UTS above 1000 MPa. The steel was obtained in 300 x 400 mm^2 sheets with a thickness of 1.3 mm, from which specimens for testing were cut, as will be outlined in the experimental setup subsections. The chemical composition of the steel was known, but not shown here due to confidentiality.

Indications of the mechanical properties of the steel are shown in table 3.1. This data is used for normalisation purposes of later experimental parameters, i.e., a load applied during testing as a percentage of yield strength of the as received material.

Table 3.1: Indications of the mechanical properties from uniaxial tensile testing of the DP1000 steel.

Property	Value
Young's Modulus	> 195 GPa
Yield Strength (p0.2)	> 650 MPa
Tensile Strength	> 1000 MPa
Maximum elongation	> 10 %

SED 20.0kV WD11mm P.C.60   x300   50µm
TU Delft
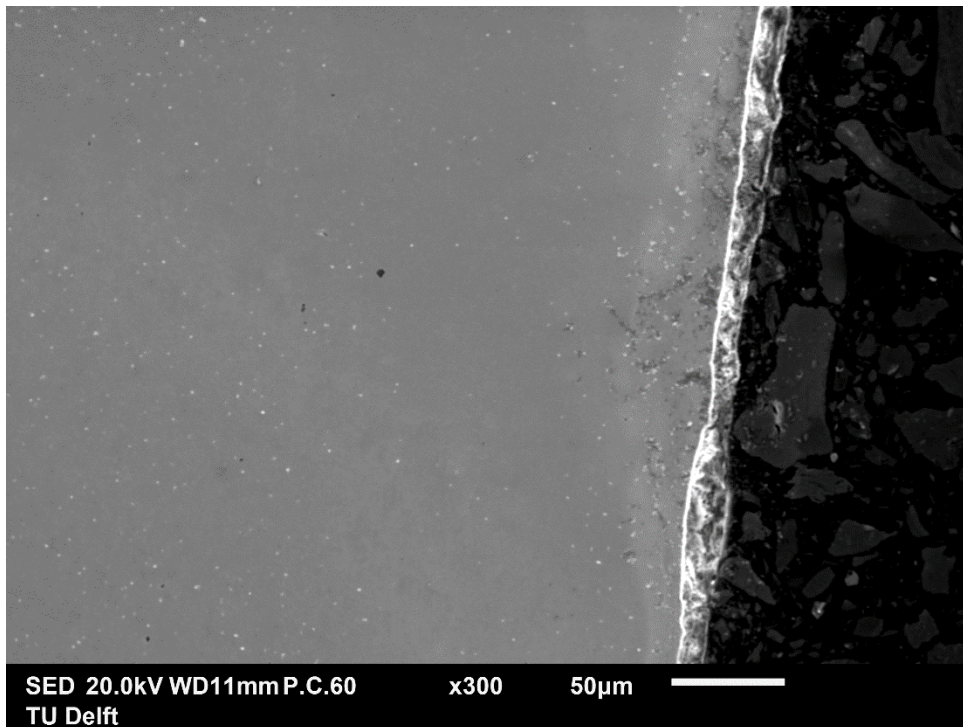
Figure 3.1: SEM micrograph of the zinc coating as delivered.

The thickness of the zinc-coating, as shown in figure 3.1, was determined by SEM microscopy to be 18±2.8 µm.

3.2 Gleeble experimental setup

As mention in chapter 2 a wide variety of experimental conditions have an influence on the embrittling effect by the liquid zinc. Therefore, a thermo-mechanical simulator i.e., a Gleeble 3500 was used to methodically investigate different thermo-mechanical conditions.

A Gleeble experimental setup can be used to investigate the effects of global thermo-mechanical conditions, due to the high degree of control over thermo-mechanical conditions. Stresses, strains, or strain rates can be prescribed accurately through a hydraulically controlled load cell. Temperatures are controlled through thermo-couples and the material is heated through joule heating, creating a homogeneous temperature zone in the centre of the sample.

Samples were cut from the provided steel sheets using shear cutting. A rectangular sample of 20 mm width and 125 mm length was chosen. Holes are punched in both ends of the rectangle, 10 mm from all

edges, with a diameter of 5 mm. Because the highest temperatures in Gleeble testing are present in the centre of the sample, this simple rectangular sample will not produce irregularities during tensile testing. The cracks were expected to form consistently in the middle of the gauge length, as the higher temperatures significantly weaken the steel. Additionally, the high temperatures will negate the edge effects created by the shearing process. A schematic image of the Gleeble sample is shown in figure 3.2.
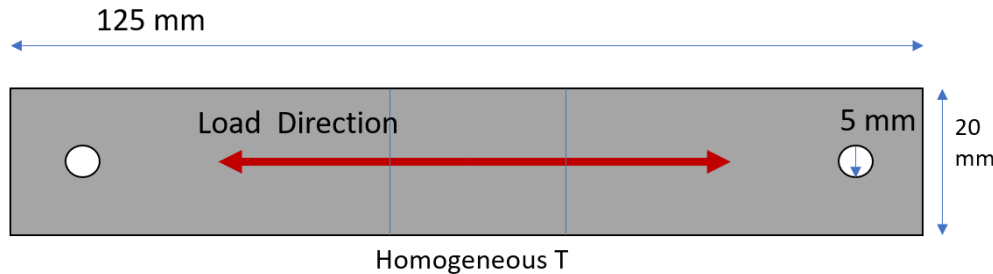
Figure 3.2: Schematic representation of Gleeble sample

For control purposes and reference specimens were prepared from which the zinc-coating was removed by submersion in 37% HCl for 1 minute, or until hydrogen gas formation was significantly reduced (indicating oxidation of iron instead of zinc).

Gleeble testing was carried out using a nitrogen shielding gas to avoid oxidation of the zinc or steel during the higher temperature operations. The temperature at the centre was measured and controlled using type K thermocouples spot welded to the sample. Firstly, the ductility trough was determined by testing at a range of temperatures from 600-950 °C and a displacement speed of 2 mm/s. This displacement speed was converted into a strain rate using a gauge length of 15 mm, as 15 mm is the length of material homogenised to the set temperature. With this gauge length, the used strain rate was 0.13 s^{-1}. The heating rate was 80 °C/s. After heating to the required temperature, the sample was held for 10 s to allow for homogenising the temperature before loading started. After failure of the sample, it was cooled through air-cooling.

After the temperature range was tested, the temperature that led to the highest degree of visual embrittlement (as shown in Appendix A) was chosen to investigate subsequent parameters, i.e., strain rate and holding time. Based on the temperature experiments 850 °C was determined to create the clearest embrittlement through visual observation. Subsequently, strain rate was varied from 1.3*10^{-3} to 1.3 s^{-1} at 850 °C. Finally, the effect of the holding time on LME was investigated. The holding time is defined as the time between the temperature reaching the setting and commencing the displacement.

3.3 LBW experimental setup

Laser-beam welding under tension was performed using the Y: YAG laser at the 3me faculty of TUDelft. A maximum laser power of 8 kW can be achieved. A focused beam with a spot diameter of 0.2 mm was applied. The provided steel sheets are cut into tensile dog bone samples with dimensions as shown in table 3.2 and figure 3.3, complying to the ASTM E8 tensile testing standard [44]

Table 3.2: Dimensions of dog-bone sample used for laser-beam welding under tension.

Dimension	Symbol	Dimensions (mm)
Gauge length	Lgauge	50
Width	W	12.5
Thickness	t	1.3
Radius of fillet	rf	13
Length of reduced parallel section	Lr	57
Length of grip section	Lg	50
Width of grip section	Wg	40
Diameter of hole	D	13
Edge distance from pin	Lb	30
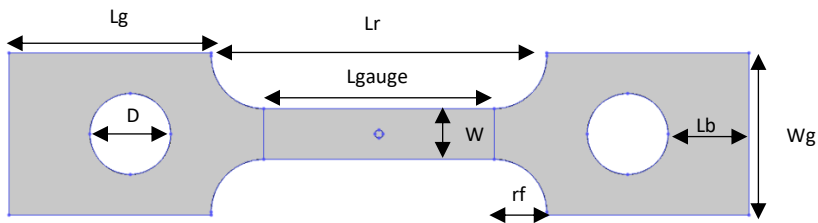
Figure 3.3: Schematic view of LBW sample, with section marked with symbols from table 3.2.

Before activating the laser, samples are pre-loaded manually, controlled and measured using a load cell. Samples are loaded to loads corresponding to 80, 100 and 120 % of the yield strength. Considering the sample dimensions this corresponds to loads of 5240, 6550 and 7861 N, respectively.

After loading, samples are laser-welded using different welding parameters. Laser powers of 600, 700, 800, 1000, 1500 and 2000 W are used. The laser spot size was defocussed to a diameter of 1 or 2 mm to prevent keyhole formation and achieve a more homogeneous temperature surrounding the weld. These conditions lead to a larger heat-affected zone, i.e., a larger area susceptible to LME. Different welding times are used to investigate LME, varying from 0.5 s at higher laser powers to 15 s at lower laser powers. Temperature was measured using thermocouples spot-welded as close as possible to the heat-affected zone, approximately 10 mm from the fusion line.

3.4 Material Characterisation

Samples obtained from Gleeble and LBW testing were prepared for microstructural characterisation. Gleeble samples were cross sectioned along the loading axis. The LBW samples were first analysed visually and using a VHX-5000 digital microscope. Features resembling LME were identified on the surface and cross-sections were made through these features to investigate whether these features could be classified as LME.
Cross sections are made using a Struers cyclotom-6 at 60 Hz and a cutting velocity of 0.2 mm/s. Cross-sectioning directions are shown for Gleeble testing figures 3.4.
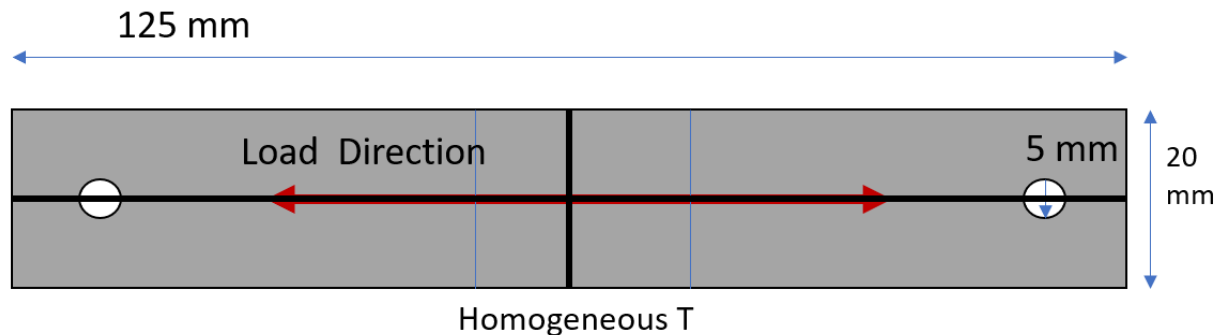
Figure 3.4: Cross-sectioning direction of Gleeble samples indicated by the thick black solid lines.

After cross-sectioning, samples were mounted in conductive hot-mounting resin for use in the scanning electron microscope (SEM) using a Struers labopress 3 at 2.5 kN pressure, 150 °C, with a heating time of 6 minutes and a cooling time of 10 minutes. Mounted samples were ground and polished using Struers Labopol 21, with decreasing coarseness until 1 μm.

mm scaled features of cross-sectioned samples were investigated using optical microscopy controlled with analysis auto software and samples with likely LME features were selected for further microstructural analysis. Polished samples were microstructurally investigated using a JEOL tabletop SEM with an acceleration voltage of 20 keV and 50% probe current (P.C.) and elemental analyses are performed with energy-dispersive x-ray spectroscopy (EDS) using 60% P.C. Additionally, samples were etched before SEM analysis to reveal microstructural features using 1% nital solution for 60s.

3.5 COMSOL model

The two experimental setups addressed before, Gleeble testing and LBW under tension, result in different conditions that may potentially lead to LME.
On the one hand, in LBW, the temperature distribution is highly heterogeneous with temperature peaks being localised in the centre of the sample. In addition, the external loading is completely static. Therefore, potential LME conditions will be a combination the static external stress and the more dynamic

thermal stresses. For LME to occur, this complex stress state should combine with areas having an appropriate temperature range during welding.

On the other hand, LME in Gleeble hot tensile testing involves the homogenisation of a pre-set maximum temperature and a uniform strain rate. The final stress state will therefore be mostly controlled by the strain rate, as the temperature gradient will be relatively small over the gauge length, therefore only small thermal stresses will arise. These stress states will also be less localised, instead acting on the entire homogeneous temperature are before to be susceptible to LME.

Finite element models (FEM) were constructed in COMSOL Multiphysics® version 5.3 to analyse the local thermo-mechanical conditions for both experimental setups. The models are validated by experimentally obtained results. Results from COMSOL modelling allow for identification of the thermo-mechanical conditions at LME susceptible locations, where obtaining experimental results is not possible.

Material properties used in the models are approximated for a bare DP1000 specimen. The thin zinc coating is not expected to add to the mechanical performance of the specimen, so it is neglected for simplification purposes. Material properties for the steel are shown in table 3.3. Solver settings and mesh are automatically generated by the COMSOL software, based on the physics, set to a normal mesh size.

Table 3.3: Material properties used in COMSOL modelling.

Property	Value or equation
Young's Modulus	$2.109875E11 + 3.572844E7 \cdot T^{\wedge}1 - 106319.6 \cdot T^{\wedge}2$ Pa
Yield strength	788 MPa for T<500K, 543 MPa for 500K<T<850 K and 116 MPa for T>850K
Tangent Modulus	2500 MPa
Laser absorbance	21%
Coefficient of thermal expansion	$1 \cdot 10^{\wedge}-23 \cdot T^{\wedge}6 - 6 \cdot 10^{\wedge}-20 \cdot T^{\wedge}5 + 7 \cdot 10^{\wedge}-17 \cdot T^{\wedge}4 - 1 \cdot 10^{\wedge}-14 \cdot T^{\wedge}3 - 4 \cdot 10^{\wedge}-11 \cdot T^{\wedge}2 + 3 \cdot 10^{\wedge}-8 \cdot T + 7 \cdot 10^{\wedge}-6$ 1/K
Thermal conductivity	17.3 W/(m·K)
Heat capacity	460.548 J/(kg·K)
Conductive heat transfer coefficient	7.9 W/(m^2·K)

3.5.1 Gleeble COMSOL model

A model to evaluate the Gleeble hot tensile samples, used in the experimental part, was built using the COMSOL 3D geometry functions. The final geometry used for modelling is shown in figure 3.5. The thermal and mechanical physics modules were applied to the model. For simplification, the temperature of the homogeneous part of the sample is not introduced via joule heating, but by applying a heating rate to the homogeneous part until the set temperature is reached. When this temperature is reached, the holding time of the specific experiment is added before a fixed displacement velocity is applied. The boundary condition for the thermal model is heat transfer to room temperature air for all surfaces except the homogeneous temperature zone. For the mechanical model, one side is set fixed (area from the short edge of the sample to the first line) and the displacement is applied on the same area at the other side of

the sample. The middle of the homogeneous temperature zone is evaluated to retrieve values of temperature and stress, as the values in the entirety of the homogeneous temperature zone are comparable. The mesh generated by COMSOL is shown in figure 3.6.
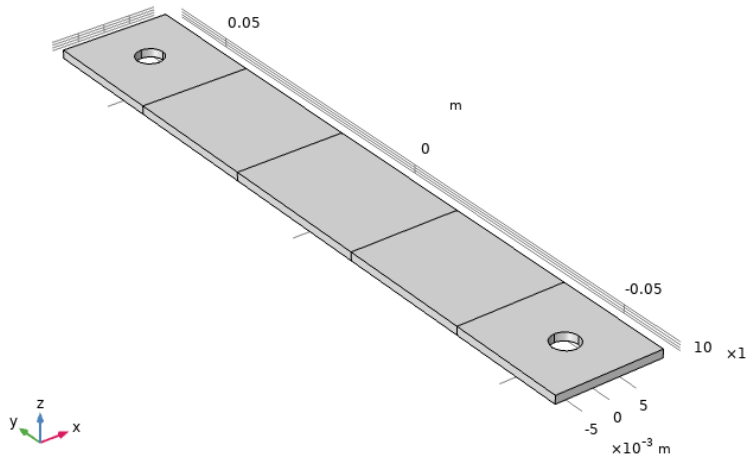
Figure 3.5: Geometry used for COMSOL Gleeble FEA model.
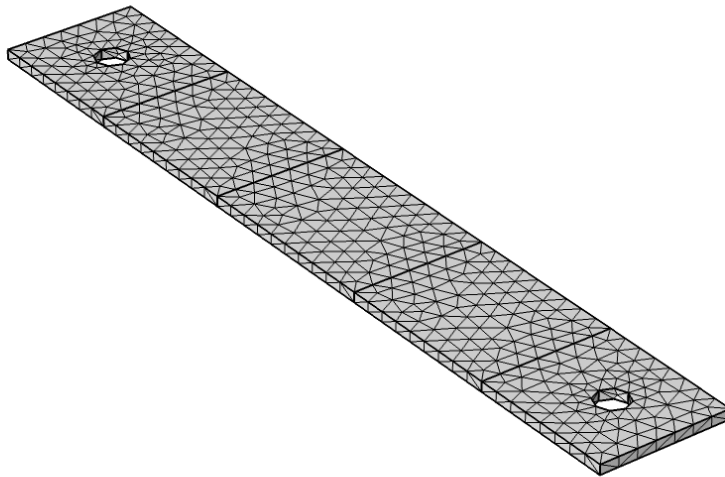
Figure 3.6: Mesh of Gleeble specimen as generated by COMSOL Multiphysics software.

3.5.2 LBW COMSOL model

The same modules used for the Gleeble samples were used for LBW samples. The dog-bone geometry used in the model is shown in figure 3.7. The model initially applies a tensile load equal to the percentage of the yield strength as used in the experiments, using a ramping function to the outer edges of one hole, while the other hole is set fixed. After the test load is reached, the new positions of the holes of the dog-bone specimen are redefined and set fixed, simulating the rods holding the specimen in

place. After this stage the laser power is turned on. The heat input is introduced by applying a deposited laser power over a circular area, using an absorption coefficient of 0.21, while the other areas are marked with heat transfer to room temperature air boundary conditions. Values of stress, strain and temperature are retrieved 1.5-2 mm from the centre of the deposited beam which is approximately the area of the HAZ. Simulation is run for the duration the laser is on, since LME is not expected to occur during cooling, because the thermal gradient will be more gradual than during heating, creating significantly lower thermal stresses. The mesh generated by COMSOL is shown in figure 3.8.
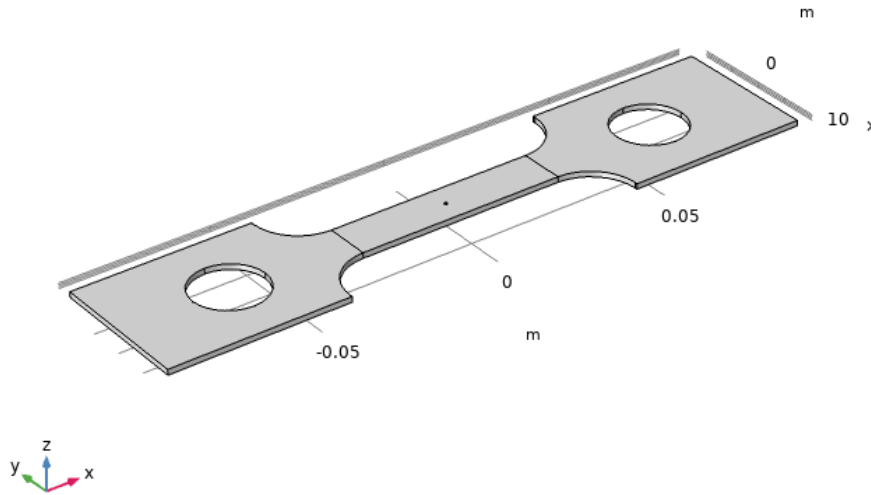
Figure 3.7: Geometry of dog-bone sample used for LBW COMSOL FEA.
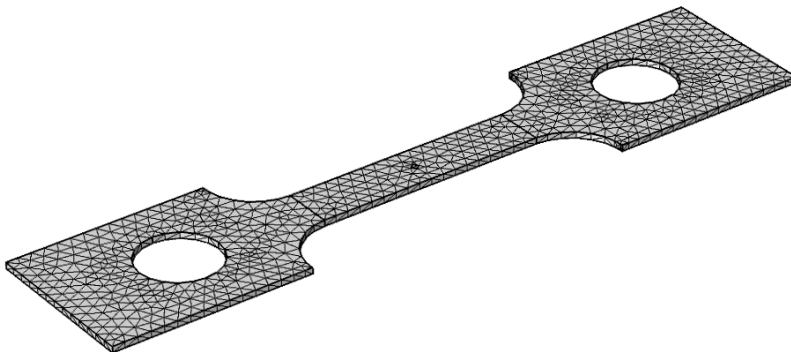
Figure 3.8: Mesh of LBW specimen as generated by COMSOL Multiphysics software.

4. Results

In this section, the quantitative and qualitative results obtained from the different experiments will be presented. First, the quantitative results of the Gleeble hot tensile tests are shown, followed by the material characterisation results. Finally, the same structure is followed for the LBW results.

4.1 Gleeble results

4.1.1 Quantitative

Results of the Gleeble hot tensile tests were obtained in the form of stress-strain curves. Several typical stress-strain curves obtained from the Gleeble tests are shown in figure 4.1, for both uncoated and coated specimens at a range of different temperatures.
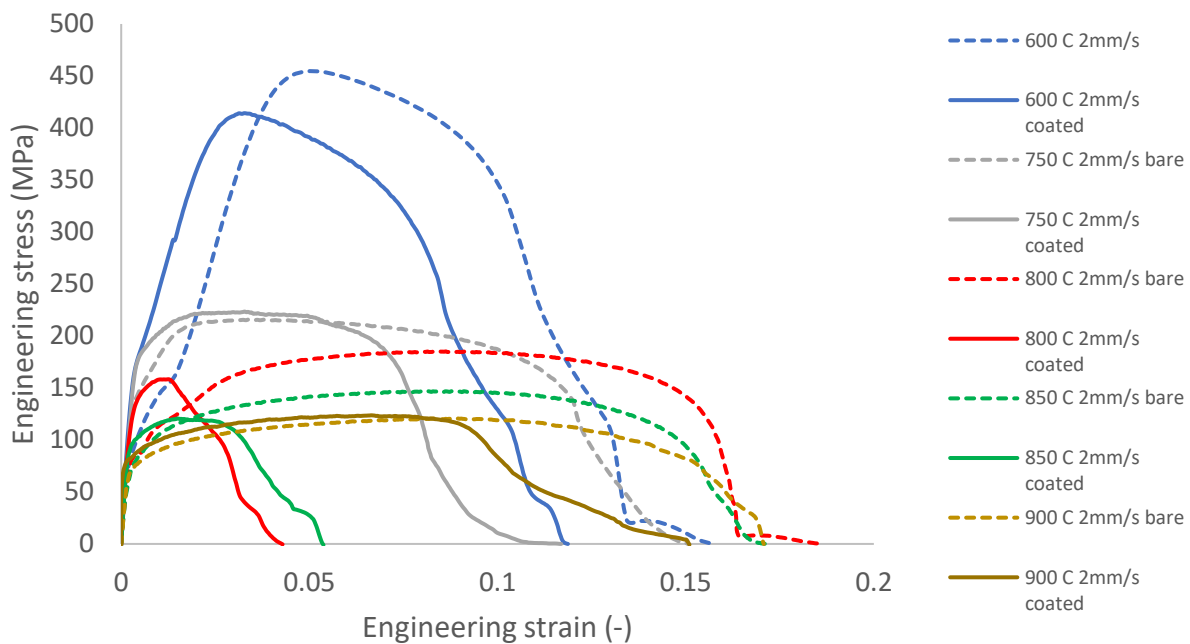
Figure 4.1: Typical obtained Gleeble stress-strain curves at different temperatures, comparing bare (dotted lines) and coated (solid lines) specimens at the same temperatures, strain rate and holding time.

By comparing the stress-strain curves of uncoated and coated specimens, the fracture energy was calculated using an approximate integration of the stress-strain curves to obtain the area under the curve. By calculating the fracture energy for the sample at each set of experimental parameters for both uncoated and coated specimens, the relative fracture toughness of the coated sample in respect to the bare sample is calculated. This relative fracture toughness is plotted as a function of temperature, hold time and strain rate in figures 4.2, 4.3 and 4.4, respectively. Error-bars are added, representing the deviation obtained from repeating the experiments at least three times. In the case of temperature,

applied strain rate was 0.13 s^{-1} and the hold time 10 s. In the case of strain rate, temperature was 850 °C and hold time 10 s. In the case of hold time strain rate was 0.13 s^{-1} and temperature 850 °C
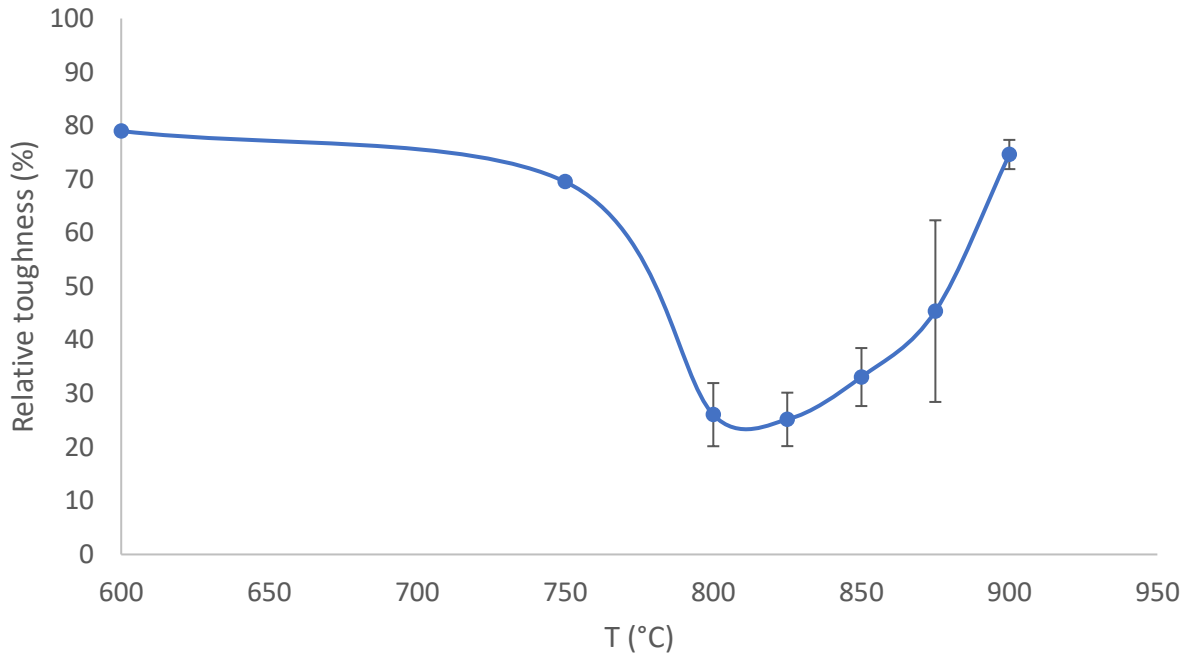
Figure 4.2: Relative fracture toughness of coated samples as a function of homogeneous temperature in Gleeble hot tensile tests, with a constant strain rate of 0.13 s^{-1} and a constant hold time of 10 s.
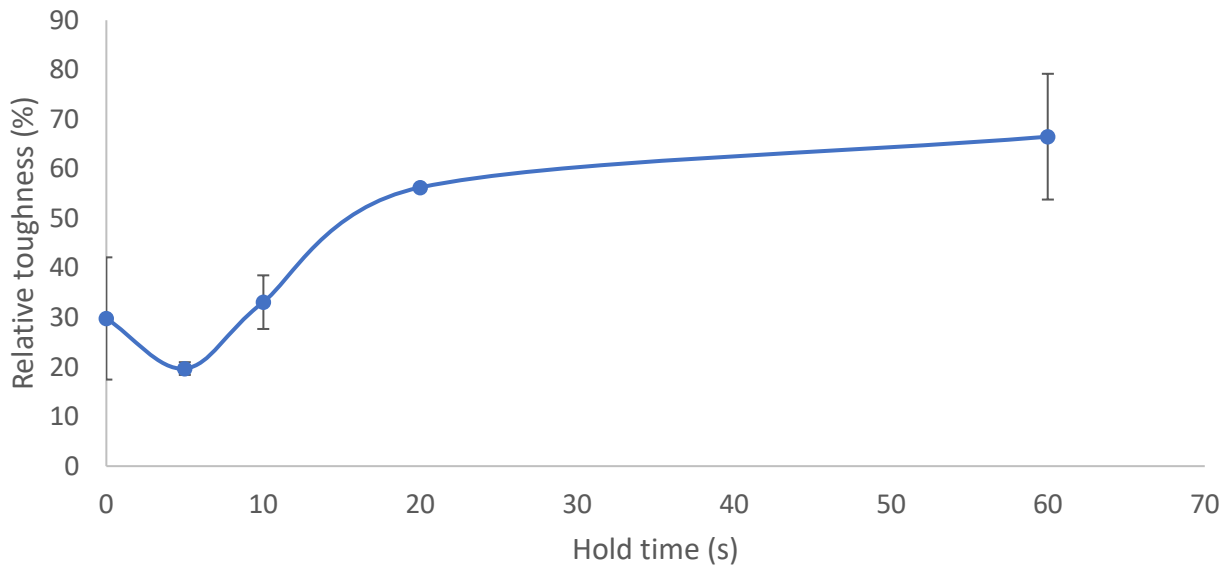
Figure 4.3: Relative fracture toughness of coated samples as a function of holding time at homogeneous temperature before applying strain rate in Gleeble hot tensile tests, with a constant strain rate of 0.13 s^{-1} and a constant temperature of 850 °C.
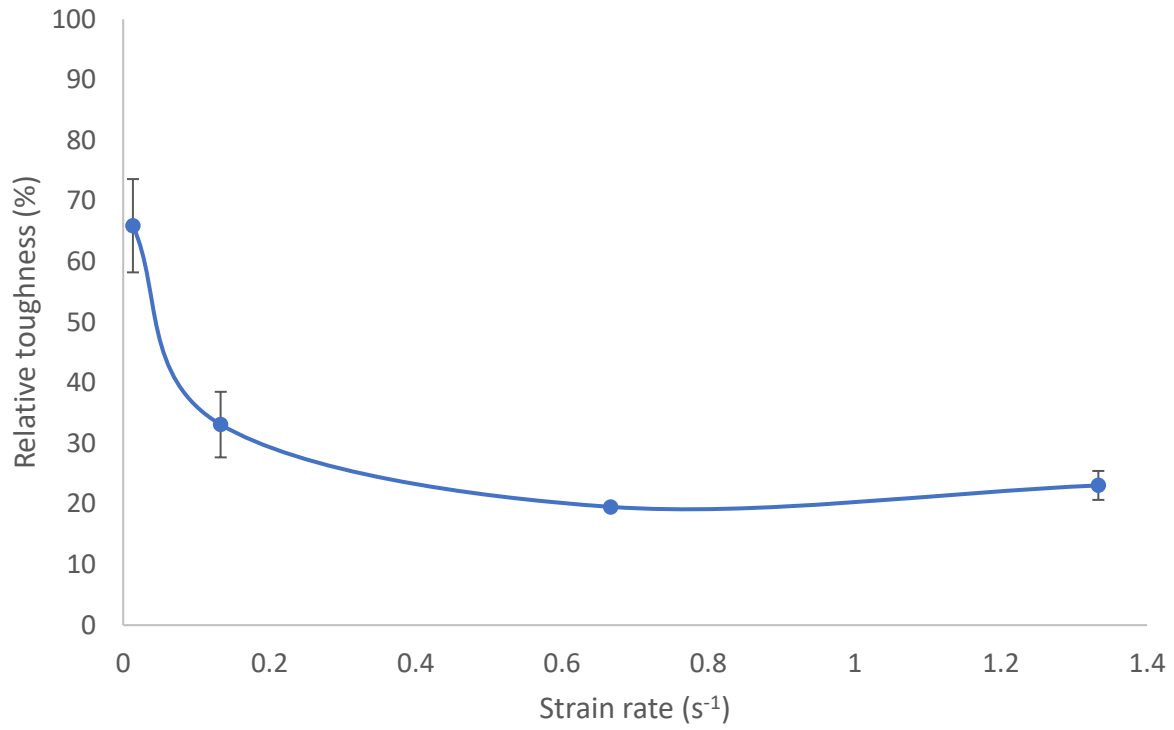
Figure 4.4: Relative fracture toughness of coated samples as a function of applied strain rate in Gleeble hot tensile tests, with a constant temperature of 850 °C and a constant hold time of 10 s.

4.1.2 Characterisation

Samples subjected to Gleeble hot tensile testing were investigated using SEM. Representative results of characterisation are presented in this section for several test conditions. More results can be found in appendix B. Figure 4.5 shows SEM micrographs of a bare and coated sample at 850 °C, a strain rate of 0.13 s^{-1} and a hold time of 10s.
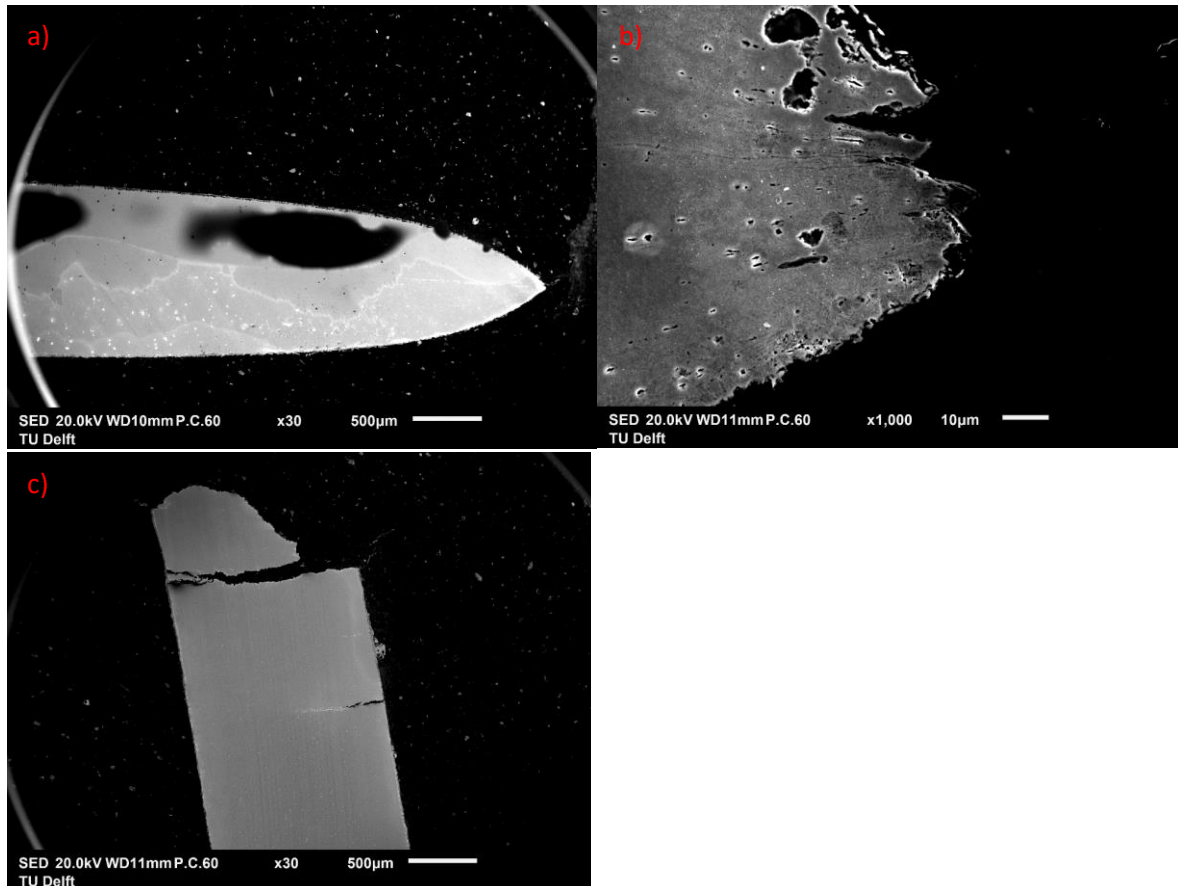
Figure 4.5: SEM micrographs of Gleeble hot tensile sample cross-sections at 850 °C, a strain rate of 0.13 s^{-1} and a hold time of 10s. a) uncoated samples, b) enlarged image of the fracture surface of an uncoated sample, c) coated sample.

EDS was performed on the coated sample, investigating the distribution of zinc on the surface of the sample and in features, such as cracks and the fracture surface. Figure 4.6 shows the EDS images on these samples. It can clearly be seen that zinc is present at crack surfaces and on the fracture surface.
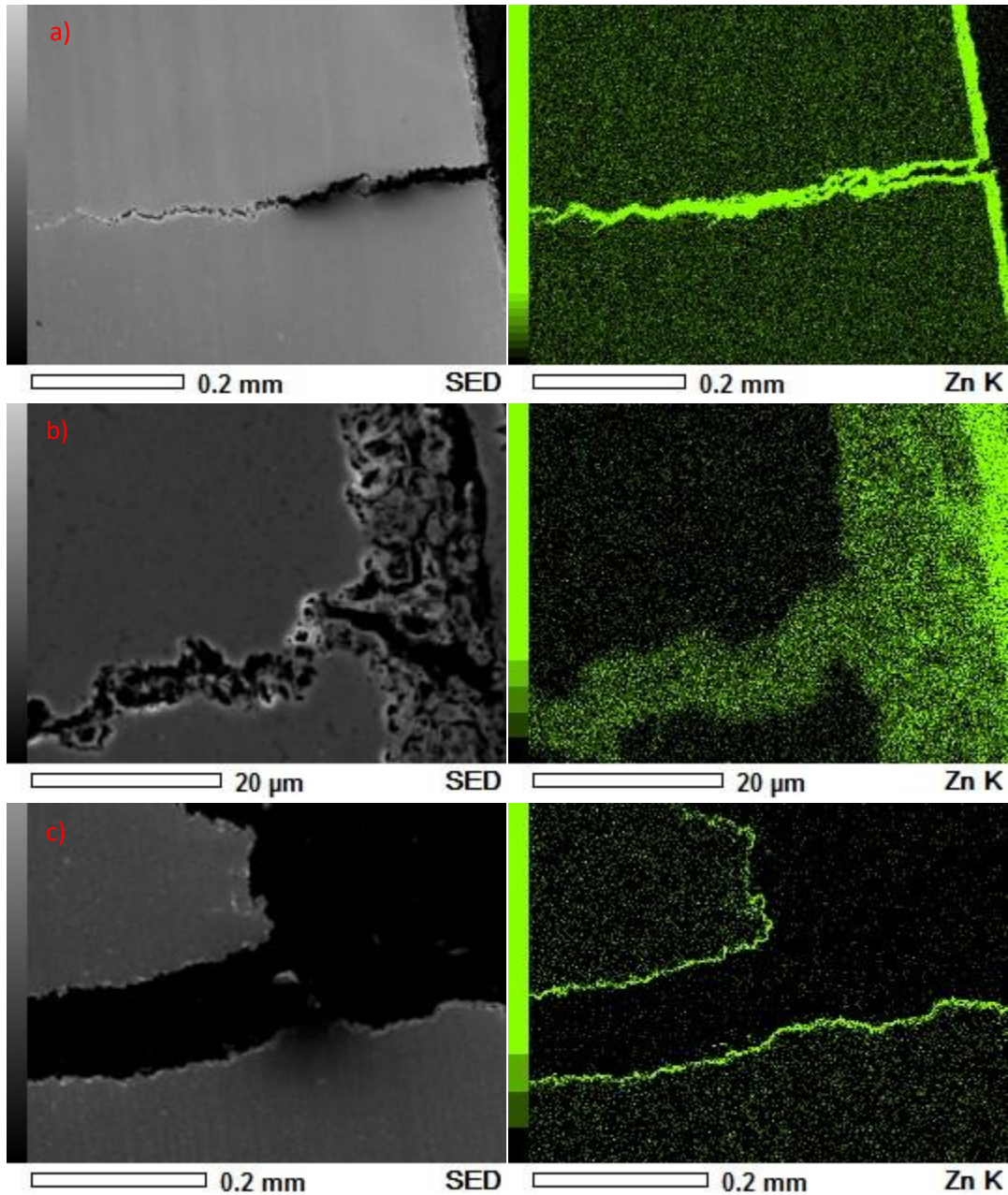
Figure 4.6: EDS of coated Gleeble hot tensile sample cross-sections at 850 °C, a strain rate of 0.13 s^{-1} and a hold time of 10, showing features and zinc presence. a) long crack in cross section, b) short crack in cross section, c) fracture surface.

A similar analysis was performed for higher (900 °C) and lower temperature (750 °C) Gleeble samples as shown in figure 4.7 and 4.8, respectively. In these figures, first, a global overview is shown, second, local EDS images are shown on zoomed in crack-like features and the fracture surface. Under these conditions, the samples show a combination of ductile failure (necking and plastic deformation of the sample) and brittle failure (the fracture surface). Additionally, some zinc penetration is seen into faults along the surface and into the fracture surface. However, the zinc penetrates to a significantly smaller degree: not the entire cracks surface is coated, but only partly at the edge of the crack and fracture surfaces.
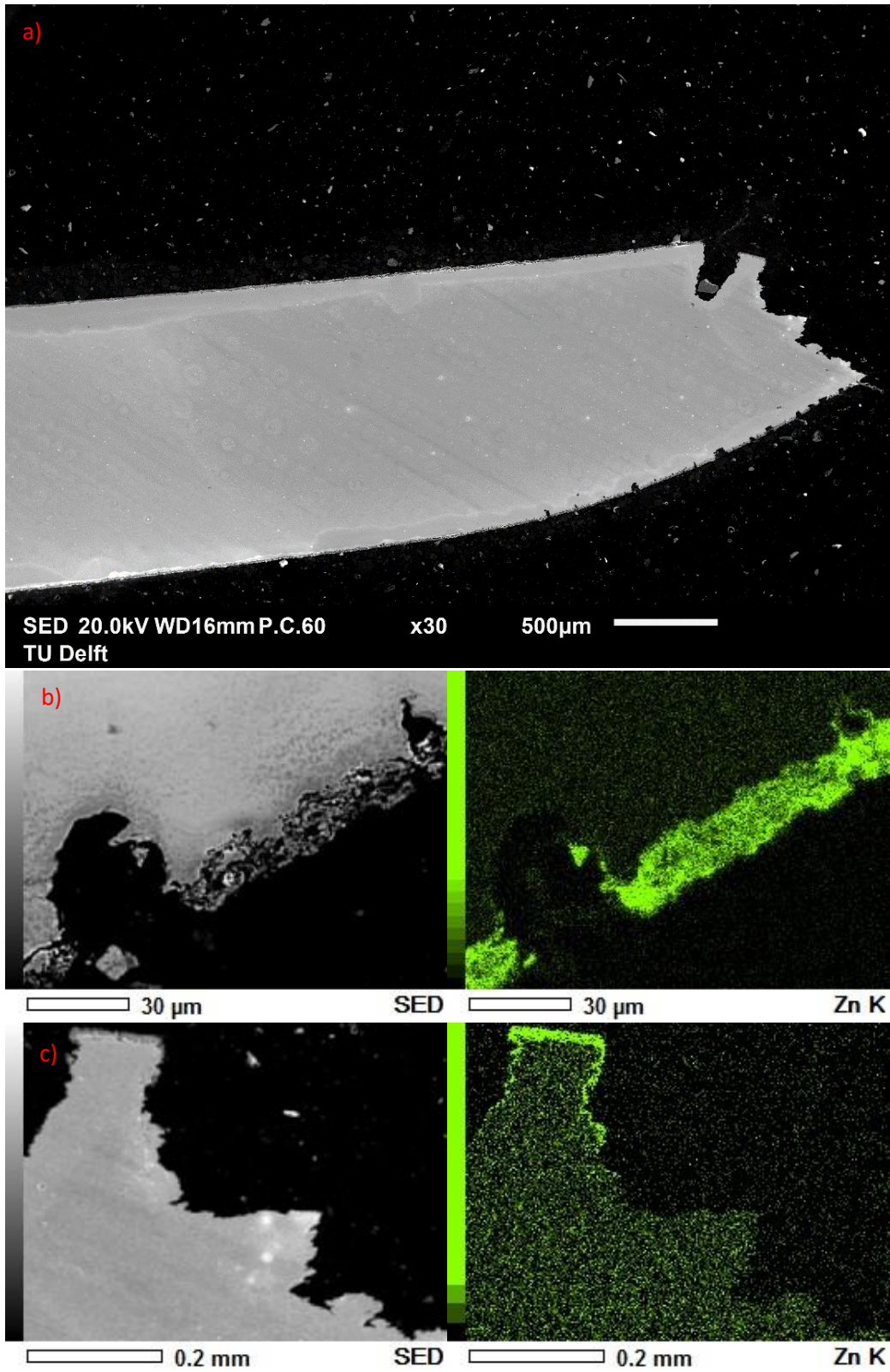
Figure 4.7: Macrograph and EDS showing zinc presence on surfaces enlarged images of features of coated Gleeble hot tensile sample cross-sections at 750 °C, a strain rate of 0.13 s^{-1} and a hold time of 10 s. a) global macrograph of cross section, b) EDS of blunted crack-like features showing zinc, c) EDS of fracture surface showing zinc.

a)

SED 20.0kV WD10mm P.C.60　　x30　　500μm
TU Delft

b)

30 μm　SED　30 μm　Zn K

c)

0.2 mm　SED　0.2 mm　Zn K
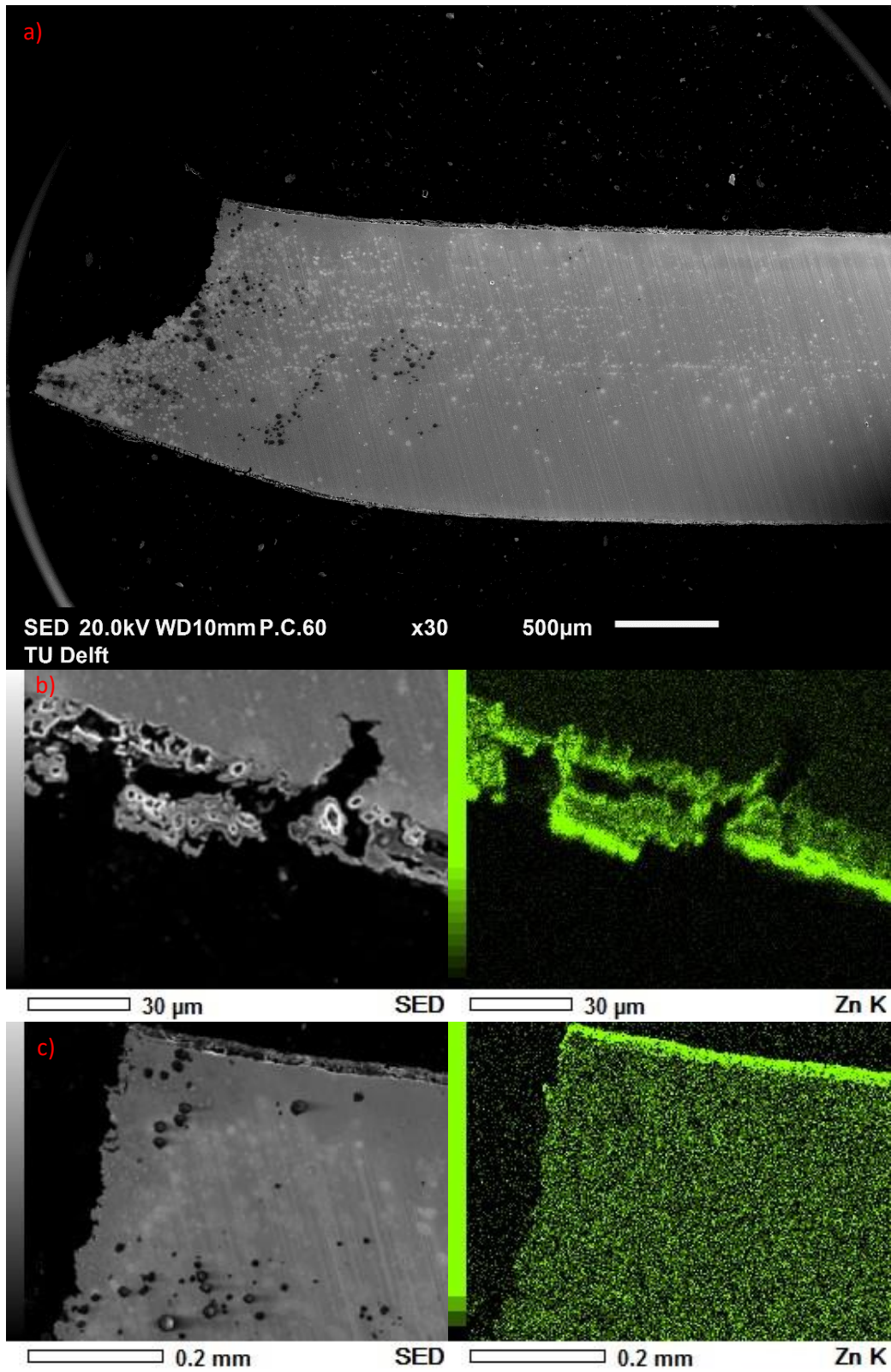
Figure 4.8: Macrograph and EDS showing zinc of coated Gleeble hot tensile sample cross-sections at 900 °C, a strain rate of 0.13 s^{-1} and a hold time of 10 s. a) global view macrograph, b) EDS of crack-like features showing zinc, c) EDS of fracture surface showing zinc.

Figures 4.9 and 4.10 show cross sections of samples for the two extremes of holding time: no hold time and a 1 min hold time. These images clearly show the effect of holding time. Figures 4.9 and 4.10 show SEM macrographs of no hold time and 1 min hold time, respectively. Figures 4.11 and 4.12 show EDS images of the same samples at different locations. These images show the large difference between no holding time and a 1 min holding time: negligible necking and plastic deformation, paired with clear brittle crack growth and fracture surface for a longer holding time. Extensive plastic deformation and necking paired with a clearly ductile fracture surface in the case of no holding time. Additionally, EDS images show that zinc covers the fracture surface and other crack surfaces and even penetrates beyond the crack tip in the case of no holding time, whereas 1 min holding time leads to no zinc penetration into the bulk; No penetration into cracks or faults along the surface can be seen and no zinc is found present on the fracture surface. The zinc coating for the longer holding time appears to have been changed significantly: gaps and cracks in the coating can be seen.
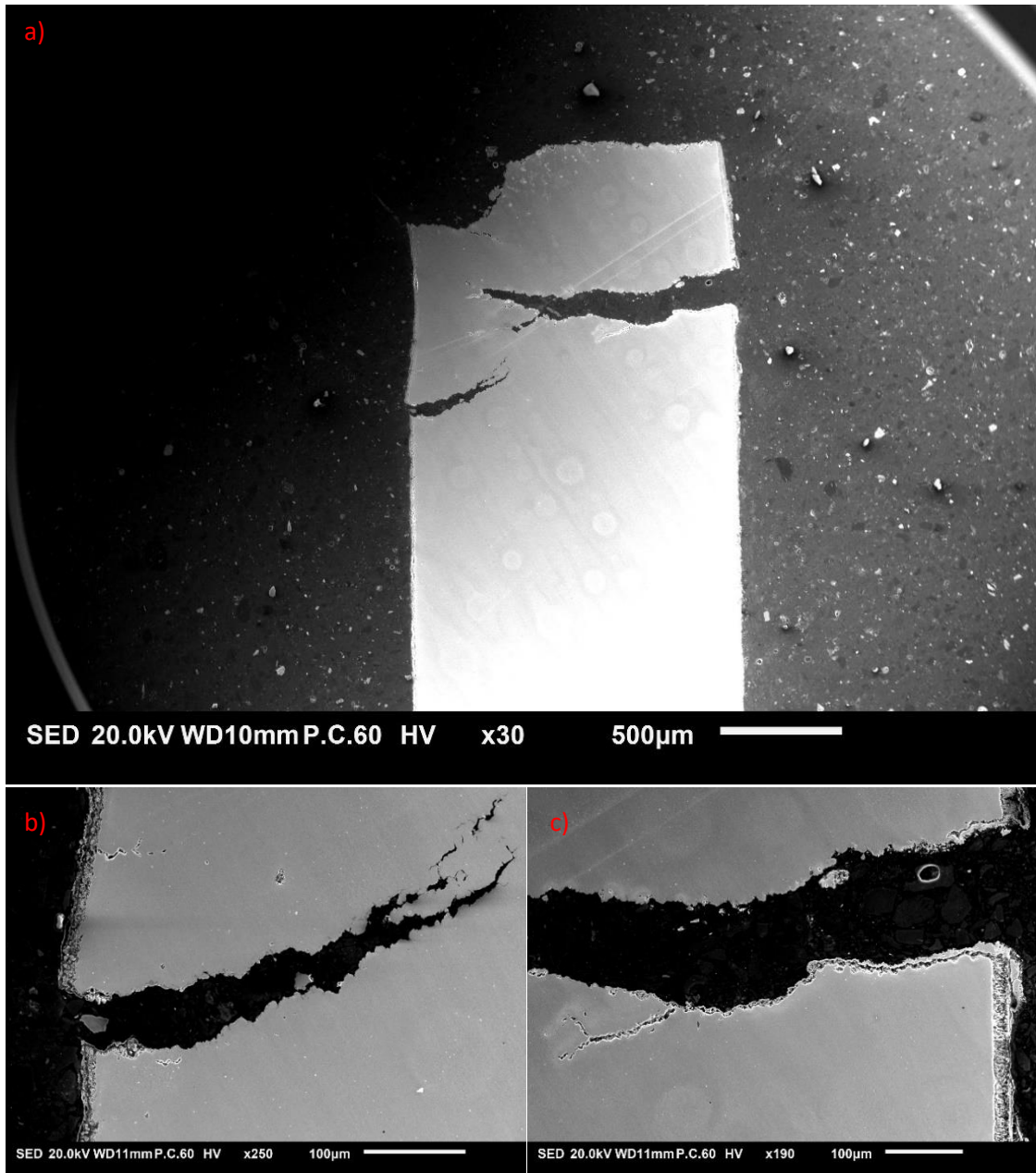
Figure 4.9: SEM macrograph of coated Gleeble hot tensile sample cross-sections at 850 °C, a strain rate of 0.13 s^{-1} and no hold time.
a) global view of the fracture surface, b) micrograph of left crack, c) opening of incomplete fracture, including zinc coating of crack surface and branching cracks.

SED 20.0kV WD10mm P.C.60 HV   x40   500µm

SED 20.0kV WD11mm P.C.60 HV   x200   100µm
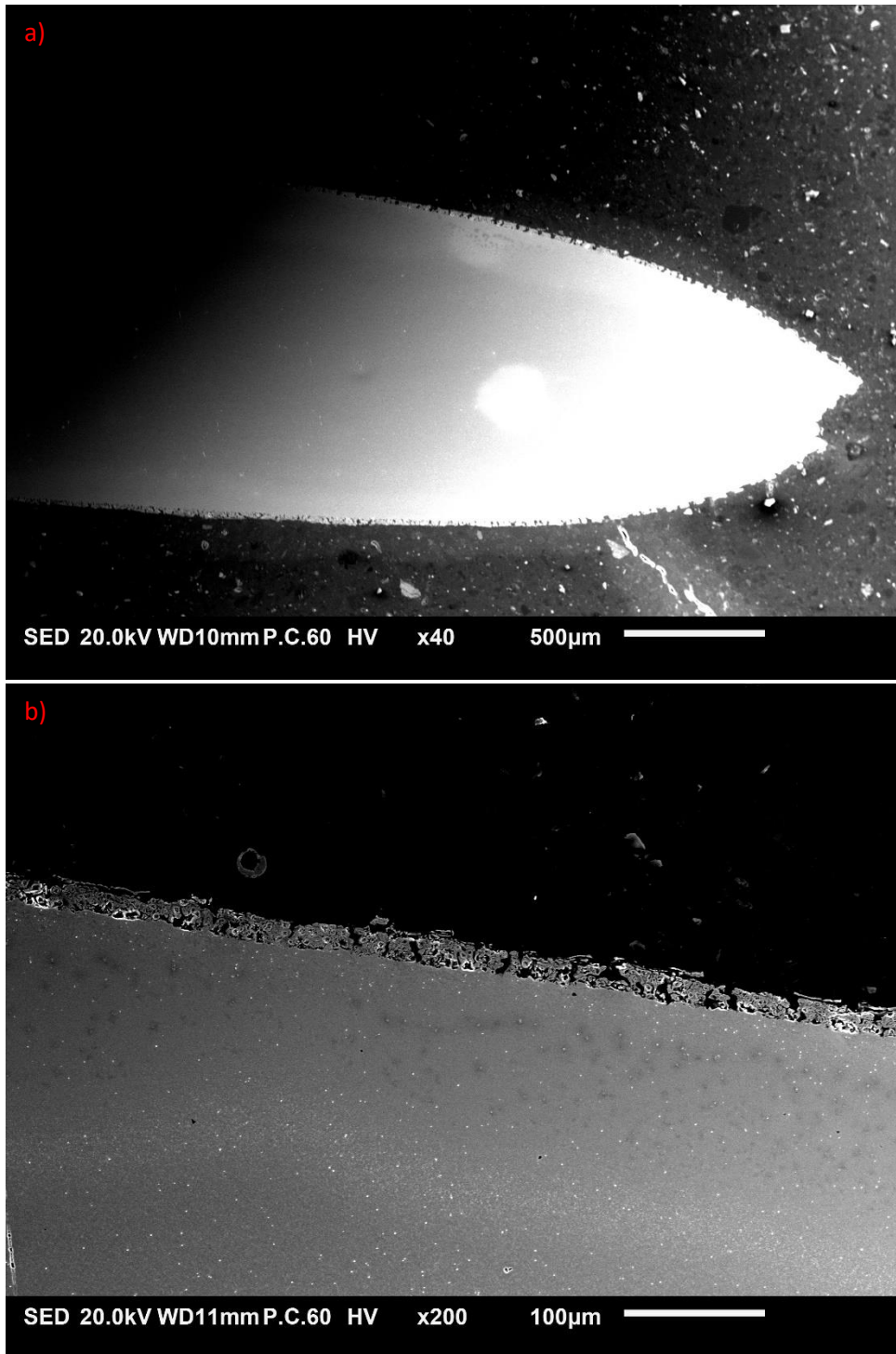
Figure 4.10: SEM micrograph of coated Gleeble hot tensile sample cross-sections at 850 °C, a strain rate of 0.13 s^{-1} and 1 min hold time. a) global view around fracture area, b) enlarged view of coating close to fracture area.
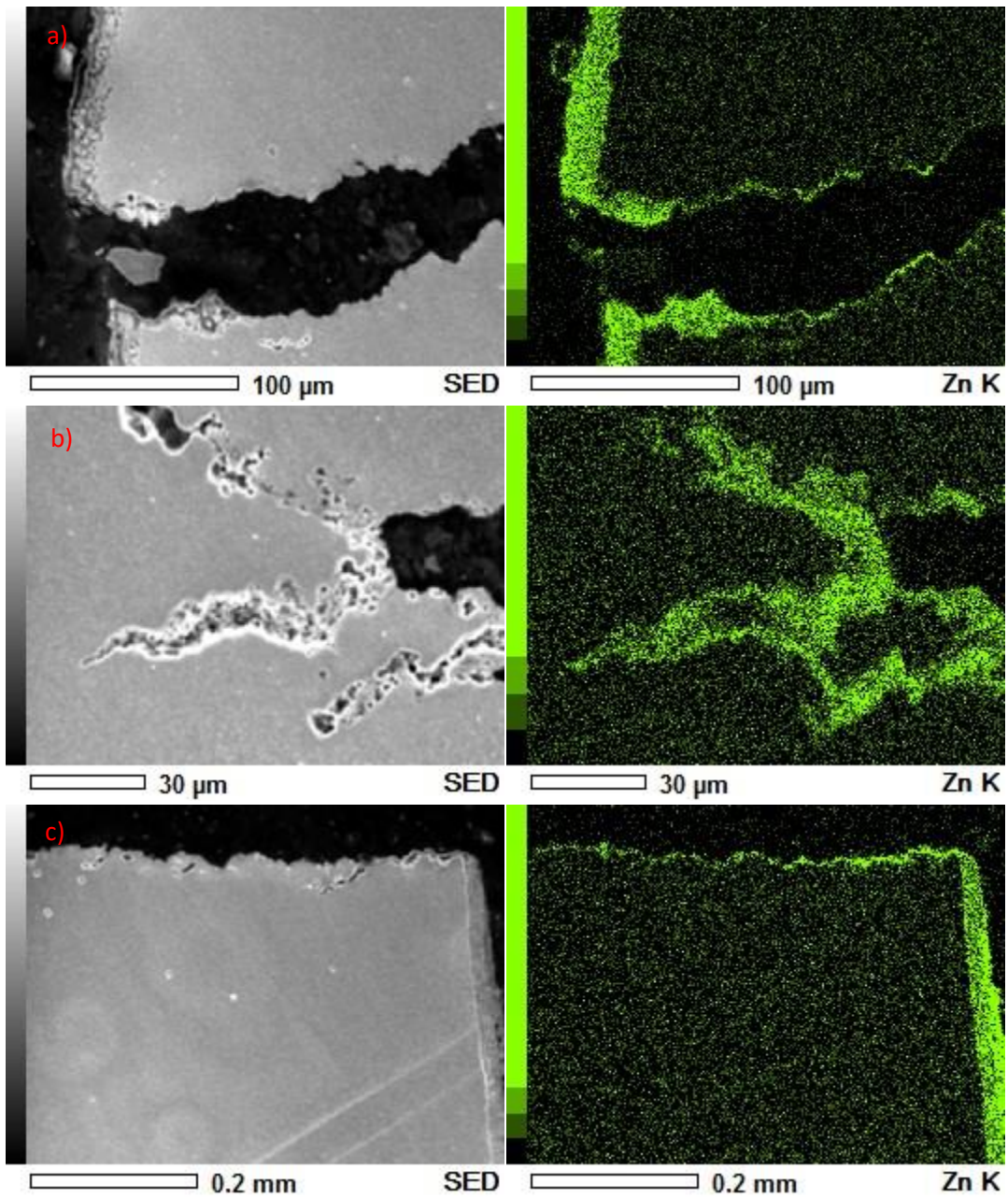
Figure 4.11: EDS analysis showing zinc presence in coated Gleeble hot tensile sample cross-sections at 850 °C, a strain rate of 0.13 s^{-1} and no hold time. a) the opening of a large crack, b) zinc penetration ahead of crack tip, c) fracture surface.
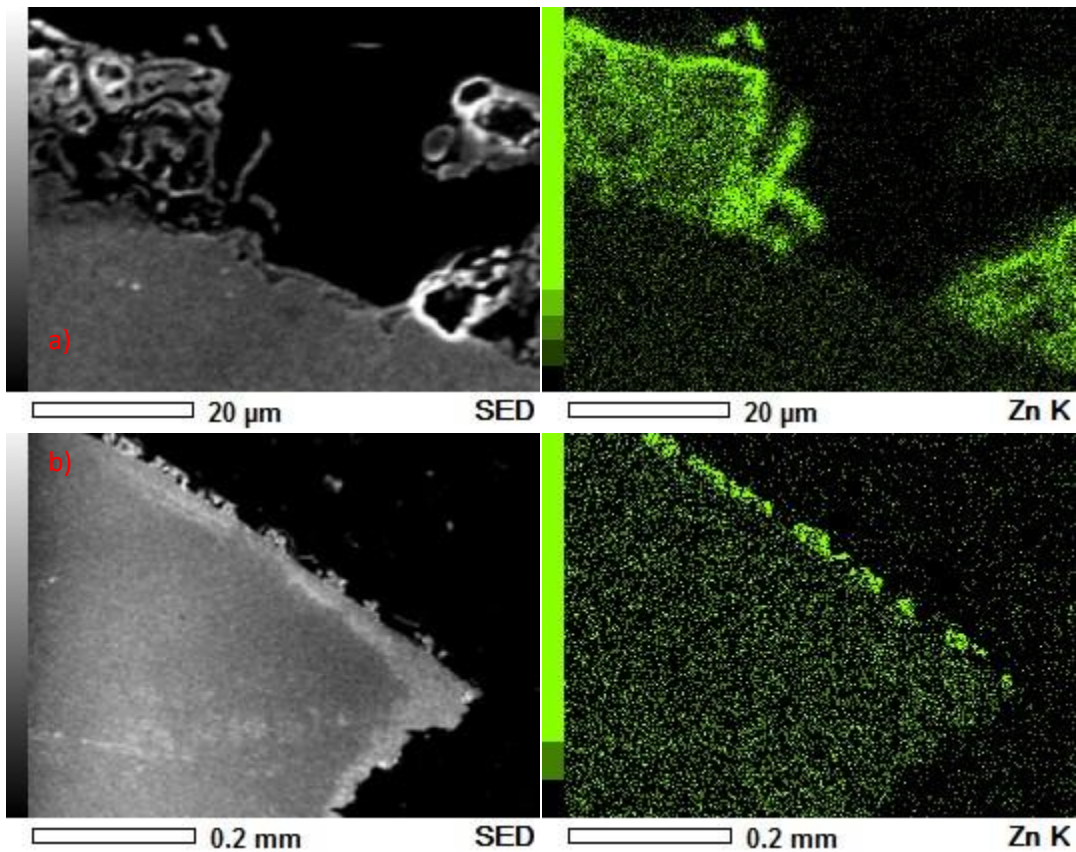
Figure 4.12: EDS analysis showing zinc presence in coated Gleeble hot tensile sample cross-sections at 850 °C, a strain rate of 0.13 s^{-1} and 1 min hold time. a) crack in coating and steel substrate underneath, b) fracture surface.

Finally, SEM micrographs of etched samples at low and high strain rate (1.3*10^{-3} s^{-1} and 1.3 s^{-1}) were obtained to characterise the microstructure around the cracks, fracture area and bulk. Figures 4.13 and 4.14 show etched microstructure of 1.3 s^{-1} samples in the bulk and around features, respectively. Red circles in these figures show microstructural features that will be further discussed in chapter 5. Figure 4.15 shows the etched microstructure of 1.3*10^{-3} s^{-1} samples around the fracture surface and the coating. These images show a clear gradient in the microstructure (figure 4.14 b) and a difference in microstructure between the homogeneous temperature zones and further from these zones (figures 4.13 and 4.14 respectively.) Further a difference in ductile and
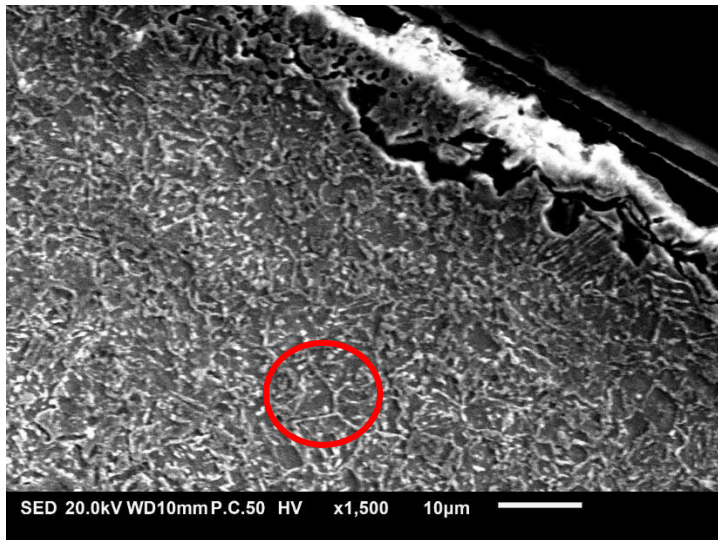
Figure 4.13: SEM micrograph of an etched coated Gleeble hot tensile sample cross-section at 850 °C, a strain rate of 1.3 s^{-1} and 10 s hold time. Image taken several cm away from homogeneous temperature zone and cracked area.
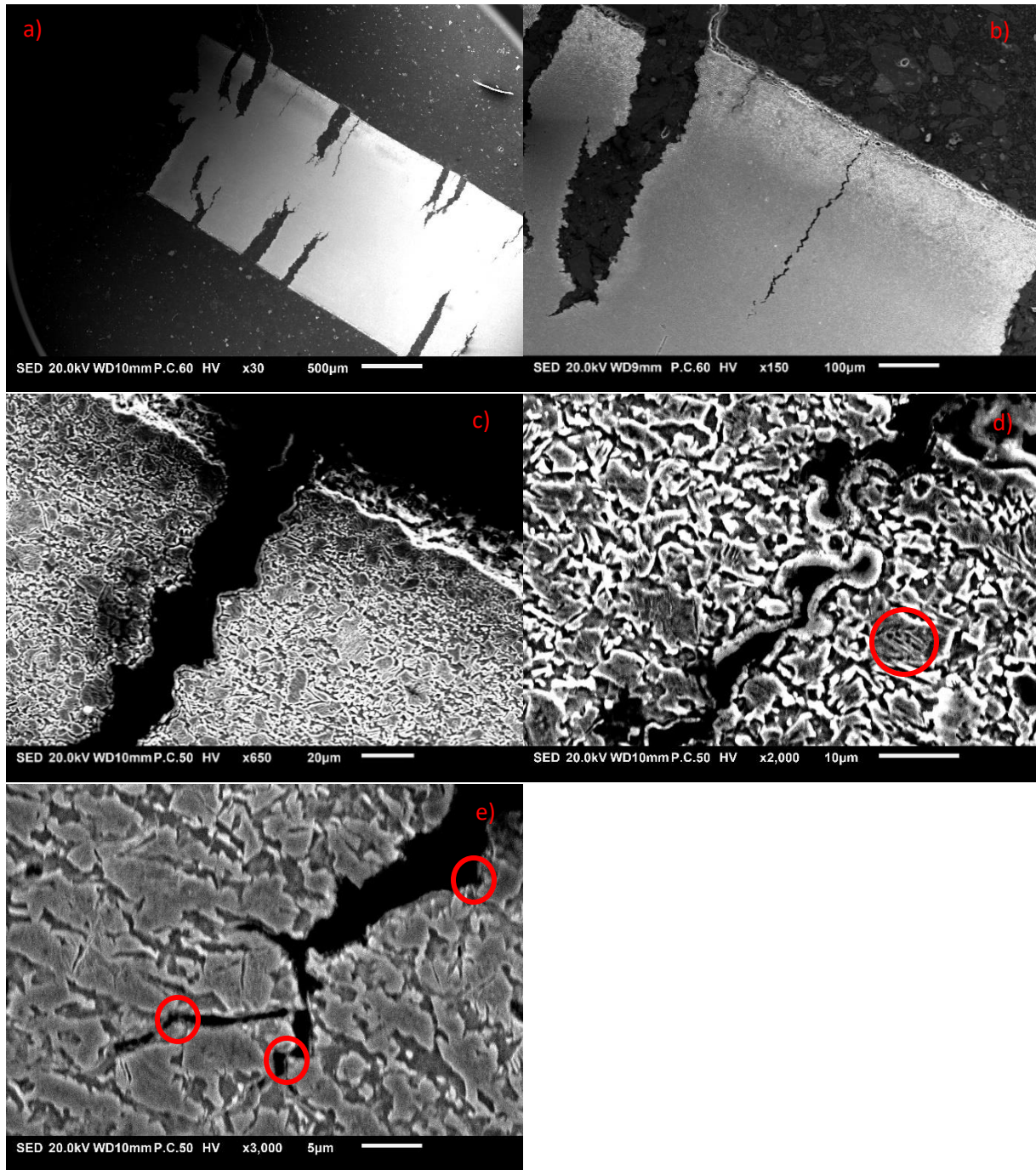
Figure 4.14: SEM micrographs of an etched coated Gleeble hot tensile sample cross-section at 850 °C, a strain rate of 1.3 s^{-1} and 10 s hold time. a) global overview, b) microstructure gradient from surface to bulk, c) microstructure around crack opening, d) microstructure around thin crack, e) microstructure around crack tip. Marked red circles show microstructural features discussed in chapter 5.
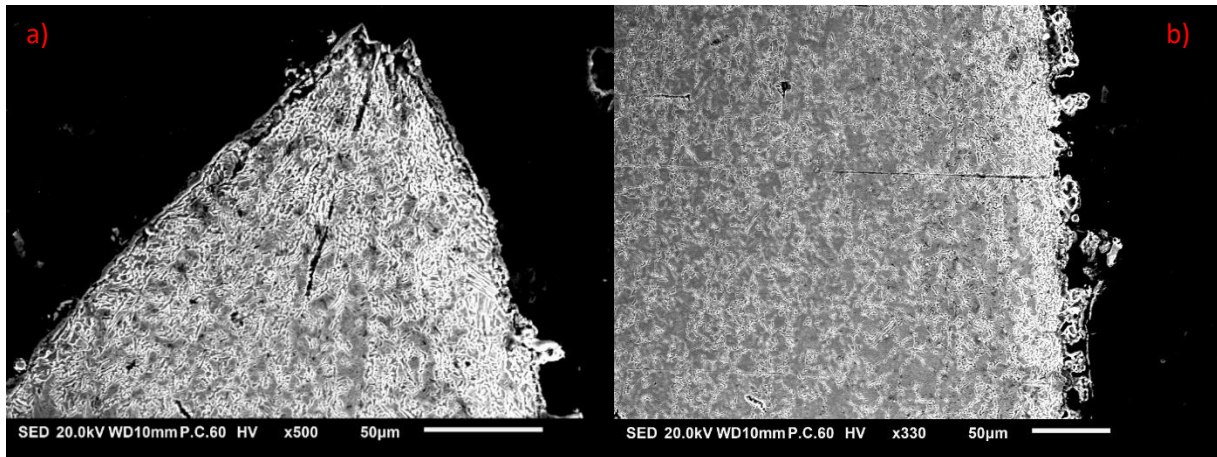
Figure 4.15: SEM micrographs of an etched coated Gleeble hot tensile sample cross-section at 850 °C, a strain rate of $1.3 * 10^{-3}$ and 10 s hold time. a) microstructure around fracture surface, b) microstructure around zinc coating sever cm away from fracture area.

4.2 LBW results

4.2.1 Quantitative

Different experimental parameters were measured during LBW with a pre-loaded specimen as outlined in section 3.3. For relatively high loads (80-100 % of the yield strength), the effect of different welding conditions on the stress development during welding was investigated. Welding was completed within 2 s, but loads were measured for a longer period to also include recovery. Additionally, an experiment with a linear weld instead of a spot weld was performed, as it produces a larger weld and was therefore expected to produce a larger area that would be susceptible to LME so also. The linear weld was performed at 1 kW laser power, with a weld speed of 10 mm/s over the entire gauge length. Load was translated to stress. Results for a range of conditions are shown in figure 4.16. It can be seen that, when welding starts (the first few steps in the curves), the load drops significantly. When welding ends (the minima of the curves), the stress is recovered slightly. The absolute amount of stress recovery appears to be constant for the spot welds, whereas the linear weld achieves a greater degree of recovery.
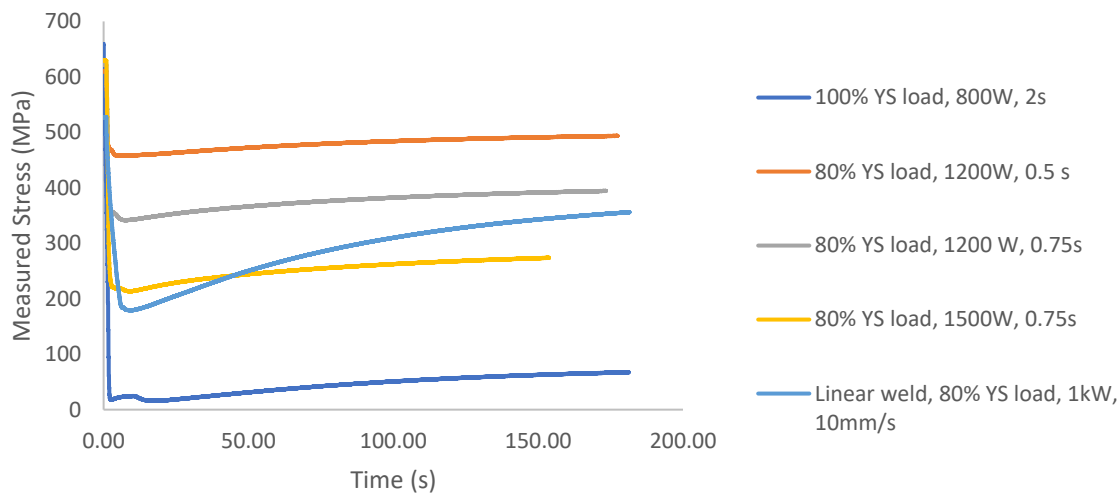
Figure 4.16: Stress development during welding for single samples, loaded and welded at different welding conditions.

Additionally, the temperature evolution in the HAZ during and after welding was monitored as outlined in section 3.3. Lower laser powers and longer times were used to approximate total energy inputs of other samples. The results are shown in figure 4.17. As can be seen, the temperature increases quickly during the first part of welding. In all cases, the slope of the temperature increase decreases. A maximum is then reached when the welding stops, and cooling begins. In the case of the highest laser power (300 W for 10 s and the lower power for a long time (240 W for 20 s), the temperature increases further. The decrease in slope of temperature increase is recovered at around 400 °C. The temperature then increases significantly, until just before cooling, the measured temperature fluctuates significantly.
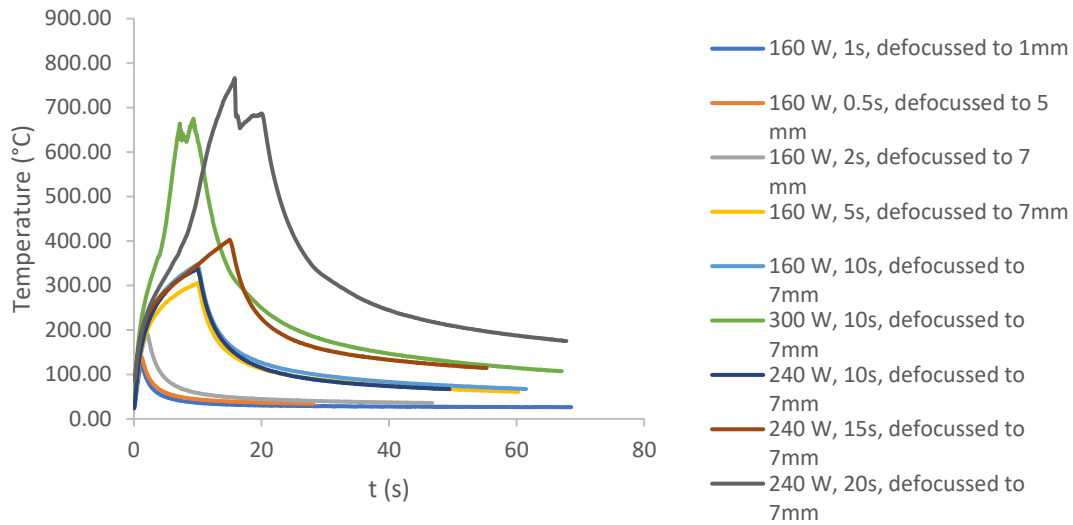
Figure 4.17: Temperature development ~1 cm from the fusion line of spot welds using different laser power setups.

4.2.2 Characterisation

The surfaces of the LBW samples were first investigated visually to find locations containing features resembling cracks. Due to the localised nature of LBW's, cross-sectioning would otherwise be too inconsistent. Surfaces of LBW showing crack-like features are shown in figures 4.18 through 4.21. Optical micrographs of other samples are collectively shown in appendix C. Indications of cracks can be found around the fusion zone in the HAZ. These features have been marked using red arrows and circles. In the melt pool, crack like features are also seen, related to hot cracking (figures 4.19 and 4.21)
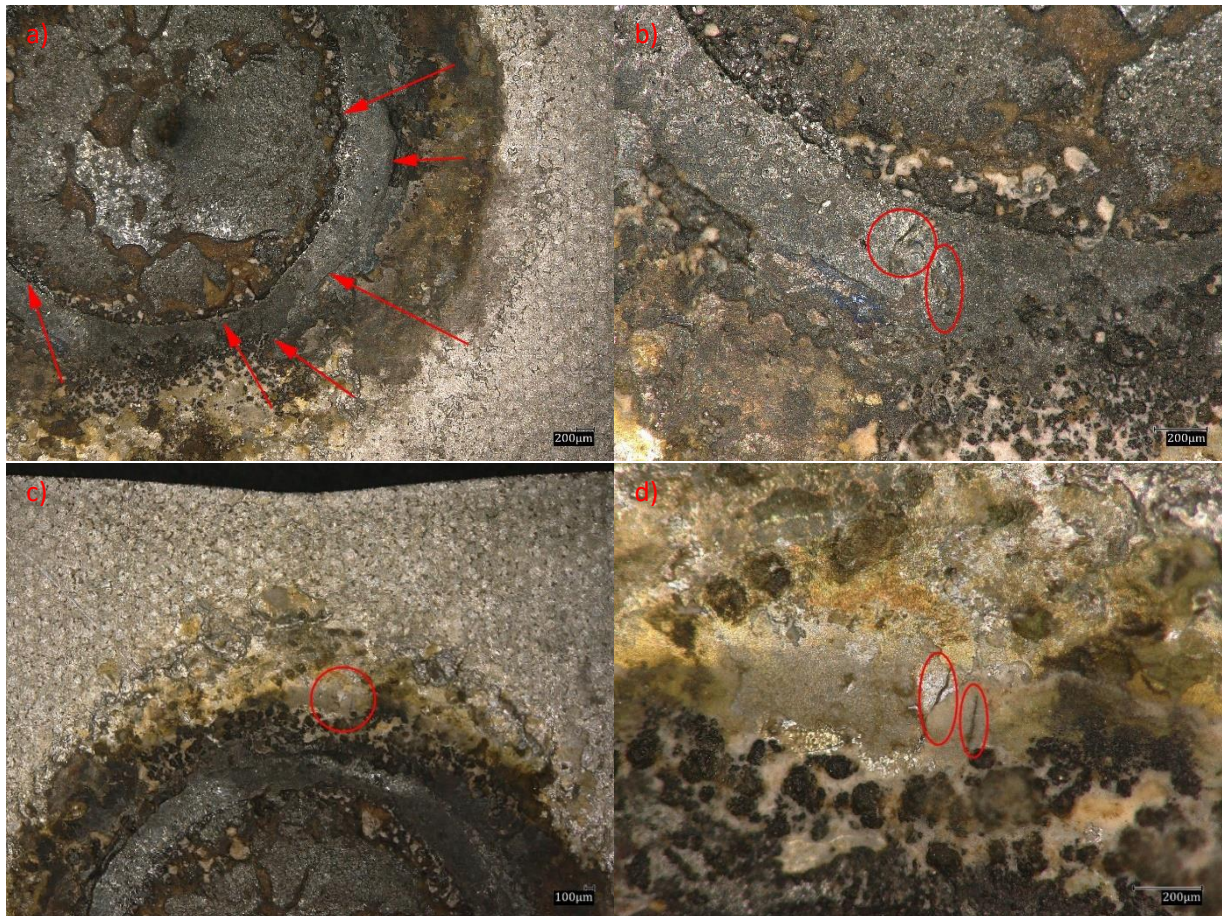
Figure 4.18: Optical micrographs of an LBW sample, loaded to 100% of yield strength, loading direction left to right, welded using 800W beam power defocussed to 1 mm for 2 s. a) marked circumferential features around fusion zone. b) transverse features marked in HAZ, c) transverse features location marked above HAZ, d) enlarged view of marked features in c).
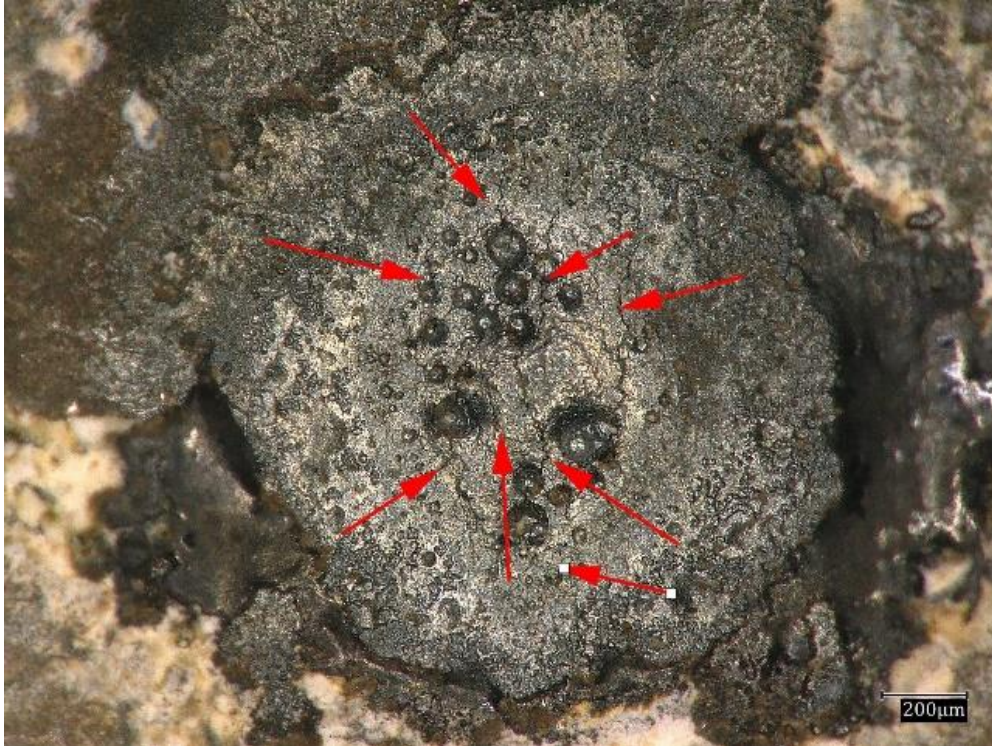
Figure 4.19: Optical micrograph of an LBW sample, loaded to 100% of yield strength, loading direction left to right, welded using 200W beam power defocussed to 2 mm for 10 s, with transverse features marked.
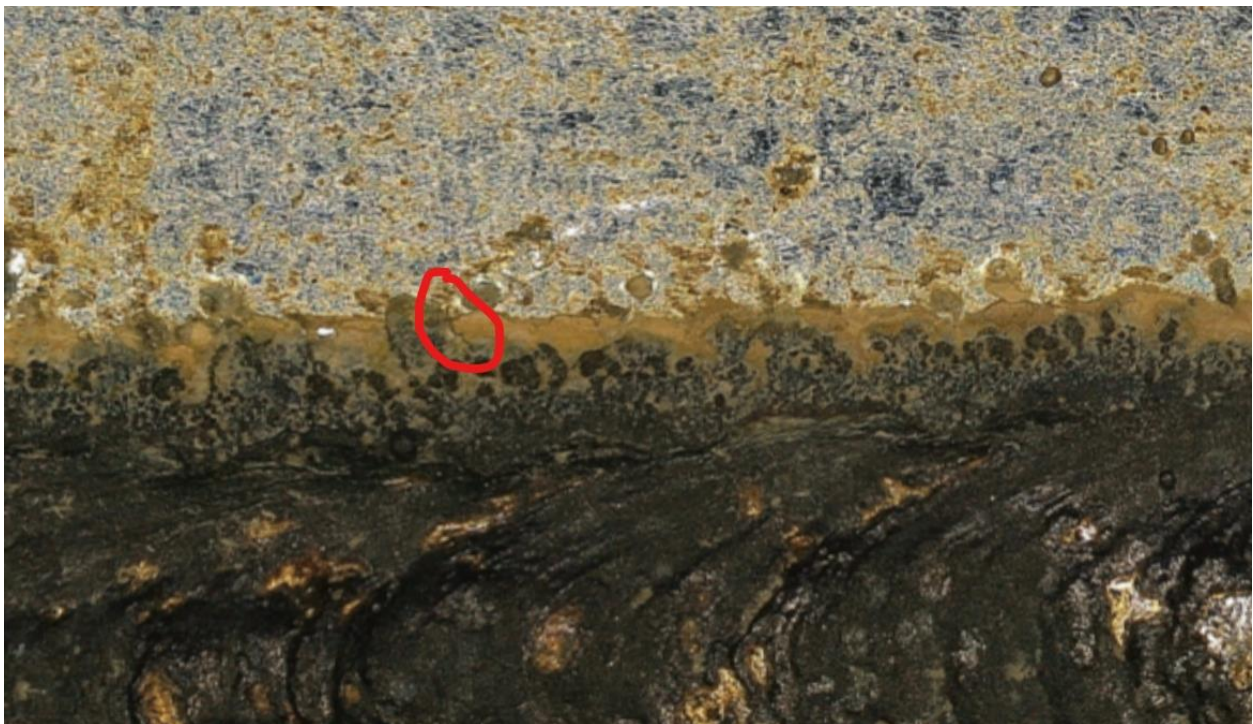
Figure 4.20: Optical micrograph of an LBW sample, loaded to 80% of yield strength, linear welded using 1 kW laser power at a velocity of 10 mm/s not defocussed parallel to loading direction. Crack-like feature marked.

Figure 4.21: Optical micrograph of an LBW dog-bone sample, loaded to 80% of yield strength, loading direction left to right, welded using 800W beam power defocussed to 1 mm for 2 s, with circumferential features marked.

Location of features were marked and cross sections through these features were made to identify feature type and depth. One such cross section is shown in figure 4.22. Additional SEM micrographs are shown in appendix D. With cross sections through these features, no evidence of crack-like features can be found in the SEM images. No EDS analyses of zinc in crack like features can therefore be shown.
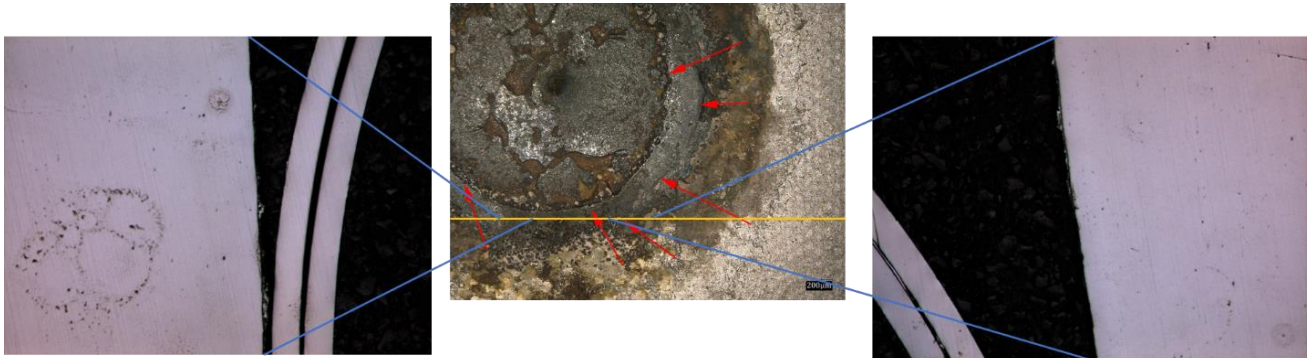
Figure 4.22: SEM micrographs of cross section through crack-like features on top side of LBW weld.

Finally, cross sections of two samples welded while stacked were made to investigate the interface. Due to the interface being under investigation, no surface micrographs were made. Figure 4.23 shows SEM optical micrograph of the interface around the weld. Figure 4.24 shows EDS analyses of both the interface and the top and bottom surfaces.
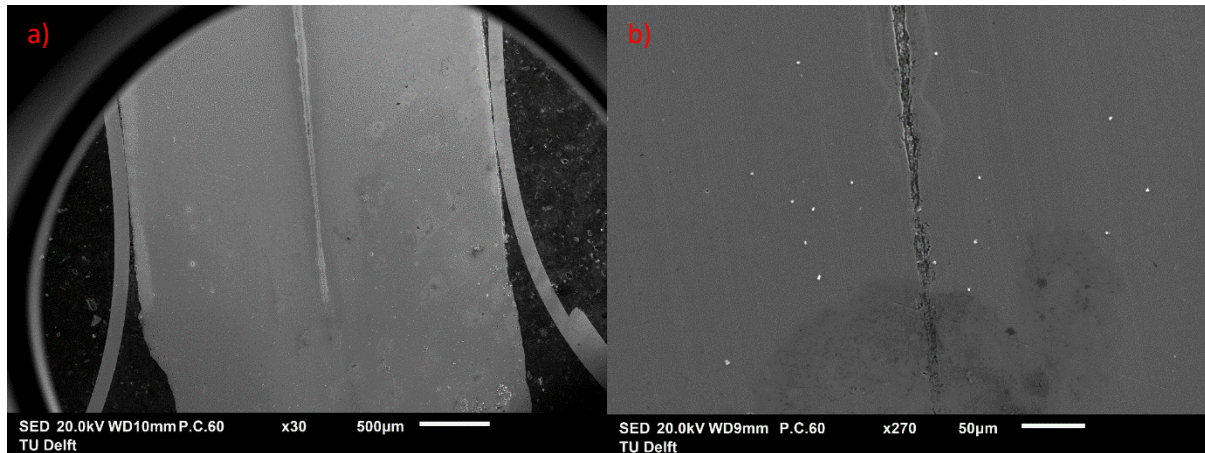
Figure 4.23: SEM micrographs of cross sections transverse to the loading direction of two samples laser beam welded and loaded to 100% of yield strength, using a focussed beam power of 2 kW for 1s. a) wide view of weld zone interface, b) enlarged image of weld interface just above fusion zone.
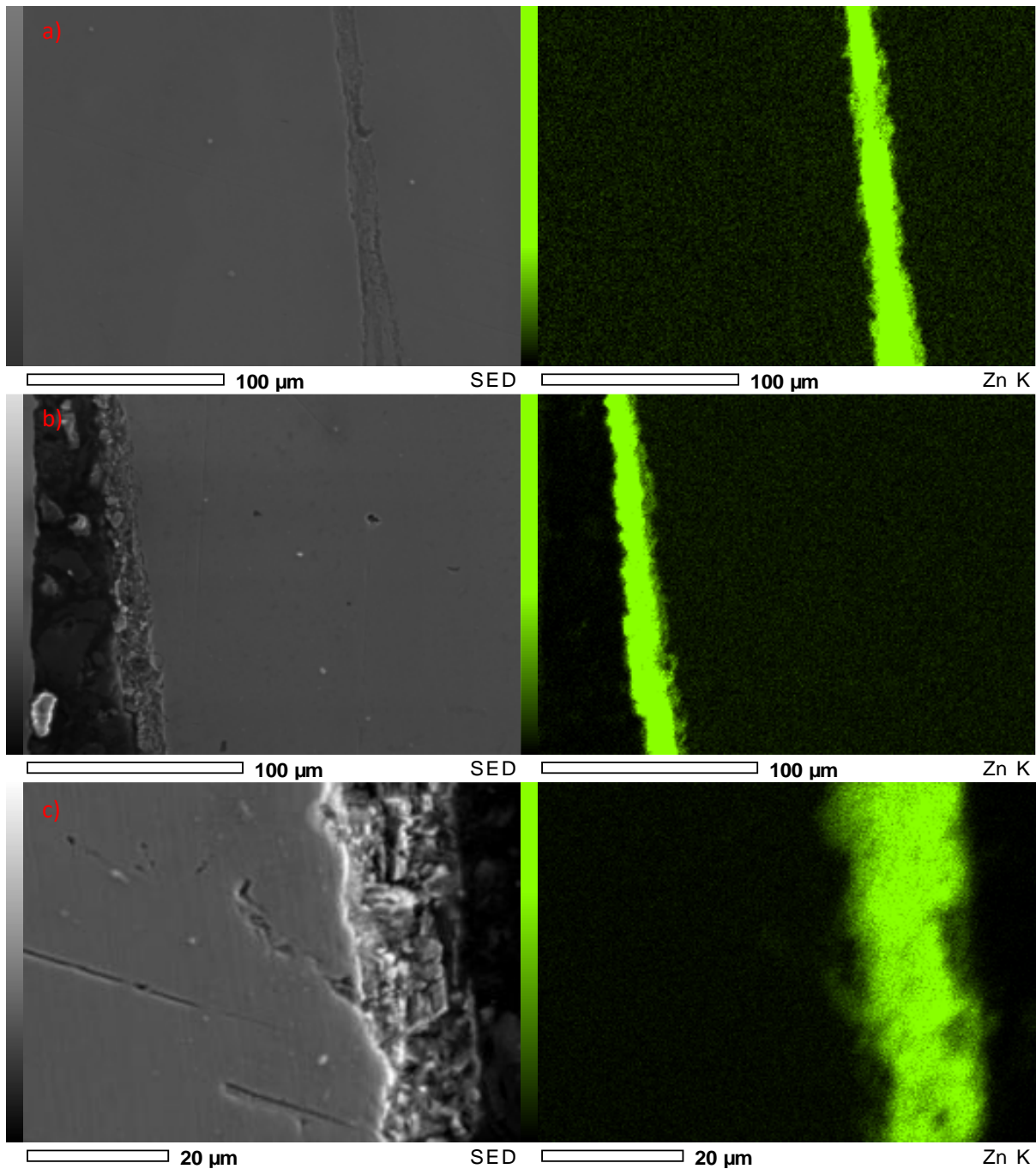
Figure 4.24: EDS analysis, showing zinc, of cross sections transverse to the loading direction of two samples laser beam welded loaded to 100% of yield strength, using a focussed beam power of 2 kW for 1s. a) interface just above weld, b) top surface just above weld, c) bottom surface just above weld.

5. Discussion

In this section, the results shown in the previous section will be discussed. Explanations for findings will be given, along with assumptions made. Incomplete knowledge and uncertainties will be addressed, and future recommendations are given. First, the three investigated parameters in Gleeble hot tensile testing are addressed: temperature effect, strain rate effect and holding time effect. Afterwards, LBW results are explored. Next, COMSOL simulations are used to relate the findings from Gleeble testing with the results from LBW testing. Finally, some initial points regarding the connection to RSW are made. In this chapter, bulk diffusion will be referred to as simply diffusion. Grain-boundary diffusion and penetration will both be referred to as penetration.

5.1 LME in Gleeble testing

This section will discuss the findings from Gleeble hot tensile testing. The quantitative and qualitative results will be combined to explore the effect of temperature, strain rate and holding time on the occurrence and extent of LME.

5.1.1 Temperature

The stress-strain curves from figure 4.1 show that for all temperatures, the elastic part does not significantly deviate between bare and coated samples. As temperature increases from 600 to 850°C, the curves start to deviate at an earlier stage of the plastic regime at higher temperatures. When the cross section decreases due to necking, the coated samples suddenly fails earlier than the bare sample. When increasing the temperature past 850°C, the ultimate strain is gradually recovered.
This effect is illustrated in terms of relative fracture energy of the coated sample as compared to the bare sample in figure 4.2. At the lower temperatures (600-750°C) there is only a small reduction in fracture energy of 20-30%. After 750°C, the fracture energy of the coated sample suddenly drops significantly, dropping as low as 20-30% of the fracture energy of the bare energy between 800 and 825°C. Above this temperature, the fracture energy gradually increases until it reaches the same relative value as the lower temperatures just above 900°C. This so-called ductility trough is similar to results found in previous literature shown in chapter 2.5 [39]. By combining the lower maximum strain with a similar UTS as seen in the stress-strain curves with the reduction of fracture energy, the ductility trough is clearly a result of a reduction of the ductility of the sample (embrittlement) as opposed to a general weakening of the sample. Additionally, the fact that the embrittlement occurs so extensively in the coated sample gives a first indication that it is in fact liquid zinc embrittlement.

At low temperatures (600 °C) the zinc is present in liquid form. However, penetration of zinc is not observed, and embrittlement does not take place, even though the stress level increases. Apparently, at this temperature the phases present (ferrite and martensite) are not susceptible to penetration of zinc. The lower limit of the embrittlement trough, is somewhere between 700 and 750°C. When tests are carried out at temperature above 750°C a significant reduction in relative toughness is encountered. It appears that LME occurrence is partially tied to austenitic phases in the steel, as, in the steel studied the austenite start temperature is around 727°C, as can be seen from the Fe-C phase diagram as shown in

figure 5.1. Because of the addition of Mn to the steel, the actual austenite start temperature can be assumed to be slightly lower, as Mn is an austenite stabiliser [45]. The sudden increase in embrittlement when the steel becomes austenitic can be explained through the grain boundary energy. As discussed in chapter 2.1, LME has a high dependence on the grain boundary energy, because the liquid metal penetrates the grain boundaries, creates two new interfaces, and separates the grains. If the grain boundary energy is low enough, creation of new interfaces is not preferable, and LME will not occur. Although exact grain-boundary energies cannot be stated, due to conditions, such as misalignment angle, alloying elements and strain energies all playing a role on the interfacial energies, approximations can give some insight. On average, the grain boundary energy of ferrite-austenite is higher (~0.80 J/m^2 [46]) than the grain boundary energy of ferrite-ferrite (~0.60 J m^{-2} as shown in figure 5.2 [47]). The formation of austenite in these temperatures can be identified from the etched microstructural features marked by red circles shown in figure 4.13 and less clearly in figure 4.14. The appearance of allotriomorphic ferrite indicates prior austenite grain boundaries.

The upper limit of embrittlement is just above 900°C. Figure 4.2 indicates that at this temperature the relative toughness has recovered to the level found at 600 °C. The fact that much of the ductility is recovered is another indication that the embrittlement is caused by liquid zinc. The boiling point of zinc is 907°C [41]. Above this temperature, the liquid zinc will evaporate before the load is applied. When the load is applied, no more zinc remains to cause LME and the fully austenitic microstructure is just tested at high temperature. As can be seen in Figure 5.2, the average grain boundary energies of f.c.c. elemental metals are around 0.40 J/m^2 [47], lower than the ferrite-ferrite grain boundary energy stated before. Therefore, if the microstructure is indeed fully austenitic at the higher temperatures, this would also aid in the recovery of fracture toughness. As the microstructure becomes more austenitic, more grain boundaries will have a lower energy and therefore, following the governing interfacial energy equation (equation 2.1), become less susceptible to LME.
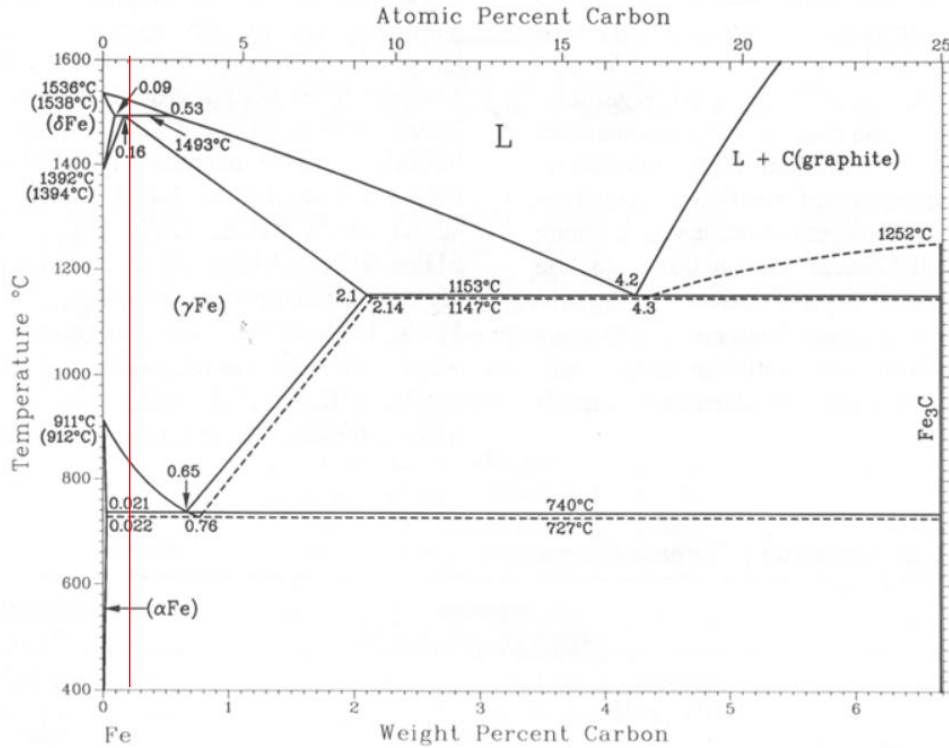
Figure 5.1: Fe-C phase diagram, with the carbon content of the steel studied marked with a red vertical line. Solid lines are recommended by Okamoto [48], dotted lines are recommended by Massalski [49].

Figure 5.2:

Average grain boundary energies of elemental metals, including their crystal structure, as determined through DFT calculations [47]

Finally, below the lower limit and above the upper limit, there is still a significant reduction of the fracture energy of approximately 20%. This can be explained by looking at the solid-liquid interfacial energies of liquid zinc on iron. By combining the findings of two papers [50] [51], an estimation can be made about the solid-liquid interfacial energy of zinc on iron. The interfacial energy of liquid Zn-Al on iron was determined to be 0.245 J/m^2 at 480 °C by Giorgi [50]. Erol investigated the liquid-solid interfacial energies of different Zn-metal liquids on zinc. Their results indicate that adding different metals to the liquid zinc has only a slight influence on the measured interfacial energy (a variation of around 0.01 J/m^2) [52]. Therefore, the presence of Al in the liquid zinc in the paper by Giorgi is neglected and the value for interfacial energy assumed to be similar for liquid zinc on iron. Additionally, the temperature dependence of the interfacial energy is unknown, but seems to increase slightly for increasing energy [53]. So, the estimated interfacial energy of two created liquid zinc-solid iron interfaces is estimated to be ~0.490 J/m^2. At the lower tested temperatures (600-700 °C), mostly bcc iron will be present in the steel. This value is lower than the estimated average grain boundary energy of 0.6 J/m^2 for bcc iron. Since the grain boundary energy is an average, grains with higher misorientation angles will most likely have a higher energy, while grains with a lower misorientation angle will have a lower energy. Combined with the rough estimation of the interfacial energy, this means that, at the lower temperature ranges, some grain boundaries will fulfil the governing energy equation (equation 2.1), while others do not. A part of the material will therefore be susceptible to LME, leading to a slight decrease in fracture energy.

For the upper temperature limit, where more austenite would have formed, the estimated interfacial energy of 0.490 J/m^2 is significantly lower than the estimated f.c.c.-f.c.c. grain boundary energy of 0.8 J/m^2. It would therefore be expected that fully austenitic iron is not susceptible to LME at all. However, even though figure 5.1 shows that the equilibrium composition of the steel is fully austenitic at 900 °C, the short holding time of 10 s suggests that the equilibrium will not have been established yet. Similar to the case for the lower temperature limit, some grain boundaries will still be ferrite-austenite and susceptible to LME, while most grain boundaries are austenite-austenite and not susceptible. This combined with the evaporation and oxidation of zinc, results in a slight decrease in fracture toughness.

During experimentation, it was confirmed visually that, during necking caused by the displacement in the more ductile specimens, the edges of the sample heated up significantly just before failure. This is assumed to be a result of the ductile sample failing from the middle outward, resulting in the edges being connected with a progressively smaller cross section. This results in high temperature spikes through joule heating when the crack grows beyond the area measured by the thermocouples, producing an inability of the Gleeble to properly control the temperature. These temperature spikes for the lower temperature specimens potentially increase the temperature at the edges to be in the ductility trough, causing additional embrittlement.

The SEM macrographs showing the global view of the specimen in figures 4.5, 4.7 and 4.8 indicate the clear differences in ductility of the samples at the different temperatures. For the uncoated specimen at 850°C, an extensive reduction of cross-section around the fracture can be seen, tapering off to a point a few tens of microns wide. Additionally, many small and larger voids can be identified next to the fracture. All features clearly indicate ductile failure. The coated sample at the same temperature, however, shows no signs of ductile fracture, *i.e.,* there is no significant reduction of the cross-section, irregularly shaped cracks can be identified, and the fracture edge has a complete brittle appearance. At the lower (750°C) and upper temperature limit (900°C) the features of both ductile and brittle fracture can be seen. The

cross section has decreased slightly, plastic deformation can be easily identified due to the deformed shape and some voids can be identified. However, blunted crack-like features can also be identified, and certain parts of the fracture do not show evidence of being accompanied by a reduction in cross section of the sample.

EDS analyses of the coated sample reveal further indications of LME and the extent of embrittlement caused by liquid zinc. Most notably, the sample tested at 850°C shows that the cracks identified are entirely decorated with zinc, indicating extensive liquid penetration. Apparently, in the short time available during testing this process takes place. Both the presence of zinc in the cracks and on the fracture, surface strongly indicate the occurrence of liquid zinc embrittlement.

In the lower and higher temperature specimens in figure 4.7 and 4.8, however, still small crack-like features could be identified. Some zinc could be found to penetrate the features in these cases. However, the zinc does not fully coat the surface of the features. For the 750°C sample it is assumed that the zinc penetrates the grain boundaries at the surface slightly, forming a small crack. Further penetration into the grain boundaries at the crack tip seems not to occur. At this point, the crack blunts, and further failure happens more ductile. Due to the small cracks, the cross section will be slightly smaller, leading to a small reduction in the fracture energy. Further investigation of the exact mechanism of liquid zinc embrittlement of steel should be performed to confirm this assumption. For example, the Gleeble experiments could be performed with identical parameters, but halted at different times, ensuring that the samples have not failed yet. This way, the penetration of zinc can be monitored during the different stages of sample failure. Identification of the early stages of zinc penetration into the steel at the lower temperature limit without fully failing the material could provide insight into the mechanism. Additionally, EBSD measurements, combined with electron probe micro-analysis (EPMA), as was discussed in chapter 2.4.2 could show if the zinc coats grain boundaries or not.

For the zinc covering the features at the upper limit temperature, a different mechanism is assumed. Because 900°C is just below the boiling point of zinc, it is assumed that the zinc will penetrate the material slightly, causing some crack formation. However, as the material starts reducing in cross-section, either by necking or by the formation of the crack, the temperature locally spikes, leading to evaporation of the zinc. The evaporation will prevent further crack growth and cause the remaining material to fail in a ductile manner. In this case, the zinc still present on the surface and in the feature would be a result of zinc depositing back on the steel after cooling. This requires further investigations to confirm. A confirmation of the assumption can be reached by finding that the zinc still present on the sample is a result of deposition of the evaporated zinc after cooling. The irregular zinc coating found in the 900 °C sample by SEM analysis does indicate that the zinc is deposited during the cooling process. Another indication could be that the zinc still present consists of zinc oxides. Instead of evaporating, the high temperature leads to the zinc more quickly reacting with the oxygen still present in the test chamber. The formed zinc oxide has a significantly higher melting point than zinc (1975 °C [54]). As the zinc oxide will therefore be solid, no zinc will penetrate the grain boundary.

The EDS analysis of the fracture surface of samples at the upper and lower limit temperatures reinforces the analysis given above. In both cases, zinc does wet a small length of the fracture edge next to the original zinc coating, but most of the fracture does not seem to be covered/concealed.

5.1.2 Holding time

The relative fracture toughness curve for the different holding times at a temperature of 850 °C and a strain rate of 0.13 s^{-1} (figure 4.3) shows that the ductility of the sample recovers as the holding time increases, reaching a similar value to the samples outside of the temperature related ductility trough after around 1 min of holding. The first point in this graph, where no holding time is applied, shows a large error bar. This is to be expected, as the thermocouple only measures the temperature in the centre of the sample. As soon as the thermocouple measures the requested temperature, the load is applied. Due to the localized nature of the temperature measurement, this results in a temperature situation where a homogeneous temperature zone cannot be assured. Consequently, a high variability will be induced in the results for extremely low holding times.

The fact that the ductility is recovered as holding time increases is an interesting finding and could have several explanations. Considering the findings of chapter 2 and of the previous section, two possibilities will be discussed.

First, the degree of austenitisation is a likely reason for the recovery of the ductility. As the system remains at a temperature leading to stable austenite, the austenite fraction and the austenite grains will grow. The longer the system remains at the temperature, the closer to equilibrium the austenite phase fraction becomes. Using austenite transformation kinetics for different steels measured using dilatometry at a low heating rate of 0.05 K/s at around 850-900 °C, the austenite growth kinetics can be estimated [55]. Using these values, at 850 °C, where figure 5.1 suggests that for equilibrium the steel is fully austenitic, the transformation will take roughly 120 s [55]. Because the transformation will start during heating when the intercritical temperature is reached, the transformation is expected to occur fast initially and to slow down as the austenite fraction increases. As discussed in the previous section, the grain boundary energy of austenite-austenite grains is significantly lower than the grain boundary energy of ferrite-austenite grains. So, as the transformation progresses, ferrite grains transform to austenite grains. Initially, this will result in an increase in the number of ferrite-austenite grain boundaries, therefore increasing the susceptibility to LME and reducing the fracture toughness in short holding times. The amount of ferrite-austenite grain boundaries will reach a maximum, before being replaced by austenite-austenite grain boundaries. At this point, the material will become less susceptible to LME as the amount of austenite increases. Initially, this will be relatively quickly, as can be seen from the results between 5 and 20 s in figure 4.3. As the amount of austenite approaches equilibrium, the transformation will slow, reducing the slope of ductility recovery. Figure 4.3 shows that after 60 s holding time, the ductility recovery has not plateaued yet, so it is expected to continue until around 120 s, where the transformation is complete. Investigating the microstructure, specifically prior-austenite grain boundaries, could help in confirming this. One way to reveal PAGB's more clearly than was achieved in this study, is to etch the material for around 1 minute using a CrO$_3$+NaOh-picric acid solution heated to 120 °C [56].

Second, the diffusion of zinc is a possibility. Similar to the austenitisation theory outlined above, the zinc will diffuse into the iron and vice-versa to reach an energetically favourable solid solution of Fe-Zn. As the system remains at a high temperature for longer, more zinc can diffuse into the bulk or form intermetallics with different properties underneath the original zinc coating. This process will reduce the amount of liquid zinc left to penetrate potential crack-tips when loading starts. Also, the liquid zinc left could

accumulate in certain areas. For example, the surface tension of the liquid zinc at 850 °C is around 0.7 J/m^2 [51], higher than the reported zinc on iron interfacial energy of 0.245 J/m^2. This will lead to zinc to form droplets, removing zinc from certain areas. Because LME does not initiate cracks, but only propagates them, this reduces the chance that a crack initiates underneath the liquid zinc. Evidence for the second possibility can be seen in figure 4.12. The EDS analysis of the zinc coating around the fracture area shows a non-uniform distribution of the zinc coating, with many large gaps between the coating. As the sample with a high holding time is the only sample that exhibited this behaviour of the zinc coating, this second explanation seems to have merit.

However, further research is necessary to confirm the latter hypothesis. One method to test the theory regarding austenite growth kinetics would be an extensive synchrotron-XRD study. Synchrotron-XRD is an XRD method that allows for *in-situ* measurement of phase composition of a metal. This can be used for *in-situ* measurement of the austenite during testing or the formation of Fe-Zn grains caused by zinc diffusion [57].

The SEM and EDS analyses of the samples with no holding time and longer holding time (figures 4.9 to 4.12) reveal a similar effect as the temperature samples. On the one hand, with no holding time, as predicted by the fracture toughness graph, the sample displays clear evidence of a brittle fracture caused by liquid zinc: little reduction of cross-section, several cracks and incomplete fractures and zinc wetting the inside of the cracks and the entire fracture surface. On the other hand, with a longer holding time, the fracture shows a clear ductile nature, and no zinc is found at the fracture surface.
Additionally, another clear sign of liquid zinc embrittlement can be seen in the no holding time sample. In the crack tip, zinc has penetrated beyond the crack tip, ostensibly through grain boundary penetration and separation as evidenced by the zinc following an irregular path, deflected by what is assumed to be an encounter with the next grain boundary. Besides further reinforcing the fact that the embrittlement is caused by liquid zinc, it also confirms that liquid zinc embrittlement of steel follows the same mechanism as the liquid gallium and solid aluminium system: grain boundary penetration of the liquid metal leading to loss of cohesion of grains.

5.1.3 Strain rate

The effect of strain rate ranging from 0.013 to 1.3 s^{-1} on embrittlement is shown in figure 4.3. The strain rate of 1.3 10^{-3} s^{-1} was tested and visually confirmed to have failed in a highly ductile manner as shown in figure 4.15. It should, however, be mentioned that this specific test could not be incorporated in the quantitative analysis due to a user error with the Gleeble. Data sampling rates were set too high for the extremely low strain rate, resulting in too many data points for the analysis software to handle.

The test on strain rate dependency of LME were carried out at a temperature of 850 °C and a holding time of 10 s. At low strain rates, there is little reduction in fracture toughness and as strain rate increases the fracture toughness reduces until a plateau is reached. At first glance, the fracture toughness graph appears to be roughly the opposite of the curve of the holding time. Naturally, the same factors influencing LME occurrence as a function of holding time play a role in the strain rate dependency. A lower strain rate translates to a longer time the sample is exposed to the elevated temperature.

An analysis is performed to compare the effects of applied strain rate and holding time. If strain rate would have a comparable effect as the hold time, the strain rate equivalent to a holding time would have the same fracture toughness. An equivalent holding time is calculated using the simplified equation:

$$t_{hold,eq} = \varepsilon_{yield}/\dot{\varepsilon} \qquad\qquad (eq\ 5.1)$$

where $t_{hold,eq}$ is the equivalent holding time, ε_{yield} is the strain when yielding of the material starts, taken from the stress-strain curve (figure 4.1) to be roughly 0.02 and $\dot{\varepsilon}$ is the strain rate. The equation determines the time it takes for the material to start plastically deforming. The yield strain is taken, because figure 4.1 showed that LME did not affect the elastic part of the curve. The plastic part is immediately affected at 850 °C. Using the lowest strain rate on the graph: 0.013 s^{-1}, the equivalent holding time would be 1.5 s. The values for relative fracture toughness for this strain rate and holding time do not match. So, an additional mechanism is behind the strain rate effect on LME susceptibility. Two possibilities will be outlined:

i) The degree to which the system experiences strain rate sensitivity with regards to LME. At high strain rates, the loading situation is highly dynamic, while lower strain rates, especially 0.013 s^{-1} and lower, can be considered near static. At these temperatures, a steel such as used in this study can achieve dynamic recovery. A certain critical stress must be reached for dynamic recovery to start. The critical stress has been found to decrease as strain rate decreases [58]. Therefore, a lower strain rate will lead to a higher degree of dynamic recovery. The dynamic recovery process causes the atoms to rearrange themselves to accommodate the stress in the material. The accommodation of stress in certain parts of the material leads to a lower stress concentration at crack tips, thereby decreasing the susceptibility to LME. As dynamic recovery requires less stress at lower strain rates, this would explain the ductility recovery at lower strain rates. The Section 5.2.2 will elaborate on this possibility.

ii) The role of zinc diffusion. At the exceptionally low strain rates, a possibility is that the liquid zinc does penetrate the grain boundary to a small degree. However, strain energies are not high enough to immediately lead to loss of cohesion, allowing the zinc to diffuse from the grain boundary into the grain. This could lead to a stronger cohesion of the grain boundaries, because the zinc will form small additional grains as revealed through EBSD in section 2.4. These grains might have a stronger cohesion than austenite-austenite grains. The zinc diffusion will be further explained in the next section.

SEM micrographs of the etched high strain rate sample were meant to reveal prior austenite grain boundaries and show that cracks propagated along austenite grain boundaries and zinc penetrated the boundaries. However, several issues were encountered: firstly, etching was not able to identify prior austenite grain boundaries on a scale allowing for investigation of the cracks. Indications of prior austenite grain boundaries are found, *i.e.,* unidirectional needle-like ferrite structures within areas (acicular ferrite forming in austenite grains) in figure 4.14 and allotriomorphic ferrite (ferrite forming at austenite grain boundaries) in figure 4.15. However, they could not be revealed to the extent necessary. Additionally, to reveal the few indications of prior austenite grains, the zinc was etched away too much to be consistently identified using EDS. Still, clear signs of LME can be identified: no reduction in cross section and many cracks that appear to be coated in zinc, although not confirmed.

In the last image of figure 4.14, *i.e.,* the microstructure around the crack tip, signs of the crack propagating intergranular can still be identified. The crack tip is clearly deflected several times, as marked, in a manner that suggests encountering an obstacle. Because it is known that the crack grew while most of the material should be austenitic, it can be assumed that this is an indication of the crack encountering a grain boundary and being deflected to follow the grain boundary.

More research should be performed to fully confirm this observation. Identification of prior austenite grain boundaries should be achievable using EBSD and zinc distribution can be measured using a more powerful elemental analysis technique such as EPMA.

5.1.4   Zinc diffusion

In the previous section it was mentioned that diffusion of zinc in the iron possibly plays an important role. In this section the diffusion distance is estimated by Fick's first law of diffusion.

$$x_{max} = \sqrt{2Dt}$$
(eq 5.2)

where x_{max} is the maximum diffusion distance of the diffusing element, D is the temperature dependent and phase independent diffusion coefficient for the interdiffusion of zinc in b.c.c. iron as experimentally determined by [59] and t is the time.

A rough estimation can be made of the maximum distance zinc can diffuse into the iron from the crack surface. These estimates are plotted as function of time for different temperatures along with the temperature dependent diffusion coefficient for the temperatures used, see figure 5.1.
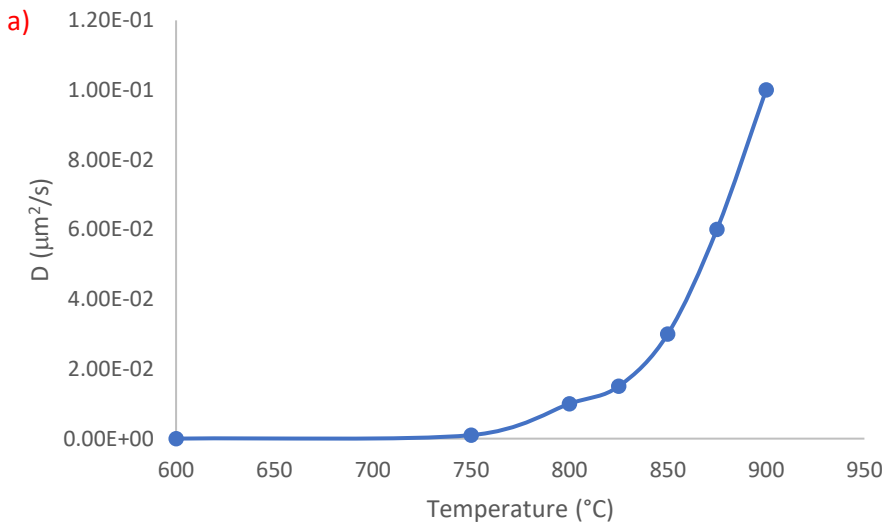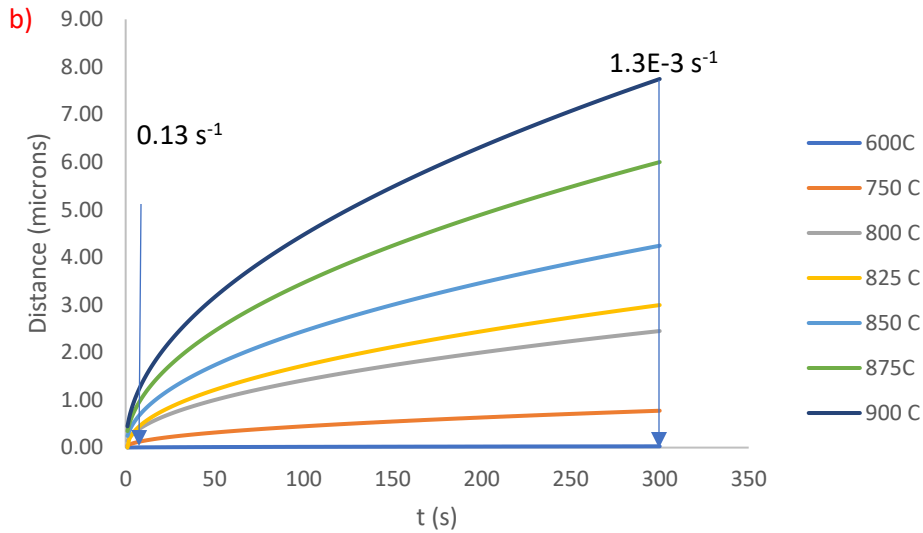
Figure 5.1: a) zinc in iron interdiffusion coefficient calculated for the temperatures used [59]b) Interdiffusion distance of zinc in iron as calculated for the different temperatures used in Gleeble testing. In the figure the time estimated until fracture occurs is indicated for two strain rates used.

These estimations obviously show that the diffusion distance increases with time and temperature. At fast strain rates, where time until fracture is limited, the zinc can diffuse less than 1 μm into the iron. A maximum distance of 8 μm can be reached at the slowest strain rate 0.0013 s^{-1}.

This result shows that, for the higher strain rates (0.13 s^{-1}) and higher, where LME was clearly observed, the zinc would only be able to penetrate 1 μm or less into the bulk from the crack. The limited ability of zinc penetrating into the bulk material from the crack surface can be confirmed in the EDS analyses of the brittle samples. The zinc distribution seems to follow the crack very closely, only showing trace diffusion into the bulk from the crack.

For the lower strain rates, the diffusion of zinc into the bulk cannot be investigated in this manner, because no cracks formed. However, the calculation shows that at the temperature under investigation for the low strain rates: 850°C, zinc could penetrate several microns into the material, either from the surface, or the grain boundaries, before fracture occur. This could be enough diffusion to significantly deplete the amount of liquid zinc available at the surface for LME or remove the zinc diffused into the grain boundaries before it leads to grain separation. The simple equation therefore predicts that the diffusion of zinc into the bulk, resulting in depletion of zinc at the grain boundaries, could be a reason for the lower susceptibility of the system to LME. However, this should be further investigated, using EBSD and EPMA to quantitatively determine how much zinc has diffused into the bulk, using EBSD to determine what has happened with the diffused zinc, *i.e.,* present in the bulk around PAGB's.

5.1.5 Gleeble Finite Element Aanalysis

In this section, results of the COMSOL FEA simulations are shown. The simulation focusses on the most susceptible conditions in Gleeble hot-tensile testing, a temperature of 825°C, a strain rate of 0.13 s^{-1} and 10 s hold time. Simulations for LBW will be discussed in the next section.

Variables under consideration are the total stress, the strain rate and for the LBW experiments the temperature.
Figures 5.2 and 5.3 show the development of the von Mises stress and the strain rate of the Gleeble sample at 825°C, 0.13 s^{-1} strain rate with a holding time of 10 s during the loading of the sample, respectively.
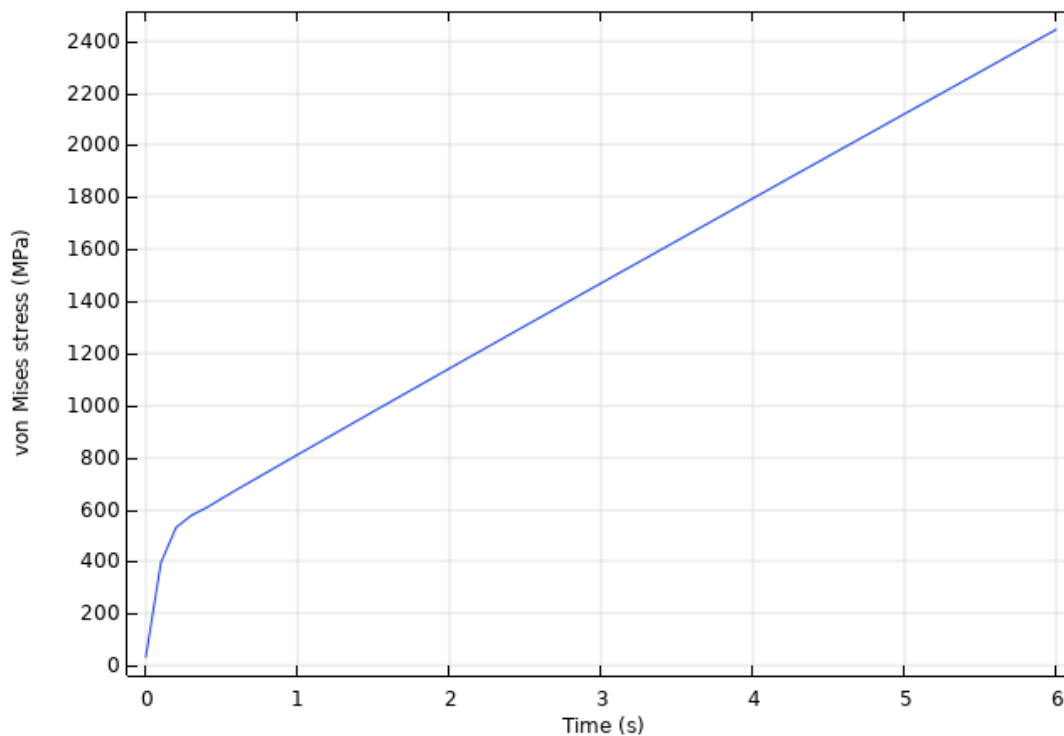
Figure 5.2: simulated von mises stress development during loading of a rectangular Gleeble sample at 825 °C, 0.13 s^{-1} strain rate with a holding time of 10 s.
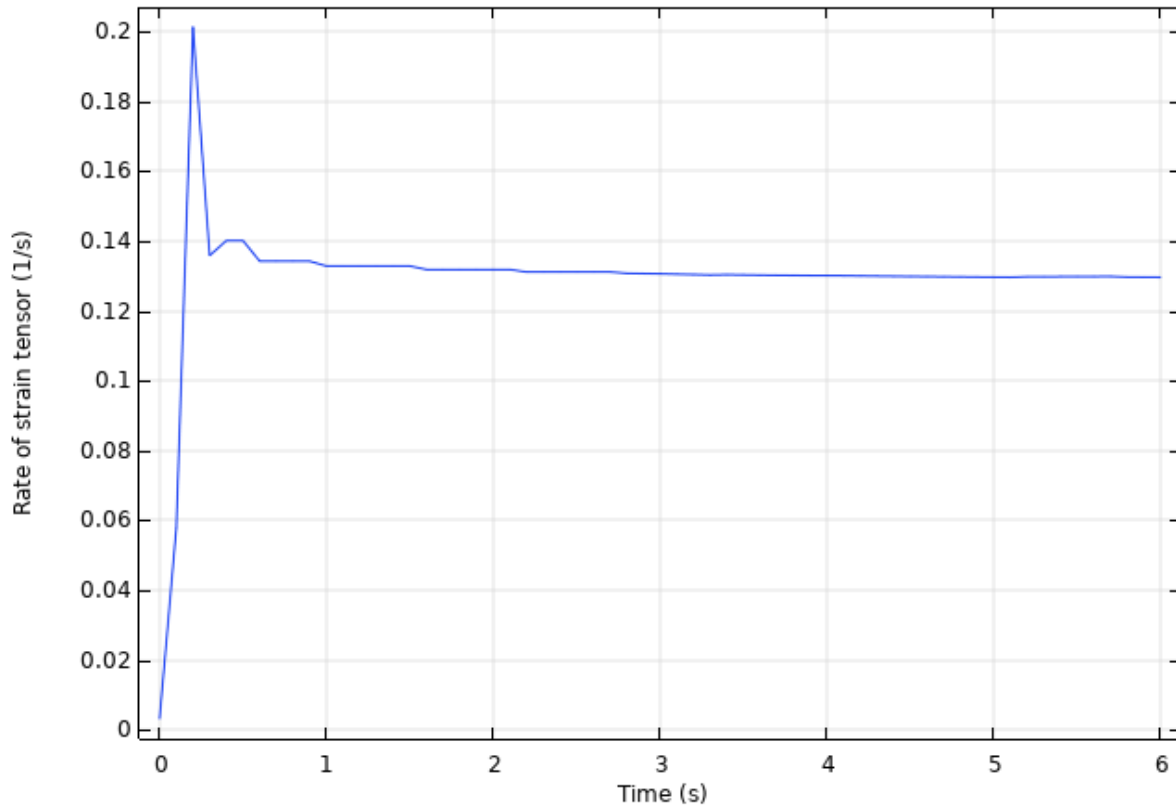
Figure 5.3: simulated strain rate development during loading of a rectangular Gleeble sample at 825 °C, 0.13 s^{-1} strain rate with a holding time of 10 s.

These simulated results are as expected for the Gleeble sample, however with a few expected exceptions. The stress develops linearly after passing the yield strength, which does not resemble reality, due to tangent modulus changing as strain increases due to hardening effects. However, the simplified tangent modulus was chosen to reduce computational time. Since the sample, if coated with zinc fails quickly after being strained beyond the yield strength, the simplified tangent modulus will not have a significant consequence when comparing data. For reference, this specific sample failed in the Gleeble experiment after around 1.5 s, not long after yielding. A comparison with the stress-strain curves in figure 4.1 for higher temperatures also shows that the sample fails around the point where the tangent modulus would significantly change. of the discrepancies in the strain rate result, *i.e.,* the peak in the beginning, followed by a drop to the expected strain rate is a consequence of the ramping function for the prescribed displacement used to ensure the boundary conditions do not break down in the simulation.

Since there is a homogeneous temperature in the centre of the specimen. Zinc is present in a liquid form and the temperature is within the intercritical range for austenite formation. In this area, LME had occurred, so the stresses and strain rates shown with the FEM are within the susceptibility range.

Using experimental results from Gleeble and the simulated Gleeble results, the susceptible ranges are identified as follows:
Temperature: 800-875 °C
Stress: At least above the yield strength

Strain rate: above 0.1 s^{-1}.

The required strain rate is set slightly below the strain rate of the Gleeble results. Susceptibility of the material to LME is highest above the strain rate of 0.13 s^{-1}, but slightly below 0.13 s^{-1}, some susceptibility remains.

5.2 LME in LBW

This section will discuss the findings related to LME in LBW. As mentioned before, laser beam spot and linear welding has been carried out while the specimen was loaded in tension.

In section 5.2.1. the evolution of the temperature and the stress state during the welding time and the subsequent cooling period will be analysed and the significance to LME susceptibility will be discussed. Secondly, the results of the microscopy analyses of specimens in relationship with the occurrence of LME in LBW will be addressed.

5.2.1 Effect of experimental parameters

During the laser spot welding experiments a melt pool is created, indicating that in this zone the temperature is in excess of the liquidus of the steel. Moving away from the centre of the weld, the temperature will decrease and areas where liquid zinc is present can be found. Depending on the conditions applied, this area can be small (high laser power for short times) or larger (lower laser power for longer times).

The tensile stress state of the specimen was monitored during the welding process. The stress at the moment the laser was turned on was constant. In the experimental setup the stress is manually applied until a certain fixed strain is reached; the overall elongation of the specimen is fixed. Any changes to the stress state are therefore a direct result of the energy input of the laser beam and the resulting thermal cycle, *i.e.*, heating, melting, solidification and cooling. Because the highest applied stress used was 100% of the yield strength, no significant plastic deformation would occur without the application of the laser.

The stress state as shown in figure 4.16 reveal that, upon heating, the stress drops significantly. This decrease in stress is the result of the temperature increase of the specimen, which as a result would like to expand, however it is prohibited by the fixed clamping condition. When the heat input is increased, by increasing the laser power or by extending the beam on-time, the reduction in measured force (stress) is larger. Note that the duration of the heating time is relatively low. When the laser power is switched off, *i.e.*, the cooling stage, an increase in stress can be seen as a result of thermal contraction and the occurrence of eventual phase transformations. However, the stress recovers slowly, plateauing at a point below the original stress state. The extent of the drop in stress during heating will be affected by a reduction of the Young's Modulus as a function of the temperature and a decrease in the yield strength as function of temperature inducing plastic deformation. As the stress does not return to its original value during cooling other phenomenon are also active, including thermal stress relief, the morphology, and dimensions of the heated area, i.e., a thinner melt pool region, the formation of hot-cracks or liquation cracks and the plastic deformation [42].

For LME to occur, the only stresses likely to contribute to the embrittlement/liquid metal penetration are the stresses present during the heating stage. During the heating stage, certain areas are in the temperature range in which the material is susceptible to liquid metal penetration as shown in chapter 5.1. Figure 4.17 showed the temperature at around 1 cm from the fusion line as a function of time for several heating conditions. The duration of these experiments is larger and the laser power lower as compared to the experimental results depicted in Figure 4.16, but the total net energy input is similar. All the curves show that initially the temperature rises quickly, but the increase slows down as zinc starts melting in the melt pool at 250 °C, due to the latent heat of melting. Due to the different laser beam conditions (laser power and time) the amount of material affected will change influencing the effect of latent heat on the temperature curve. This can be most clearly seen for the experiment conducted at 300 W. For longer exposure times and higher laser powers, the size of the melt pool increases, therefore under these conditions the highest temperatures are achieved at the location of the thermocouple. At the peak temperatures reached by the 300 W experiment and the 240 W for 20 s experiment, the evaporation of zinc from the melt pool affects the measured temperature. The evaporation caused expulsion from the melt pool, shielding, and scattering the laser slightly, which caused temperature fluctuations as measured by the thermocouples.

The curves also show that the heat input affects the duration that the material is exposed to the presence of liquid zinc; this is the heat affected zone, where zinc is not evaporated. For the higher laser powers used in the stress evaluation, this means that higher temperatures are likely to occur in the area where the thermocouples were, albeit with a shorter time window within the susceptible range. With the higher heating rate caused by higher laser powers, the thermal stresses and strain rates caused by the heat input will be higher, potentially increasing the susceptibility to LME. However, the higher heat input will also increase the temperature in and around the melt pool. The higher temperature will decrease the Young's modulus and yield strength at those areas. So, more of the strain applied through the setup will be accommodated in these areas. Although the susceptible temperature range will also occur during cooling, it becomes more likely that the material will experience stress relief through solidification cracking [8]. Therefore, more stress relieving mechanisms will be competing with the LME process, reducing the likelihood for LME to occur. A comparison between the samples shown in figure 4.16 reveals that for spot welded samples, the stress recovery remains around a relatively constant value of approximately 30 to 40 MPa, regardless of welding power or applied external load. This suggests that, even when the sample is loaded below the yield strength, the thermal stresses caused by the laser increase above the yield strength whereas only a strain related to the thermal stresses of around 30-40 MPa can be recovered elastically. However, for the linear weld, the recovered stress is significantly higher, exceeding 100 MPa. Consequently, this shows that the linear welding method will add significantly lower thermal stresses, leading to a lower degree of plastic deformation, possibly decreasing the susceptibility of the sample to LME for linear welding as compared to spot welding.

As can be seen in figure 4.18 and appendix C, necking could be observed in the area around the weld pool. As was seen in figure 4.1, LME has no noticeable impact on the elastic part of material deformation. Therefore, without any changes to the stress state, no LME would occur when loading below the yield strength. However, thermal stresses do add to the stress state and considering the aforementioned necking, most likely lead to plastic deformations in the material. Combining these results, all conditions determined in chapter 5.1 to be necessary for LME are present in LBW, *i.e.,* temperature in the susceptible temperature range, plastic deformation, short period of time held at high temperature and, most likely,

high local strain rates due to thermal stresses (as evidenced by noticeable necking after short welding times of a second or lower). These results suggest that LME will occur in the LBW setup, provided that all the required conditions are present at the same locations. Due to the high temperature gradient (melting in the weld pool and no obvious alteration to the zinc coating near the edge of the sample) this last condition is not necessarily met.

Initially, LBW samples were cross sectioned in a relatively random manner, like for Gleeble samples, *i.e.,* an area was identified that was expected to be susceptible to LME. For the laser experiments cross sections were made in the HAZ, parallel to the loading direction, as cracks were expected to be perpendicular to loading direction. Where the semi-random cross-sections made in Gleeble samples consistently produced cross-sections revealing multiple LME cracks, the semi-random cross-sections made of LBW samples did not produce any identifiable cracks, as shown in the images in appendix E. From the difficulty in locating evidence of LME cracking using the semi-random method, it follows that, should the LBW setup produce LME cracks, they will be constrained to small and specific zones around the weld, due to the high temperature gradient, as mentioned in section 5.2.1.

In order to better identify LME susceptible areas, a different approach was used. As cracks are expected to initiate at the surface of the sample, *i.e.,* the only area where liquid zinc is present, the surface was investigated first visually. After the experiment, the surface of the sample was cleaned, using only ethanol and a brush, to remove some oxides and contaminants at the surface, without grinding the surface. As shown in figures 4.18 through 4.21, the surface did reveal several visible crack-like features.

Some features, such as the ones marked in figure 4.19 and the centre of the fusion zone in figure 4.21, are transverse crack-like features in the fusion zone. The melting point of the steel is several hundred degrees higher than the boiling point of zinc and as no liquid zinc will be present, the features at these locations cannot be related to LME. Therefore, those features were identified as being solidification cracks [8].

The other features observed in the mentioned figures, however, could be related to LME cracks. Circumferential and transverse crack-like features are present in the HAZ.

1. Spot welds

Although the surface investigations show signs of LME cracking matching expected LME crack locations and morphology in spot welded samples, a confirmation of LME cracks must be obtained. The most reliable method of identifying LME cracks is an analysis as was used for Gleeble testing. The approach is to find in a cross section a crack starting from the surface into the bulk and using SEM to show evidence of intergranular cracking and EDS to show penetration of the zinc coating into the crack and crack tip. If wetting of the crack with zinc is observed this provides evidence that LME occurred. In the procedure the position of the crack was marked, and precise cross sections were made through the identified features on the surface. One such a cross-section is shown in figure 4.22, where the yellow line indicates the cross section. This cross section passes through a circumferential crack marked with red arrows in top left image of figure 4.18 and the transverse features marked in the bottom right image of figure 4.18. SEM images of these locations are marked in figure 4.22. As can be seen from the SEM images zoomed to 200x, no

signs of LME cracks can be identified, even when the cross-sections are made to specifically cross the identified features.

In the case of RSW, most LME cracks will be circumferential, which is also mentioned frequently in the literature [9] [10] [12]. However, in the LB spot welds circumferential LME cracks are not necessarily expected. The main reason for this is the difference in loading state. In the LBW experiments the largest applied external stress is a unidirectional tensile stress, which would most likely lead to transverse LME cracks as was the case in Gleeble samples. In RSW the highest applied stress is the compressive stress applied by the electrodes, but the stress leading to LME is the shear stress around the electrode, which has a circumferential shape. Nevertheless, circumferential cracks are still feasible in LBW, provided the thermal stresses created by the circumferential temperature gradient are high enough.

2. linear welds
In addition, figure 4.20 shows a single feature found in the linear welded sample. Despite the fact that a significantly larger HAZ is present in the linear weld as compared to a spot weld, only one single feature was identified.
A reason could be the lesser degree of thermal stresses present in linear welds as mentioned in section 5.1.1. This can also be seen in the steep drop in load to a level of approximately 20 MPa when a linear weld configuration is applied. A further study, more focussed on comparing laser beam spot welds and laser beam linear welds could provide further insight into the differences and reasons for the lower occurrence of crack-like features.

3. welded plates
Finally, two samples welded together in overlap configuration were investigated. The interface between the two samples creates an area where the zinc becomes liquid and is trapped. In this experiment the chance to induce an LME crack in the interface might increase, provided appropriate conditions/requirements for LME to occur are fulfilled. Because this approach does not allow to inspect the surface visually, a thorough examination was done instead. The cross section was made, ground and polished again several times between consecutive SEM investigations, in order to capture a large area. Figure 4.23 shows such a cross section, where the transition from the fusion zone to the HAZ can be identified by the zinc interface disappearing towards the fusion zone. Using this method to identify the HAZ, EDS measurements were performed both on the zinc coatings and the interface in this area, *i.e.,* just above the area where the zinc started appearing. However, also under these conditions no clear evidence of LME cracks could be identified as shown in figure 4.24. Figure 4.24f, which is a cross section showing the bottom surface zinc-coating, does reveal a feature resembling an LME crack. It shows a small amount of zinc penetrating. However, the 'crack' is exceedingly small, and based on these measurements it cannot be fully concluded that it is an LME crack.

4. Summarising the characteristics of LBW

These results for LBW show that, conditions should be present in the LBW setup to initiate LME. However, it appears to be difficult to find and irrefutably identify LME cracks. There could be two reasons for the absence of identifiable LME.

In the first case, the conditional requirements leading to LME are never present in the same location in an LBW sample at the same time. In that case, no LME occurs, and the surface features shown by optical microscopy are not LME cracks, but other features. One possibility is the occurrence of liquation cracks. In agreement with literature, austenitic steels (which the steel would partially be in the susceptible temperature range) are susceptible to liquation cracking the HAZ, close to the fusion line [60]. As the inspected area is the same as the area susceptible to liquation cracking, this might be a competing mechanism. Liquation cracking is the result of partial melting of the material along grains, occurring due to the high thermal gradient. The cracks are often extremely small and mostly present at the surface of the sample. In the mentioned literature, the cracks were also identified at the surface, but cross-sectioning through the crack for further analysis proved to be impossible due to the cracks not penetrating into the bulk or being too thin when penetrating [60].

In the second case, LME cracks do form as shown in figure 4.24, but the zinc penetration is extremely limited and remain highly superficial. In this case, LME does occur, but not in high enough numbers or without sufficient severity that they can be consistently identified using the SEM and EDS methods used here.

In both cases, a likely reason is the lack of an externally applied strain rate in the LBW setup. Whereas the Gleeble hot-tensile samples had a uniform applied strain rate in addition to potential thermal gradients, the loading state in the LBW setup applies a single load and the total global strain of the system remains constant throughout the welding. As was seen in Gleeble hot-tensile testing, a strain rate is necessary to create a system susceptible to LME. The lack of LME in LBW suggests that the changes in the stress distribution due to thermal stresses induced are not sufficient to realise local strain rates that are high enough.
It should be mentioned in RSW an external strain rate is applied neither. However, the thermal energy in RSW is applied almost instantaneously after applying the load, while the manual loading in the LBW setup required time between loading and starting the laser. Potentially, this results in a system in RSW that applies a stress almost simultaneously to applying the heat, whereas the loading and welding in the LBW setup are clearly separate. Potentially a higher applied tensile load in the LBW setup could result in observable LME, but it will be difficult to prevent the material failing simply through thermal stresses. As can be seen in figure 4.16, when applying 100% of the yield strength, the laser heat input almost drops the stress to 0 MPa. Should this occur, the material most likely fails, as the strength of the material is reduced below the applied stress when it is heated.

Most likely, it will be necessary to use a different LBW setup, where the load is applied through a system that can be controlled remotely, allowing strain rates to be applied during the welding process.

5.2.3   LBW Finite Element Analysis

In this section the Finite Element Analysis (FEA) of the LBW specimen resulting in the highest degree of features in the HAZ resembling LME, *i.e.,* 800W for 2 s, defocused to a 1 mm spot diameter and loaded to 100% of the yield strength, will be discussed. FEA of two other experimental conditions (1500 W for 0.75 s with a 1 mm spot diameter and 300 W for 20 s with a 7 mm spot diameter) will also be briefly discussed.

With the help of the FE models the location where the conditions meet the requirements for LME to occur can be estimated. This allows to compare the conditions prevailing to the occurrence of LME.

For the laser model, figures 5.5 through 5.7 show the simulated temperature, the longitudinal stress, and strain rate parallel to the loading direction, respectively at three different locations around the weld. Figure 5.4 shows the approximate positions of the probed locations used in the analysis. The parallel strain rate is chosen, as that is the strain rate that most likely led to the transverse crack features found during characterisation.

Figure 5.4: LBW Spot weld surface, welded at 800 W laser power for 2 s with a spot diameter of 1 mm. The approximate probed locations for FEA are marked. a) First location, called inner edge HAZ, b) second location, called middle of HAZ, c) third location, called outer edge HAZ
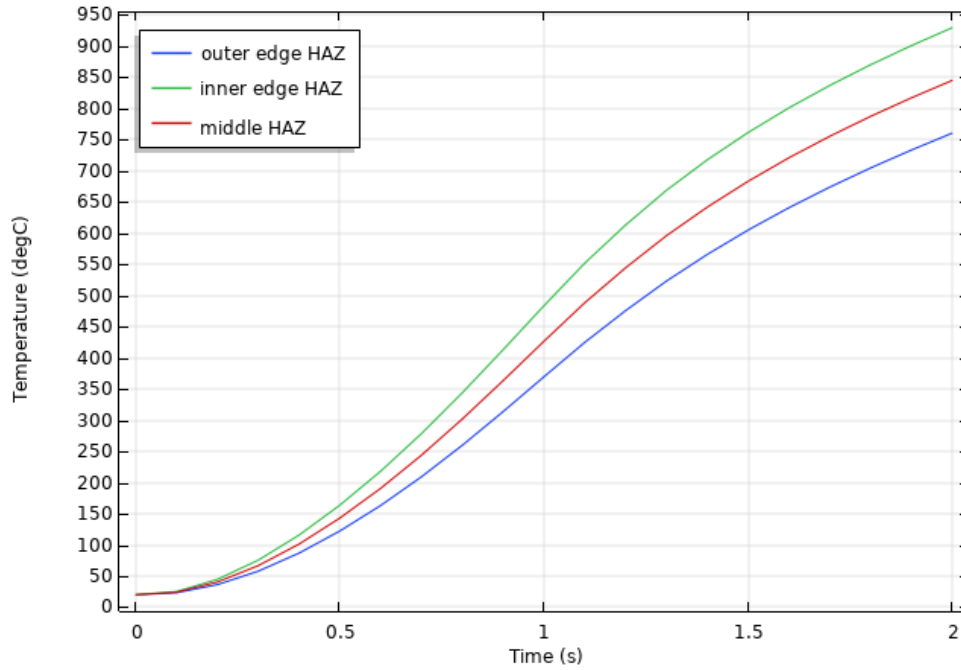
Figure 5.5: simulated temperature evolution during LBW at 800 W beam power for 2 s, defocused to 1 mm loaded to 100% of the yield strength probed at the inner edge, the outer edge, and the middle of the HAZ.
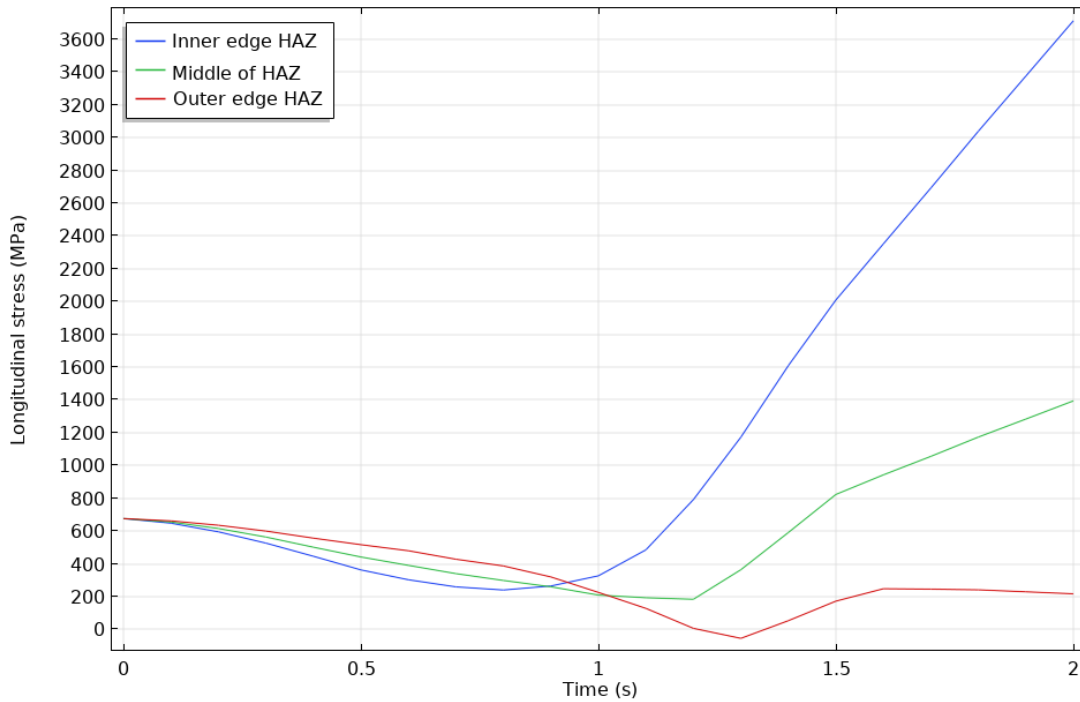
Figure 5.6: simulated stress evolution during LBW at 800 W beam power for 2 s, defocused to 1 mm loaded to 100% of the yield strength probed at the inner edge, the outer edge, and the middle of the HAZ.
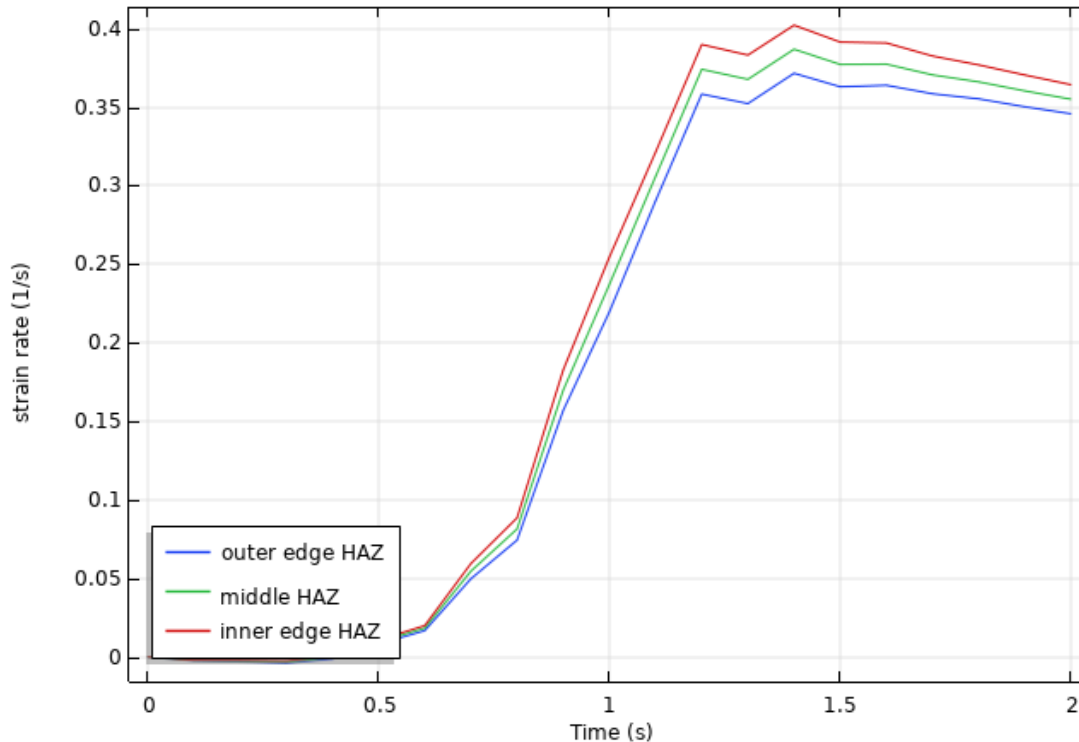
Figure 5.7: simulated strain rate parallel to loading direction evolution during LBW at 800 W beam power for 2 s, defocused to 1 mm loaded to 100% of the yield strength probed at the inner edge, the outer edge, and the middle of the HAZ in the centre line of the plate.

Using the simulated graphs, values of the three variables can be compared to find if susceptible ranges of the properties coincide at any point during the laser welding. The HAZ used in the model was determined from the microscopical analysis and is taken at around 1 mm wide.

The inner probed location, roughly the edge where liquid zinc is still present, lies within the temperature susceptible range, above 750 °C between 1.6 and 1.8 s into the welding process for the condition simulated. At these times, the strain rate (0.35-0.4 s⁻¹) and stress (>1000 MPa) are clearly also in the susceptible range. The middle of the HAZ lies in the susceptible temperature range slightly later, between 1.8 and 2 s. Like the inner edge, this coincides with susceptible values for both the strain rate and stress, however, the stress criterion is only just met. The outer edge, however, does not reach the susceptible temperature range nor stress range. Similar FEM results were obtained for other experimental conditions (300 W for 10 s and 1500 W for 0.75 s) the results are shown in appendix E. For 300 W for 10 s, conditions were not extreme enough to lead to LME. The temperature only just reached the melting temperature of zinc and stresses and strain rates remain relatively low. For the laser power of 1500 W for 0.75 s, susceptible conditions are just reached in small areas. With a longer welding time, a relatively large susceptible area could be obtained. However, an attempt to weld at these powers for longer times quickly resulted in melt pool collapse, indicating that extended welding times are not relevant.

Therefore, the simulations suggest that conditions could be met for LME to occur during laser beam welding. Comparing the locations where the HAZ might be susceptible to LME according to the simulations

and the identified features found, gives some indication that the features are LME cracks. However, the difficulty in identifying the features as LME cracks in SEM reinforces the conclusion given before, that the conditions prevailing do not cause LME cracks to penetrate deep into the bulk. Additionally, the time window where parts of the material are susceptible to LME is exceptionally short, less than 0.5 s. This means that small uncertainties encountered during actual welding might prevent LME from occurring in certain areas of the HAZ. For example, one such uncertainty encountered during laser welding is the vaporisation of zinc from the fusion zone oxidising just above the surface of the sample, being blown away by the nitrogen cross jet used to protect the laser lens. The scattering of the zinc oxides briefly blocks the laser beam from the sample surface, causing some temperature fluctuations as can be seen in the higher temperature curves of figure 4.17. These small fluctuations can cause certain parts of the HAZ, that would be susceptible, to fluctuate outside of the susceptible temperature range. More uncertainties lie in the fixing of the sample in the load cell. The clamps could freely be located around the longitudinal axis before being tightened. Because the samples were fixed to the loading cell manually, samples could be rotated slightly. This can result in the surface of the sample not being parallel to the laser beam, but slightly slanted, altering the laser spot size, changing the thermal conditions of the sample. Additionally, the manual mounting could result in a misalignment of the two clamps. The misalignment results in a torsional force on the sample, significantly changing the stress distributions in the sample.

The short time window for susceptibility and the time windows being constrained to small areas combined with mentioned uncertainties easily pushing variables outside of the susceptible ranges and areas could be a reason for the difficulty of identifying LME cracks. Only a small number of cracks will form and cracks that will form will likely not penetrate far into the bulk. Hence, even though the LBW setup creates LME cracks, they are too few and too small to identify further with the methods used in this study.

These explanations are all made on the assumption that the used model predicts the conditions in the samples correctly. Although conditions were found to be predicted in the correct order of magnitude, some simplifications were used in the model setup that reduces the accuracy of the model. *i.e.,* The tangent modulus was taken as a linear function, the yield stress as a function of temperature was a stepwise function, instead of a continuous function and the thermal model was fully based on an uncoated sample. So, the effects of different laser absorbance of zinc and the thermal effects of zinc melting, and evaporating are not taken into account. The FE models should be improved upon in these aspects to ensure a more accurate prediction of conditions and therefore, a more accurate prediction of LME susceptible areas in LBW samples.

Further research is recommended to improve the LBW setup to form larger cracks more consistently. If the surface features shown by optical microscopy can be properly identified to be LME cracks, the surface features can be used to perform in-situ measurements of temperature and local strain field as the cracks are forming. Using a high-resolution camera during welding, the cracks could potentially be located as they are growing. With the currently proposed methods, the time windows could be lengthened by using a more diffuse laser at lower beam powers to keep the HAZ in the susceptible temperature range for longer. Longer cracks could be created by changing the setup in such a way that a global strain rate could be applied to the sample during welding. Combined with the high strain rates induced by thermal strains, this could increase the area of susceptible zones and create more extreme stress states leading to more and longer cracks.

5.3 Relevance to RSW

To mimic the conditions in RSW better in the LBW setup closer, another more preferable method is proposed. The current in RSW is applied for short times, in general less than a second. Therefore, the time window for LME susceptibility is comparably short. Figure 5.8 shows a representation of the temperature evolution in the LME susceptible area in RSW [12].
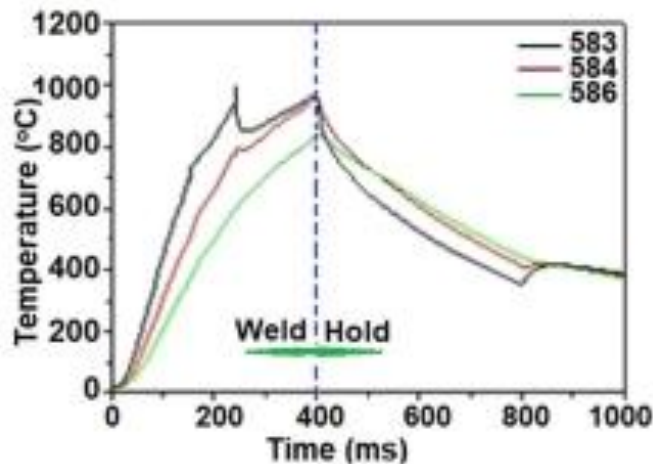
Figure 5.8: Temperature evolution of the LME susceptible area in RSW during welding [12]

As can be seen from the figure, the susceptible area remains in the temperature range between 800 and 875 °C for only around 200 ms, similar to the duration for LBW found in the current study. Yet, clear LME cracks were found in the resistance spot weld, as shown in figure 5.9.
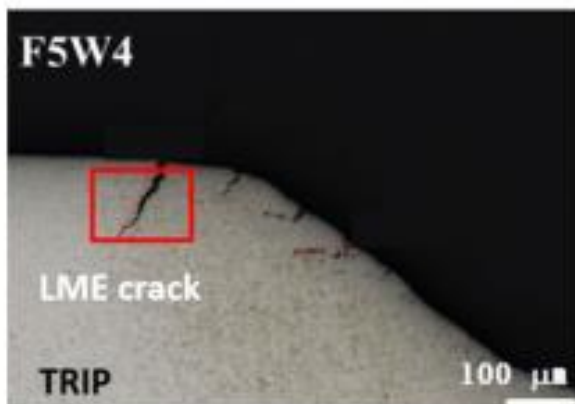
Figure 5.9: LME crack found in RSW of TRIP steel [12]

Apparently, for similar time windows and area where the material is susceptible to LME, results in a different LME behaviour between the RSW and LBW setups.

The first difference that might affect the results can be related to the different steel grades. The steel shown in figure 5.7 is a TRIP steel, while the steel in the current study is a DP steel. Potentially, DP steel is less susceptible to LME compared to TRIP steel. However, the results from the Gleeble hot-tensile tests clearly showed that the DP steel experiences significant liquid zinc embrittlement, so the difference in steels is likely not the only cause.

The other main difference is the severity of external loading in the RSW and the LBW setup.
Firstly, the load in RSW leading to LME is mostly shear in nature, as opposed to the tensile load in LBW. Steels are often significantly weaker in shear than in tension, the ultimate shear strength being estimated around 60% of the ultimate tensile strength [61].
Secondly, both setups create similar thermal gradients, leading to similar thermal stresses. However, in the LBW setup used in this study, the external loading is static and tensile in nature. In the susceptible area in RSW, however, the external loading is first of all more dynamic. The loading by the electrodes is load controlled. This means that, as the temperature increases due to Joule heating, the Young's modulus drops, decreasing the amount of stress. More strain is then applied continuously by the electrodes to meet the prescribed electrode force. Accordingly, the loading situation in RSW contains an element of strain rate, in contrast to the currently used LBW setup. As was confirmed in the Gleeble tests, an applied strain rate greatly increases LME susceptibility. Additionally, a major part of the stress in RSW is in shear, where the material is significantly weaker.

Therefore, the best method to increase the severity of LME in LBW under tension would be to increase the severity of the loading, either further increasing the applied tensile load, making the loading more shear in nature or applying a more dynamic loading method by using a mechanically controlled method of loading.

6. Conclusions

Embrittlement by liquid zinc is a phenomenon occurring in AHSS grades, including DP steel. The zinc penetrates high energy grain boundaries, forming a new interface that leads to loss of cohesion of the grains under load. A specific combination of external load and elevated temperature are required for the material to become susceptible to LME. During resistance spot welding of DP steel automotive body panels, the dome shaped nature of the electrodes combined with the high electrode compressive force, causes liquid zinc embrittlement cracks at the edge of the fusion zone. The LME cracks negatively influence the mechanical behaviour of the welds. To accurately predict LME occurrence and severity and create welding schedules preventing LME the in-situ thermo-mechanical conditions leading to LME need to be known. In part, the local conditions can be determined using finite element modelling. However, to fully understand at what point during the welding process the cracks form, the weld needs to be monitored during welding. Due to the electrodes covering the areas of the weld where LME cracks form, monitoring the cracks as they grow is impossible in RSW. A laser-beam welding under tension setup is proposed as an alternative method to reveal the local thermo-mechanical conditions leading to LME. Opposed to RSW, the laser beam welded surface of the material is uncovered. Therefore, the local conditions could be detected using thermal imaging and digital image correlation.

This thesis focussed on confirming the viability of the proposed experimental setup to find thermo-mechanical conditions leading to LME. To this end, the effect of global thermo-mechanical conditions is investigated using Gleeble hot tensile testing. The effect of temperature, strain rate and time to equilibrate on the extent of liquid zinc embrittlement were explored. LME mechanisms and degree of LME was confirmed using digital microscopy and SEM combined with EDS. LBW welding schedules were applied to dog-bone samples under tensile load to find welding schedules leading to LME in LBW under tension. Again, optical and electron microscopy was used to confirm LME. Finally, FEA using COMSOL were applied to connect Gleeble results to LBW results and modelling results for RSW from previous studies were used to investigate the relevance to RSW.

Based on the experimental and modelling results the following conclusions were made:
- The temperature dependent ductility trough of the steel measured through Gleeble hot tensile testing is relatively narrow: the lower and upper limit of the ductility trough are 750 and 900 °C, respectively. The most significant embrittlement (down to 20-30% of the uncoated fracture toughness) occurs between 800 and 875 °C and was determined to be related to the presence of austenite-ferrite grain boundaries. The lower limit of the ductility trough was determined to be related to the austenite start temperature. The upper temperature of the ductility trough is limited by 1) the boiling point of zinc; As the zinc evaporates, no liquid zinc is left to cause embrittlement, 2) the extent of austenitisation becoming higher, leading to more austenite-austenite grain boundaries, which were determined to be less susceptible to LME than austenite-ferrite grain boundaries.
- From the holding time and strain rate results, it is concluded that the system must be sufficiently dynamic to become susceptible to LME. Under strain rates of 0.13 s^{-1} and above a holding time of 10 s, the ductility is quickly recovered. The ductility recovery was determined to be a result of zinc depletion from crack surfaces through diffusion for both variables. At a low strain rate, the system

will have time to accommodate more of the stress by dynamic recovery, at higher holding times, the phase fraction of austenite will reach its equilibrium composition, which is fully austenitic at the tested temperatures and therefore less susceptible to LME.

- Material characterisation using SEM and EDS confirmed that the embrittlement seen in the zinc-steel system is indeed liquid metal embrittlement. The cracks show signs of being deflected by grain boundaries and the cracks and fracture surfaces were coated with zinc. Furthermore, zinc penetration beyond the crack tip, resembling penetration of grain boundaries was discovered. All mentioned features are indicative of the LME crack growth process.
- The LBW setup can produce features resembling LME cracks when viewed at the surface. However, the externally applied load must be relatively high (at least 100% of the sample's yield strength). Furthermore, the features could not be confirmed as LME cracks through SEM and EDS.
- FEA revealed that, locally, the LBW setup could create conditions making the system susceptible to LME. Nevertheless, no LME could be confirmed. Provided the model was sufficiently accurate, this means that some of the features found on inspection of the surface were LME cracks. However, due to the short time windows and highly localised nature of the correct conditions, the cracks cannot grow deep enough to be consistently detected in cross-sections. When comparing the LBW conditions that did not create detectable LME cracks with Gleeble hot tensile conditions leading to LME cracks and RSW conditions from literature leading to LME, the following differences can be concluded:

  In the Gleeble setup, the extreme conditions leading to susceptibility are present macroscopically. Temperature and strain rate are both in susceptible ranges in an area of several tens of mm^2, whereas the LBW reaches susceptible conditions in areas in the μm^2 range and for only 200 ms. In RSW, the susceptible areas experience a different stress state: mostly dynamic shear as opposed to mostly static tensile in LBW.

The proposed LBW under tension setup does not suffice as is to explore the local thermo-mechanical conditions leading to LME. The setup will need alterations to achieve LME cracks penetrating further into the bulk to be detectable and enough LME cracks to be detectable *in-situ*. Possible alterations must either change the loading state of the samples, either more extreme loading or more dynamic loading, or increase the area and time where the material is susceptible to LME. More extreme loading could be achieved by further increasing the applied tensile load beyond the yield strength. However, higher loads also increase the probability of slight inaccuracies in the loading, such as a misalignment, to lead to failure of the weld, which would make monitoring the crack growth more difficult. Another possibility is to change the mechanism of loading. Instead of manual loading, the load would have to be applied mechanically and be controlled remotely. This way, a strain rate can be applied during the welding process, creating a significantly more dynamic system.

To increase the time and space windows where the material is susceptible, the laser could be defocussed further, a lower power could be used or a combination of both. The temperature will increase more gradually and longer welding times can be used, resulting in larger areas being within the susceptible temperature range. However, this method will also decrease the slope of the thermal gradient, reducing the thermal stresses. It would have to be ensured that thermal stresses are still sufficient to cause LME.

7. Acknowledgements

The writing of this thesis would not have been possible without the support and assistance provided throughout its duration.

I would like to thank my supervisors, Dr. Ir. Marcel Hermans and Gautam Agarwal PhD for the feedback and suggestion they provided, the many fruitful discussions and the continued motivational support.

I also thank He Gao PhD for providing input from previous studies and the useful suggestions given.

Finally, I want to thank Jurriaan van Slingerland, Remko Seijffers, Sander van Asperen and Hans Hofman for their practical guidance and support.

Bibliography

[1]   WorldAutoSteel, "Advanced High-Strength Steel (AHSS) Definitions," 2020. [Online]. Available: https://www.worldautosteel.org/steel-basics/automotive-advanced-high-strength-steel-ahss-definitions/. [Accessed 15 December 2020].

[2]   S. Keeler, M. Kimchi and P. Mooney, "Advanced High-Strength Steels Application Guidelines Version 6.0," WorldAutoSteel, 2020.

[3]   R. Hugo and R. Hoagland, "Gallium penetration of aluminum: in-situ TEM observations at the penetration front," *Scripta Materialia,* vol. 41, no. 12, pp. 1341-1346, 1999.

[4]   S. Bassini, S. Cataldo, C. Cristalli, A. Fiore, C. Sartorio, M. Tarantino, M. Utili, P. Ferroni, M. Ickes, A. Alemberti and M. Frignani, "Material Performance in lead and lead-bismuth alloy," in *Comprehensive Nuclear Materials (Second Edition)*, Elsevier Ltd., 2020, pp. 218-241.

[5]   X. Gong, "Liquid Metal Embrittlement of a 9Cr-1Mo Ferritic-martensitic Steel in Lead-bismuth Eutectic Environment under Low Cycle Fatigue," Arenberg Doctoral School, Leuven, 2015.

[6]   A. Hojna, F. Di Gabriele and J. Klecka, "Characteristics and Liquid Metal Embrittlement of the steel T91 in contact with Lead-Bismuth Eutectic," *Journal of Nuclear Materials,* vol. 472, pp. 163-170, 2016.

[7]   K. Bag, K. Ray and E. Dwarakadasa, "Influence of Martensite Content and Morphology on Tensile and Impact properties of High-Martensite Dual-Phase Steels," *Metallurgical and materials Transactions A,* vol. 30A, no. 1202, 1999.

[8]   G. Agarwal, "Study if solidification cracking during laser welding in advanced high strength steels: A combined experimental and numerical approach," Delft, 2019.

[9]   J. Barthelmie, A. Schram and V. Wesling, "Liquid Metal Embrittlement in Resistance Spot Welding and Hot Tensile Tests of Surface-refined TWIP steels," *IOP Conference Series: Materials Science and Engineering,* vol. 118, no. 012002, 2016.

[10]   R. Ashiri, M. Haque, C. Ji, M. Shamnian, H. Salimijazi and Y. Park, "Supercritical area and critical nugget diameter for liquid metal embrittlement of Zn-coated twinning induced plasticity steels," *Scripta Materialia,* vol. 109, pp. 6-10, 2015.

[11]   R. Ashiri, M. Shamanian, H. Salimijazi, M. Haque, J. Bae, C. Ji, K. Chin and Y. Park, "Liquid metal embrittlement-free welds of Zn-coated twinning induced plasticity steels," *Scripta Materialia,* vol. 114, pp. 41-47, 2016.

[12]   D. Choi, A. Sharma, S. Uhm and J. Jung, "Liquid Metal Embrittlement of Resistance Spot Welded 1180 TRIP Steel: Effect of Electrode Force on Cracking Behavior," *Metals and Materials International,* vol. 25, pp. 219-228, 2019.

[13]   Wikipedia, "Gallium," Wikipedia, 9 January 2021. [Online]. Available: https://en.wikipedia.org/wiki/Gallium. [Accessed 13 January 2021].

[14]   S. Mishra and R. Datta, "Embrittlement of Steel," in *Encyclopedia of Materials: Science and Technology (Second Edition)*, Elsevier Ltd., 2001, pp. 2761-2768.

[15]   N. Glickman and M. Nathan, "On the kinetic mechanism of grain boundary wetting in metals," *Journal of Applied Physics,* vol. 85, no. 3185, 1999.

[16]   W. Sigle, G. Richter, M. Ruhle and S. Schmidt, "Insight into the atomic-scale mechanism of liquid metal embrittlement," *Applied Physics Letters,* vol. 89, no. 121911, 2006.

[17]   R. Stumpf and P. Feibelman, "Towards an understanding of liquid-metal embrittlement: energetics of Ga on Al surfaces," *Physical Review B,* vol. 54, no. 5145, 1996.

[18]   D. Thomson, V. Heine, M. Payne, N. Marzari and M. Finnis, "Insight into gallium behavior in aliminum grain boundaries from calculation on Σ=11 (113) boundary," *Acta Materialia,* vol. 48, no. 14, pp. 3623-3632, 2000.

[19]   P. McIntyre and A. Mercer, "Corrosion Testing and Determination of Corrosion Rates," in *Shreir's Corrosion*, Elsevier Ltd., 2010, pp. 1443-15526.

[20]   A. Huntington, "Discussion on report to Beilby Prize Committee," Journal of the Institure of Metals, 1914.

[21]   R. Clegg and D. Jones, "Liquid metal embrittlement in failure analysis," *Soviet materials science: a translation of Fiziko-khimicheskaya mekhanika materialov,* vol. 27, pp. 453-459, 1992.

[22]   A. Westwood, C. Preece and M. Kamdar, "Chapter 10- Adsorption-induced brittle fracture in liquid-metal environments," in *Engineering Fundamentals and Environmental Effects*, Academic Press, 1971, pp. 589-644.

[23]   T. Mae and S. Hori, "Embrittlement of aluminum by liquid gallium," *Journal of Japan Institute of Light Metals,* vol. 34, no. 1, pp. 3-7, 1984.

[24]   K. Ina and H. Koizumi, "Penetration of liquid metals into solid metals and liquid metal embrittlement," *Materials Science and Engineering: A,* Vols. 387-389, pp. 390-394, 2004.

[25]   N. Fonstein, "Dual-phase steels: Design, Metallurgy, Processing and Applications," in *Automotive steels*, Chicago, Woodhead Publishing, 2017, pp. 169-216.

[26]   Wikipedia, the free encyclopedia, "Galvanization," Wikipedia, 9 november 2020. [Online]. Available: https://en.wikipedia.org/wiki/Galvanization. [Accessed 23 november 2020].

[27]   R. Pereira, E. Oliveira, M. Lima and S. Brasil, "Corrosion of Galvanized Steel Under Different Soil Moisture Contents," *Materials Research,* vol. 18, no. 3, pp. 563-568, 2015.

[28] Zinkpower, "Hot Dip Galvanizing Data Sheet," [Online]. Available: https://www.zinkpower.com/media/files/arbeitsblaetter_englisch/1_2.pdf. [Accessed 23 November 2020].

[29] Staff, Corrosionpedia, "An Introduction to the Galvanic Series: Galvanic Compatibility and Corrosion," Corrosionpedia, 12 November 2020. [Online]. Available: https://www.corrosionpedia.com/an-introduction-to-the-galvanic-series-galvanic-compatibility-and-corrosion/2/1403. [Accessed 23 November 2020].

[30] K. Hickey, "Welding simulation for AHSS: LME during resistance spot welding," 20 November 2019. [Online]. Available: https://www.ahssinsights.org/news/welding-simulation-for-ahss-lme-during-resistance-spot-welding/. [Accessed 15 January 2021].

[31] P. Mallick, "Joining for lightweight vehicles," in *Materials, Design and Manufacturing for Lightweight Vehicles*, Woodhead Publishing, 2010, pp. 275-308.

[32] L. Lin, C. Hsu, C. Lee, T. Kuo and S. Jeng, "Effects of zinc layer thickness on resistance spot welding of galvanized mild steel," *Journal of Materials Processing Technology,* vol. 251, 2017.

[33] T. Barnes and I. Pashby, "Joining techniques for aluminium spaceframes used in automobiles. Part 1 - solid and liquid phase welding," *Journal of Materials Processing Technology,* vol. 99, pp. 62-71, 2000.

[34] S. Lynch, "Perspectives in Hydrogen in Metals," in *A fractographic study of gaseous hydrogen embrittlement and liquid-metal embrittlement in a tempered-martensitic steel*, 1986, pp. 739-750.

[35] D. Roessler, "Laser Processing of Materials for Automotive Applications," *Material and Manufacturing Processes,* vol. 4, no. 3, pp. 285-310, 1989.

[36] T. Maeji, K. Ibano, S. Yoshikawa, D. Inoue, S. Kuroyanagi, K. Mori, E. Hoashi, K. Yamanoi, N. Sarukura and Y. Ueda, "Laser energy absorption coefficient and in-situ temperature measurement of laser-melted tungsten," *Fusion Engineering and Design,* vol. 124, pp. 287-291, 2017.

[37] S. Riches and TWI, "Industrial Lasers and Applications in Automotive Welding," in *Lasers in the Automotive Industry*, Nissan Motor Manufacturing (UK) Ltd, Sunderland, 1998.

[38] G. H. M. den Ouden, Welding technology, Vssd, 2009.

[39] M. Razmpoosh, A. Macwan, E. Biro, D. Chen, Y. Peng, F. Goodwin and Y. Zhou, "Liquid metal embrittlement in laser beam welding of Zn-coated 22MnB5 steel," *Materials and Design,* vol. 155, pp. 375-383, 2018.

[40] C. Beal, X. Kleber, D. Fabregue and M. Bouzekri, "Liquid zinc embrittlement of twinning-induced plasticity steel," *Scripta Materialia,* vol. 66, pp. 1030-1033, 2012.

[41]   Royal Society of Chemistry, "Periodic Table - Zinc," Royal Society of Chemistry, [Online].
       Available: https://www-rsc-org.tudelft.idm.oclc.org/periodic-table/element/30/zinc. [Accessed
       27 november 2020].

[42]   B. De Cooman, O. Kwon and K. Chin, "State-of-the-knowledge on TWIP steel," *Materials Science
       and Technology,* vol. 28, no. 5, pp. 513-527, 2012.

[43]   J. Van den Bosch, D. Sapundjiev and A. Almazouzi, "Effects of temperature and strain rate on the
       mechanical properties of T91 material tested in liquid lead bismuth eutectic," *Journal of Nuclear
       Materials,* vol. 356, pp. 237-246, 2006.

[44]   American Association State, "Standard Test Methods for Tension Testing of Metallic Materials,"
       February 2020. [Online]. Available: https://compass-astm-
       org.tudelft.idm.oclc.org/EDIT/html_annot.cgi?E8+16ae1#s00033. [Accessed 23 November 2020].

[45]   Metallurgy for Dummies, "Phase diagrams Fe-Mn, Fe-Co, Fe-Mo," Metallurgy for Dummies, 2021.
       [Online]. Available: https://www.metallurgyfordummies.com/phase-diagrams-fe-mn-fe-co.html.
       [Accessed 25 Januray 2021].

[46]   Z. Yang and R. Johnson, "An EAM simulation of the alpha-gamma iron interface," *Modelling and
       Simulation in Materials Science and Engineering,* vol. 1, no. 5, p. 707, 1993.

[47]   H. Zheng, X. Li, R. Tran, C. Chen, M. Horton, D. Winston, K. Persson and S. Ong, "Grain boundary
       properties of elemental metals," *Acta Materialia,* vol. 186, pp. 40-49, 2020.

[48]   H. Okamoto, "The C-Fe (Carbon-Iron) System," *Journal of Phase Equilibria,* vol. 13, no. 5, pp. 543-
       565, 1992.

[49]   T. Massalski, H. Okamoto, P. Subramanian and L. Kacprzak, Binary Alloy Phase Diagrams, 2nd
       edition, ASM International, 1990.

[50]   M. Giorgi, J. Guillot and R. Nicolle, "Theoretical model of the interfacial reactions between solid
       iron and liquid zinc-aluminium alloy," *Journal of materials science,* vol. 40, pp. 2263-2268, 2005.

[51]   K. Nogi, K. Ogino, A. Mclean and W. Miller, "The Temperature Coefficient of the Surface Tension
       of Pure Liquid Metals," *Metallurgical Transactions B,* vol. 17, no. B, 1968.

[52]   M. Erol, K. Keslioglu and N. Marasli, "Measurement of Solid-liquid Interfacial Energy for Solid Zn
       in Equilibrium with the ZnMg Eutectic Liquid," *Journal of Physics: Condensed Matter,* vol. 19, no.
       176003, 2007.

[53]   J. Monk, Y. Yang, M. Mendelev, M. Asta, J. S. Hoyt and D.Y., "Temperature dependence of the
       solid-liquid interface free energy of Ni and Al from molecular dynamics simulation of nucleation,"
       Modelling and Simulation in Materials Science, vol. 18, no. 015004, 2010.

[54]   PubChem, "Zinc Oxide Compound Summary," [Online]. Available: https://pubchem-ncbi-nlm-nih-gov.tudelft.idm.oclc.org/compound/Zinc-oxide#section=Molecular-Formula. [Accessed 29 January 2021].

[55]   F. Caballero, C. Capdevila and C. Garcia de Andres, "Kinetics and dilatometric behaviour of non-isothermal ferrite-to-austenite transformation," *Materials Science and Technology,* vol. 17, no. 9, pp. 1114-1118, 2001.

[56]   L. Zhang and D. Guo, "A general etchant for revealing prior-austenite grain boundaries in steels," *Materials Characterization,* vol. 30, no. 4, pp. 299-302, 1993.

[57]   S. Babu, "Application of Synchrotron and neutron scattering techniques for tracking phase transformations in steels," in *Phase Transformations in Steels*, USA, Woodhead Publishing Series in Metals and Surface Engineering, 2012, pp. 588-633.

[58]   R. Souza, E. Silva, A. Jorge Jr., J. Cabrera and O. Balancin, "Dynamic recovery and dynamic recrystallization competition on a Nb- and N-bearing austenitic stainless steel biomaterial: Influence of strain rate and temperature," *Materials Science and Engineering: A,* vol. 582, pp. 96-107, 2013.

[59]   L. Zhu, S. Honrao, B. Rijal, R. Hennig and M. Manuel, "Phase equilibira and diffusion coefficients in the Fe-Zn binary system," *Materials & Design,* vol. 188, no. 108437, 2020.

[60]   J. Lippold, W. Baeslack and I. Varol, "Heat-Affected Zone Liquation Cracking in Austenitic and Duplex Stainless Steels," *The welding journal,* 1992.

[61]   Wikipedia, "Shear Strength," Wikipedia, 8 December 2020. [Online]. Available: https://en.wikipedia.org/wiki/Shear_strength#:~:text=0.75*TYS%20.&text=There%20are%20no%20published%20standard,equal%20to%20their%20torsional%20strength.. [Accessed 21 December 2020].

[62]   W. Shockley and W. Read, "Quantitative Predictions From Dislocation Models Of Crystal Grain Boundaries," *Physics Review,* vol. 75, no. 692, 1949.

[63]   G. Agarwal, A. Kumar, I. Richardson and M. Hermans, "Evaluation of solidification cracking susceptibility during laser welding in advanced high strength automotive steels," *Materials and Design,* vol. 183, no. 108104, 2019.

Appendices

Appendix A Pictures of Gleeble samples
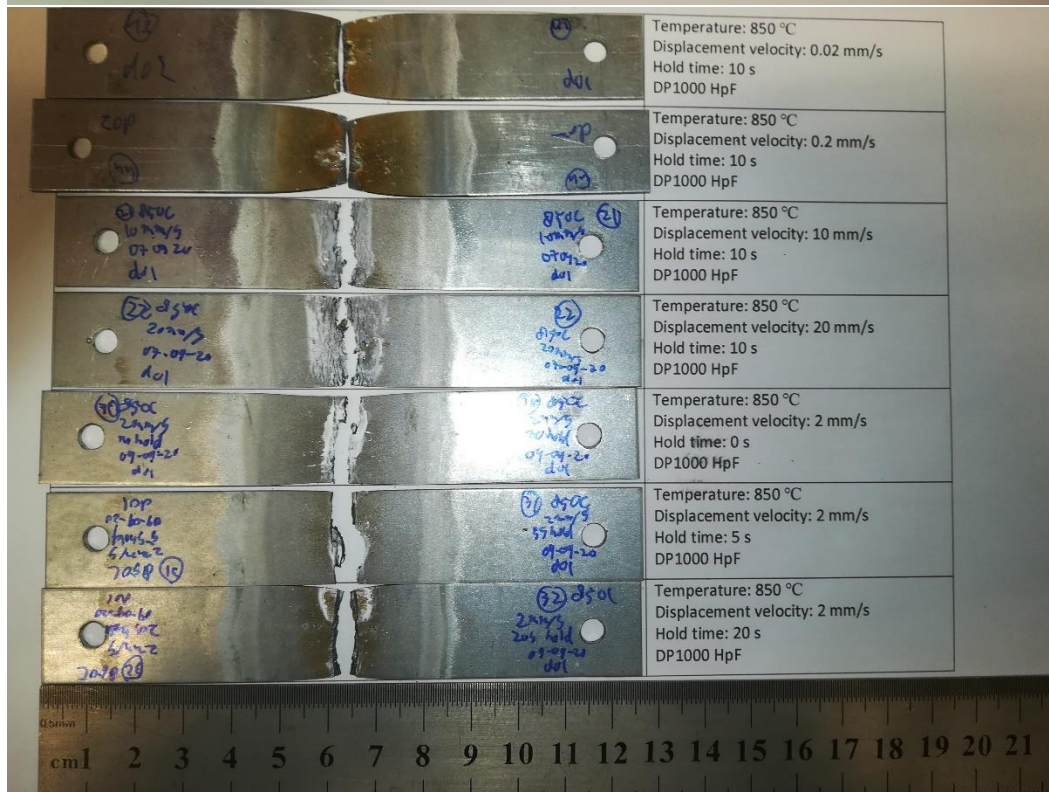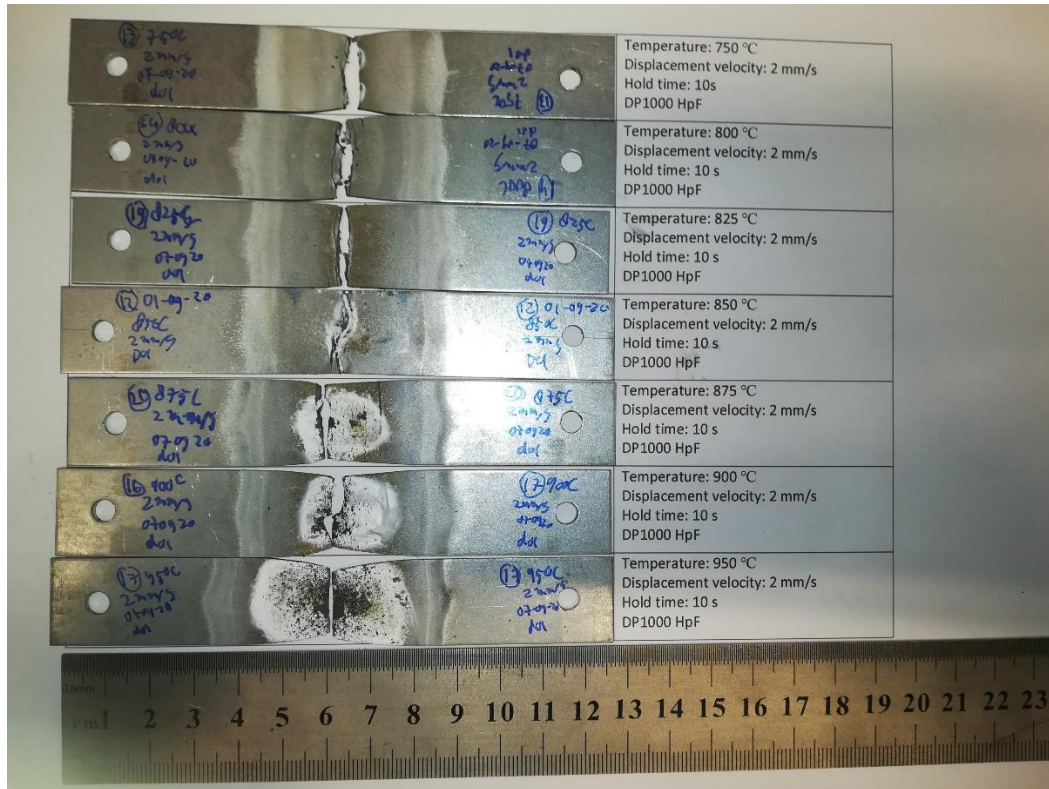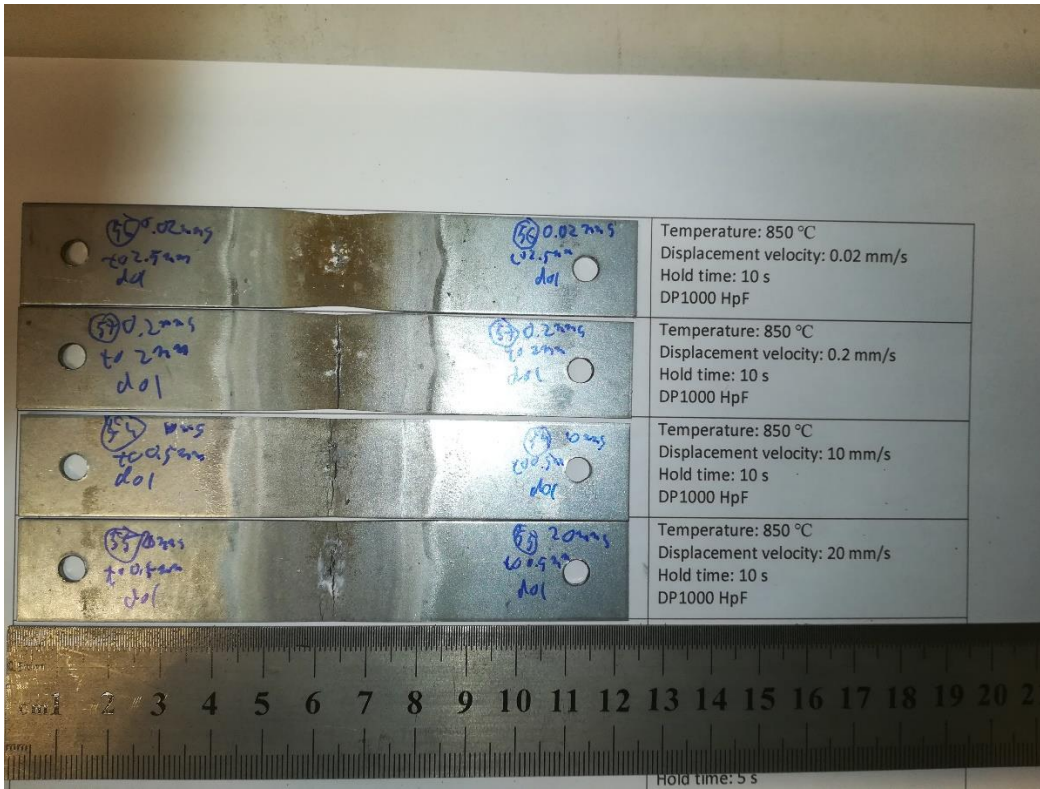
Figure A.1: Pictures taken of failed Gleeble samples to illustrate fracture mode.

Appendix B Gleeble micrographs
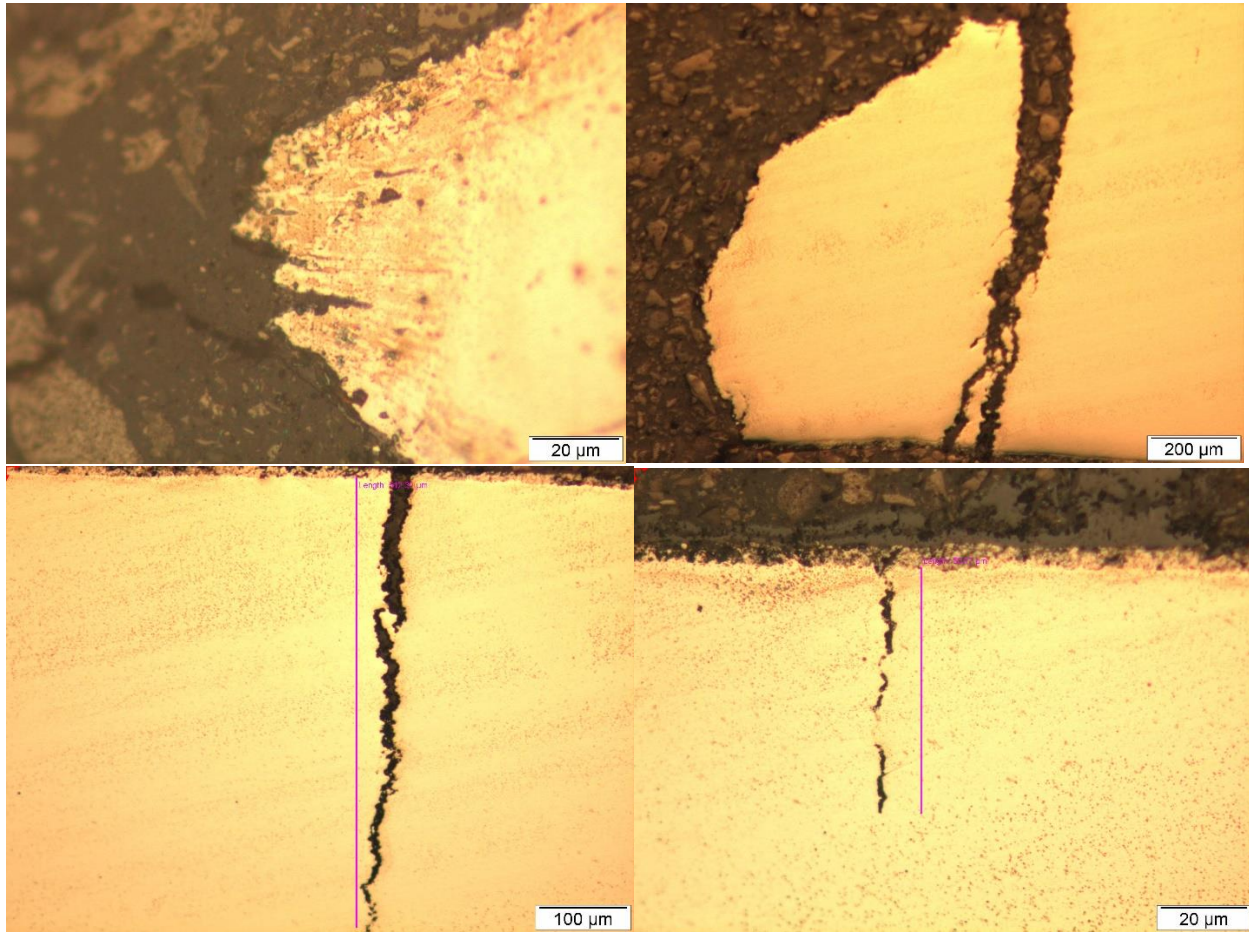
Figure B.1: Optical micrographs of Gleeble samples at 850 °C with a strain rate of 0.13. Top left shows an uncoated fracture surface, top right a coated fracture surface and the bottom two show LME cracks.
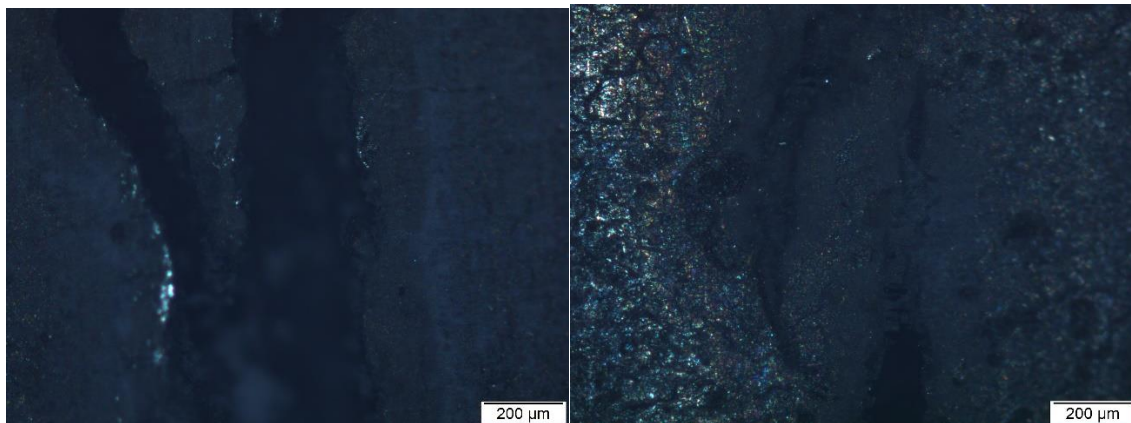
Figure B.2: Optical micrographs of a crack opening and crack tip in Gleeble samples at 800 °C with a strain rate of 0.13.
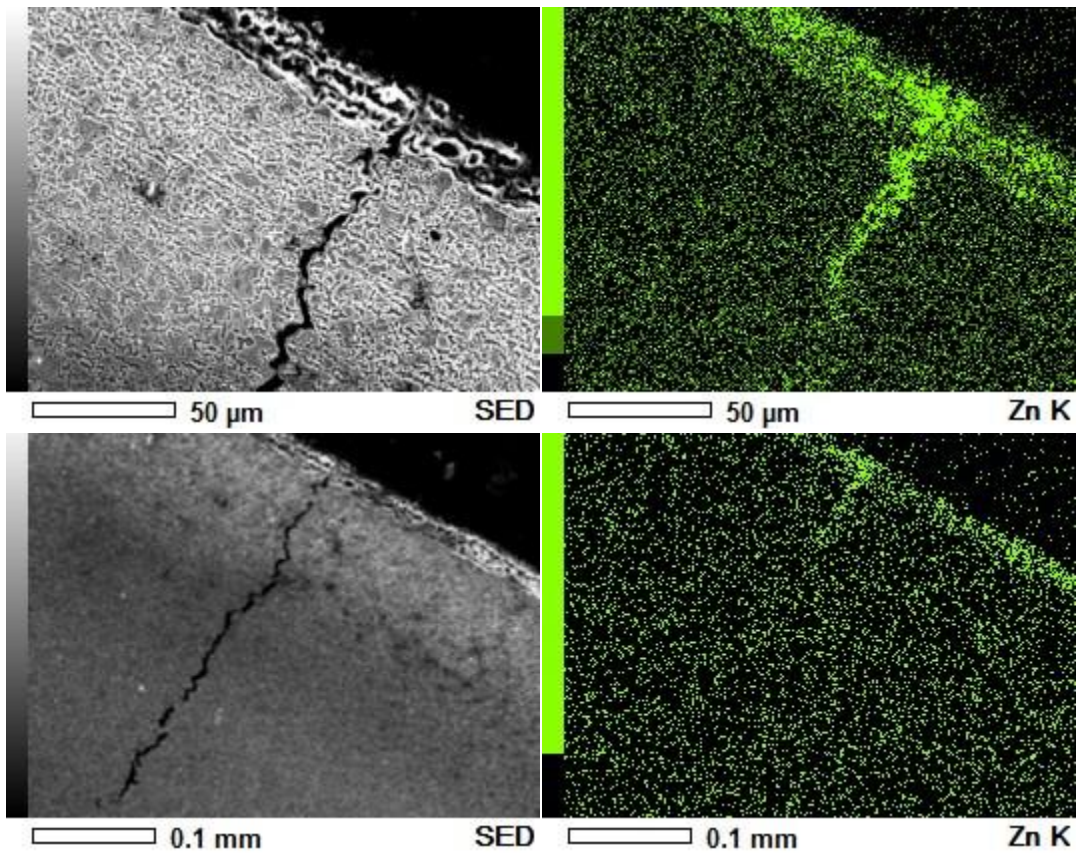
Figure B.3: EDS analyses of etched Gleeble samples, showing difficulty of analysing zinc in etched specimens.

Appendix C Optical micrographs of LBW specimens

Figure C.1: Keyence digital micrograph of the surface of a LBW sample welded at 800W, with the beam defocussed to 1mm for 2s under 100% ys tensile load.

Figure C.2: Keyence digital micrograph of linear weld welded at 1 kW at a speed of 10mm/s under 100% ys tensile load.

Figure C.3: Keyence digital micrograph of the bottom surface of laser welded samples. Left image: welded at 800 W, beam defocussed to 1mm for 2s at 100% ys tensile load. Right image: welded at 800 W, beam defocussed to 1mm for 2s at 800% ys tensile load.

Figure C.4: Keyence digital micrograph of top surface of laser welded sample welded at 200 W, beam defocussed to 7mm for 10 s at 100% ys tensile load, showing a possible crack feature.

Appendix D SEM micrographs of semi-random cross-sections of LBW samples
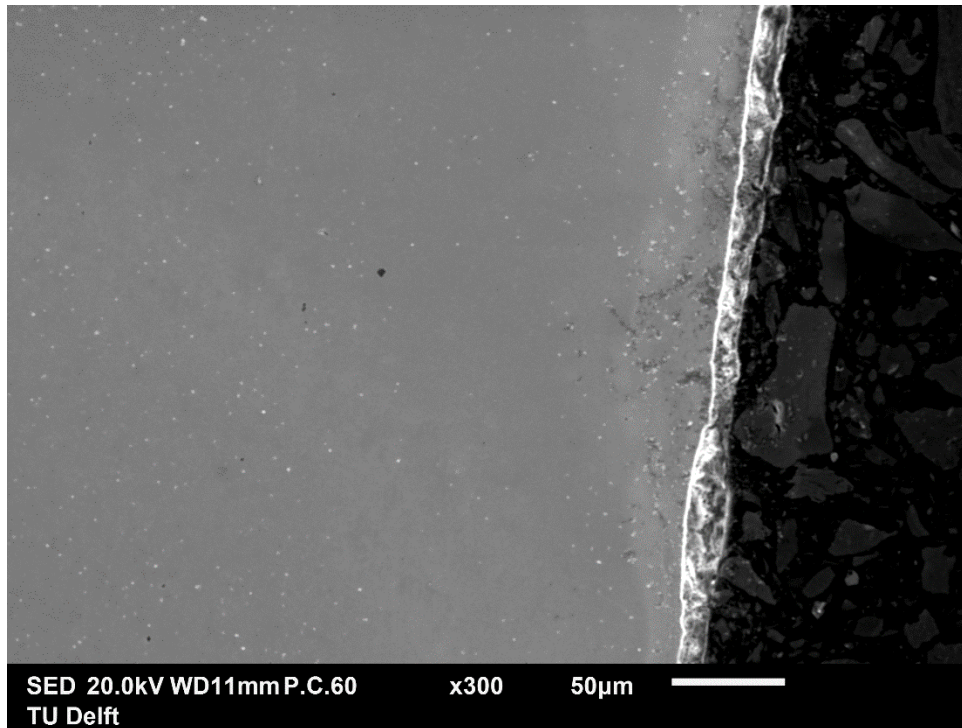
Figure D.1: SEM micrograph of an unloaded LBW sample, welded at 800W, beam defocussed to 1mm for 2s under 80% ys tensile load.
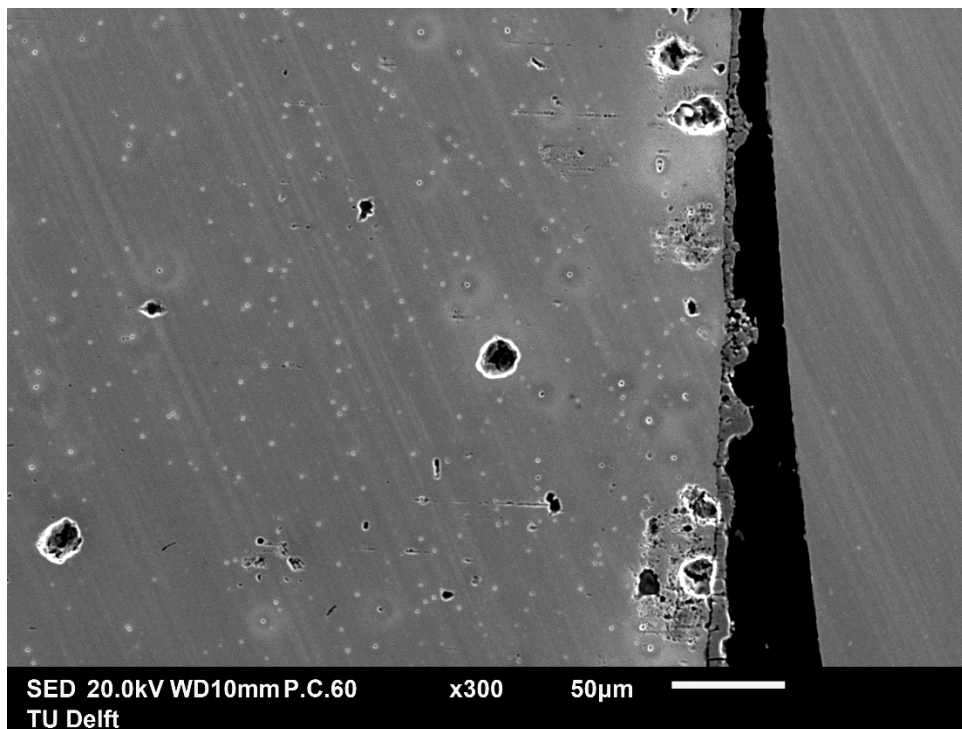
Figure D.2: SEM micrograph of an LBW sample, welded at 800W, beam defocussed to 1mm for 2s under 80% ys tensile load, taken at the top surface in the HAZ.
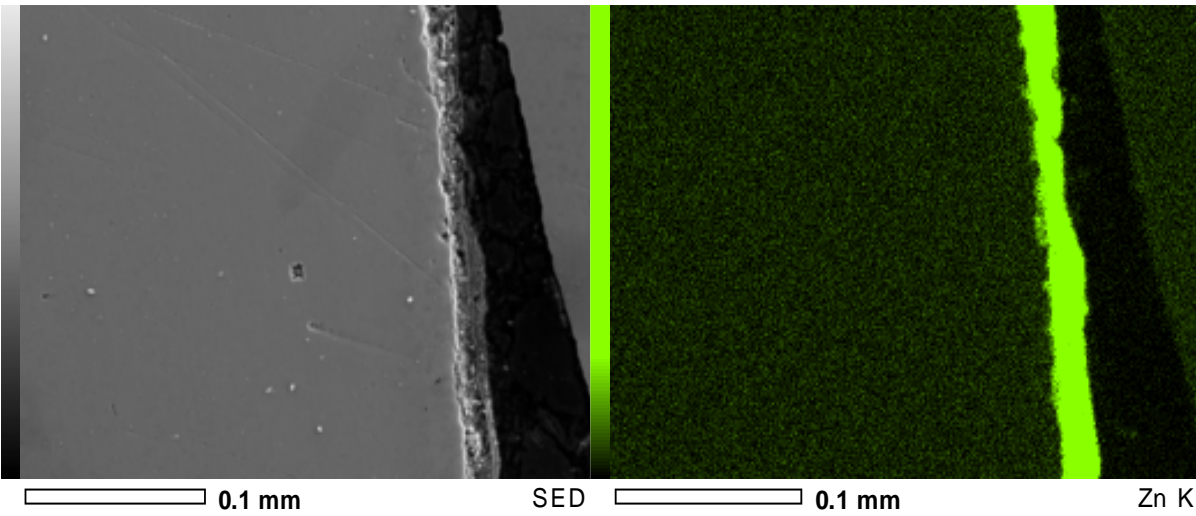
Figure D.3: EDS zinc distribution of a semi-random cross section through a LBW sample welded at 800W, beam defocussed to 1mm, for 2s under 80% ys tensile load, taken in the HAZ.
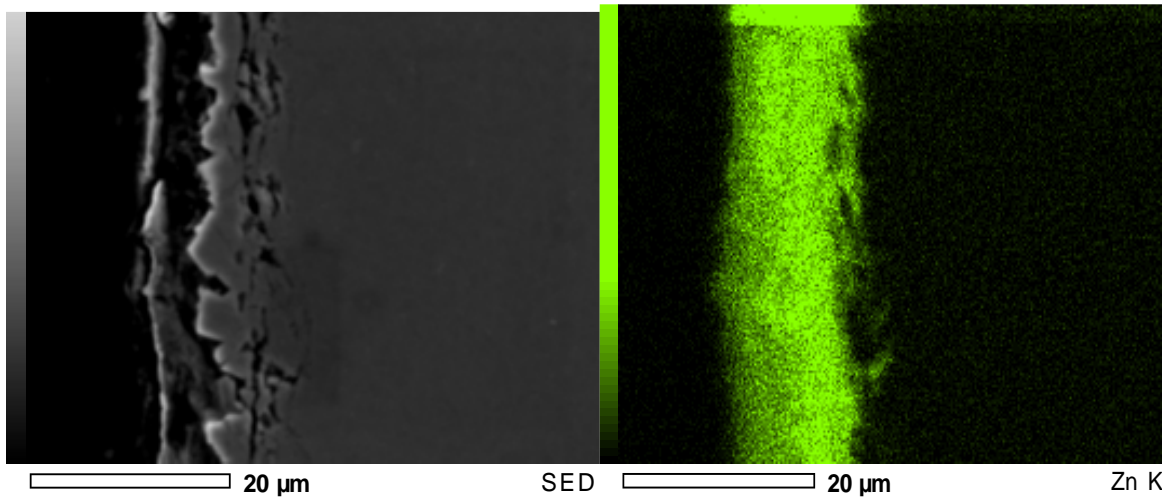
Figure D.4: EDS zinc distribution of a semi-random cross section through a LBW sample welded at 800W, beam defocussed to 1mm, for 2s under 100% ys tensile load, taken in the HAZ.

Appendix E FEA results for LBW samples.
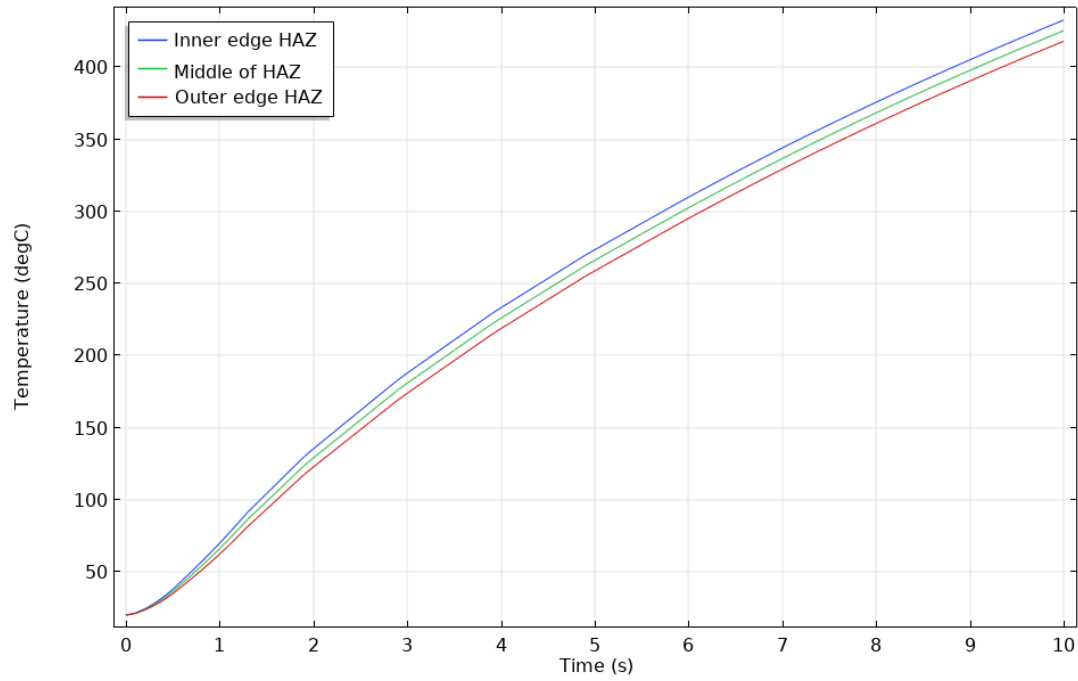
Figure E.1: Temperature distribution in the HAZ of LBW under tension sample, loaded to 100% YS welded with 300W for 10s with the beam defocussed to 7mm.
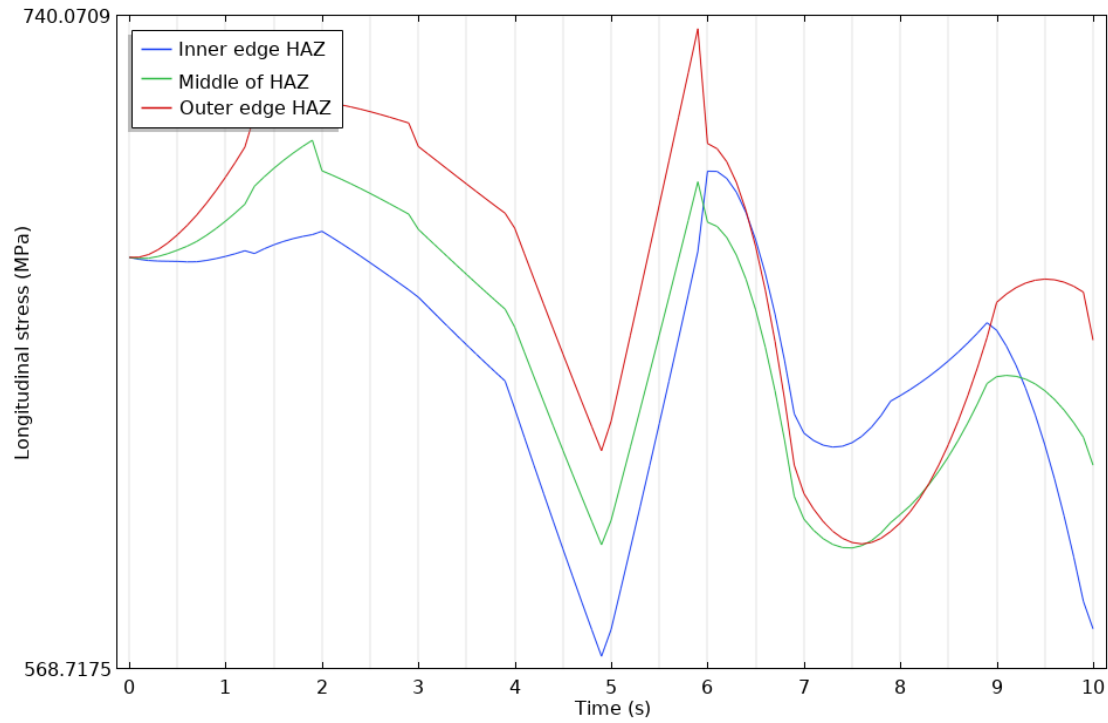
Figure E.2: Longitudinal stress distribution in the HAZ of LBW under tension sample, loaded to 100% YS welded with 300W for 10s with the beam defocussed to 7mm.
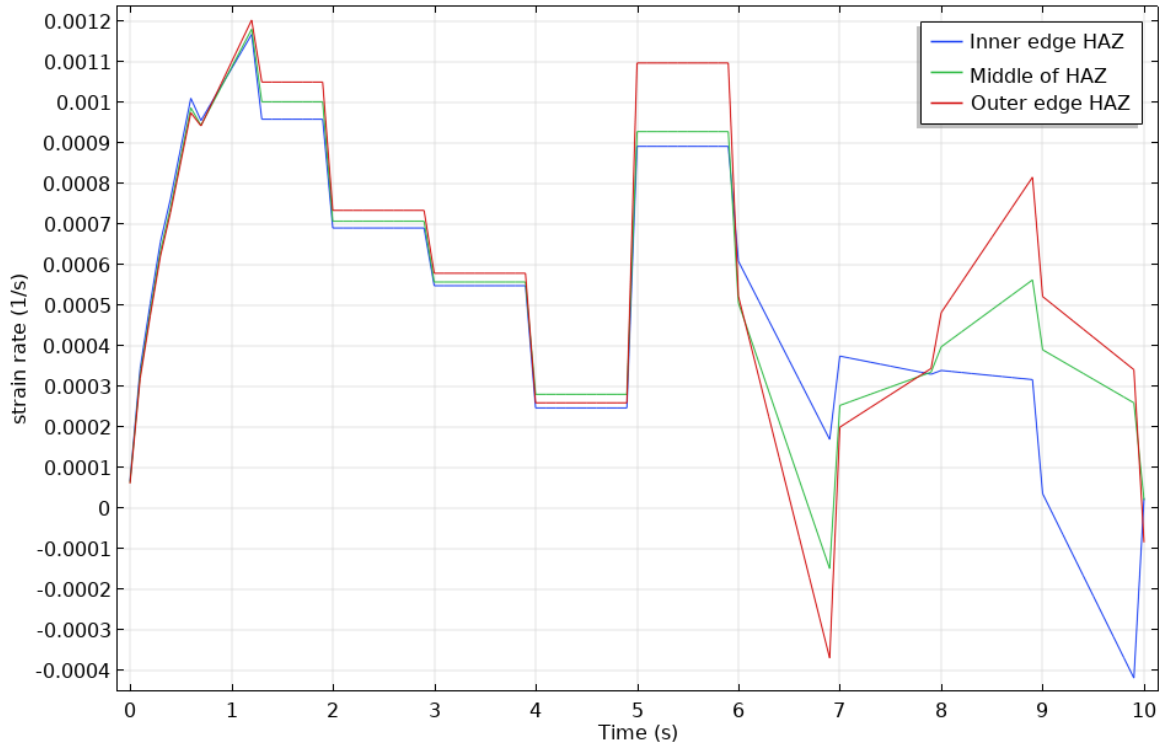
Figure E.3: Longitudinal strain rate distribution in the HAZ of LBW under tension sample, loaded to 100% YS welded with 300W for 10s with the beam defocussed to 7mm.
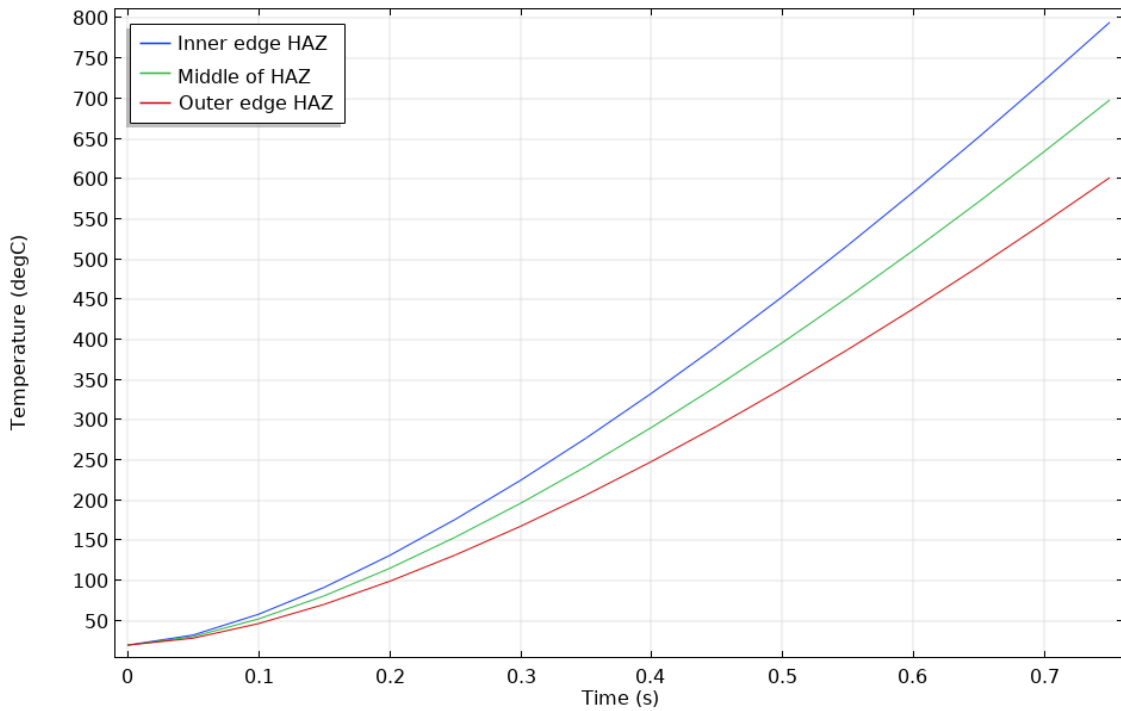
Figure E.4: Temperature distribution in the HAZ of LBW under tension sample, loaded to 100% YS welded with 1500W for 0.75s with the beam defocussed to 7mm.
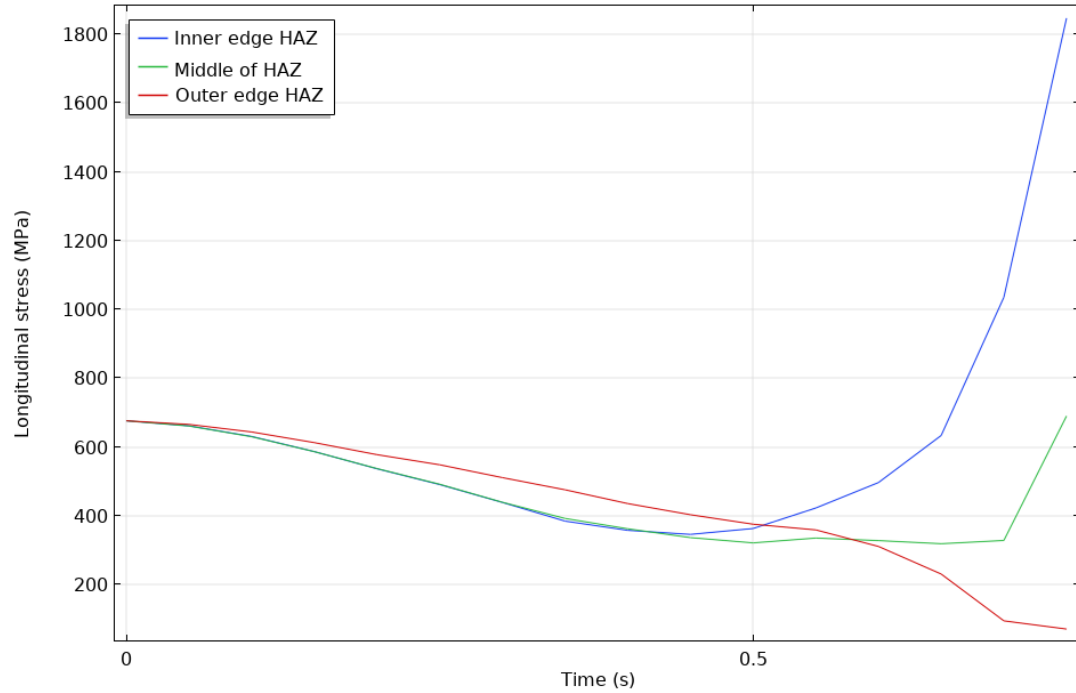
Figure E.5: Longitudinal stress distribution in the HAZ of LBW under tension sample, loaded to 100% YS welded with 1500W for 0.75s with the beam defocussed to 7mm.
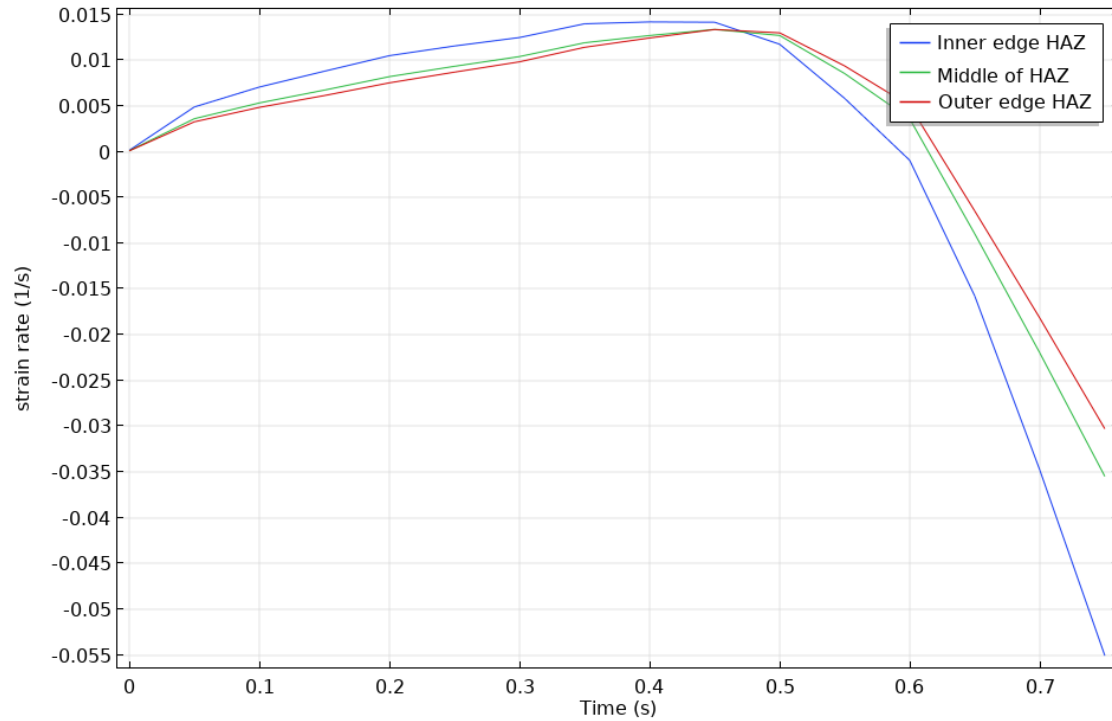
Figure E.6: Longitudinal strain rate distribution in the HAZ of LBW under tension sample, loaded to 100% YS welded with 1500W for 0.75s with the beam defocussed to 7mm.